Signal processing of intracardiac electrograms:

optimization of mapping and ablation in tachyarrhythmias

© Milad El Haddad, Ghent 2014

Printed at: University Press, Zelzate, Belgium

“ Say not, I have found the truth, but rather, I have found a truth. ”

Khalil Gibran, The Prophet (1923)

The cover of the book is an edited picture of the anatomy of the heart drawing of Leonardo Da Vinci (1510)

The complete electronic version of the dissertation is available for download at:

http://elhaddad.eu/thesis/

Or scan the code below:

Signal processing of intracardiac electrograms:

optimization of mapping and ablation in tachyarrhythmias

Milad El Haddad

Promoter:
Prof. Dr. Mattias Duytschaever

Co-promoter:
Prof. Dr. Roland Stroobandt

This dissertation was submitted in partial fulfillment of the requirements for the degree of Doctor of Philosophy in Biomedical Sciences.

Department of Internal Medicine
Faculty of Medicine and Health Sciences
Ghent University, Belgium
Academic year 2013-2014

Board of examiners:

Prof. Dr. Sébastien Knecht, CHU Brugmann, Belgium

Prof. Dr. Ir. Pascal Verdonck, Ghent University, Belgium

Prof. Dr. Luc Jordaens, Ghent University, Belgium

Prof. Dr. Peter Gheeraert, Ghent University, Belgium

Prof. Dr. Harry Crijns, University of Maastricht, the Netherlands

Prof. Dr. Ulrich Schotten, University of Maastricht, the Netherlands

TABLE OF CONTENTS

TABLE OF CONTENTS (EXTENDED)

PART I

PART II

Optimization of mapping and ablation in regular and irregular tachyarrhythmias

Algorithmic detection of the beginning and end of bipolar electrograms: Implications for novel methods to assess local activation time during atrial tachycardia

Histogram Analysis: A novel method to detect and differentiate fractionated electrograms during atrial fibrillation

A meta-analysis on adjunctive complex fractionated atrial electrogram ablation: comparing the incomparable?

PART III

PART I

General introduction

In this introductory chapter, the heart as an electro-mechanical system and the faulty in this system leading to tachyarrhythmias are briefly described. The chapter continues to describe the detection of arrhythmias since early times and the transition to non-pharmaceutical treatments by catheter ablation.

The heart: an electro-mechanical system

The heart is a hollow muscular organ that pumps blood into the circulatory system by mechanical contractions. The contraction of the heart is controlled by an electrical conduction system that insures a sequential and organized functionality. A heart beat is triggered by an impulse initiated at the sinus node which consists of specialized pacemaker cells. The excitation impulse first propagates through the upper two chambers of the heart (right and left atria). This depolarizes the myocardial tissue, leading to contraction of the atria and pushing blood to the lower two chambers (right and left ventricles). The impulse is then transmitted to the ventricles by the atrioventricular node (AV node, the only electric connection between the atria and the ventricles). Since the mechanical activity is slower than the electric conduction, the atrioventricular node delays the impulse insuring all blood has been pumped out from the atria to the ventricles. The bundle of His, the distal part of the AV junction, conducts the impulse rapidly from the AV node to the bundle branches. The bundle branches are connected to the Purkinje fibers that spread out all over the ventricles, delivering the impulse to the myocardial fibers. With the ventricles contracting, the blood is pumped to the lungs (from the right ventricle) and body (from the left ventricle). In a normal heart, the impulse takes around 200 ms to travel from the sinus node to the myocardial cells in the ventricles. Problems with any part of this process can cause abnormal activity in the heart, leading to arrhythmias.

Arrhythmias: faulty control system

The activity of the heart is controlled by an electrical system prone to errors due to several factors such as diseases, genetic abnormalities, life-style, and aging. Faults in the control system might cause either harmless or life threatening arrhythmias. An arrhythmia can cause a fast (tachyarrhythmia) or slow (bradyarrhythmia) heart beat (normal heart beats approximately 60 times per minute), and may be also regular or irregular. This thesis relates to three types of tachyarrhythmias: 1) atrial tachycardia (regular), 2) ventricular tachycardia (regular), and 3) atrial fibrillation (irregular). The mechanism of atrial and ventricular tachycardias can be classified into either focal or macro-reentry based upon their activation pattern. Focal tachycardias are characterized by radial activation pattern and may be caused by automatic, triggered, or micro-reentrant mechanisms.[1] Macro-reentry tachycardias are characterized by continuous activation pattern and are caused by reentry through large and well defined circuits (loops).[2] Describing the mechanism of atrial fibrillation remains ambiguous because several hypotheses (e.g. multiple-wavelet, triggers from pulmonary veins, high-frequency sources or rotors, or autonomic innervation) have been put forward.[3]

History of arrhythmias

While the Greeks and Romans more than 2000 years ago introduced the term *arhythmus* to describe an abnormal pulse,[4] the first documented arrhythmia (premature ventricular beats) dates back to the late 18th century by Etienne-Jules Marey.[5] Between 1902 and 1909, Mackenzie, Wenckebach, Cushny, and Lewis studied the cardiac rhythm with pulse recordings and published comprehensive reports on arrhythmias (Fig. 1.1).[,6,7,8,9,10] Although Einthoven was the first to record the electrocardiogram of an arrhythmia, namely atrial fibrillation,[11] it was examined by others only after Einthoven's electrocardiograph instrument became commercial in 1908.[7] This first reported arrhythmia was described in detail by Lewis, Rothberger and Winterberg as *auricular fibrillation* (later named atrial fibrillation).[10,11]

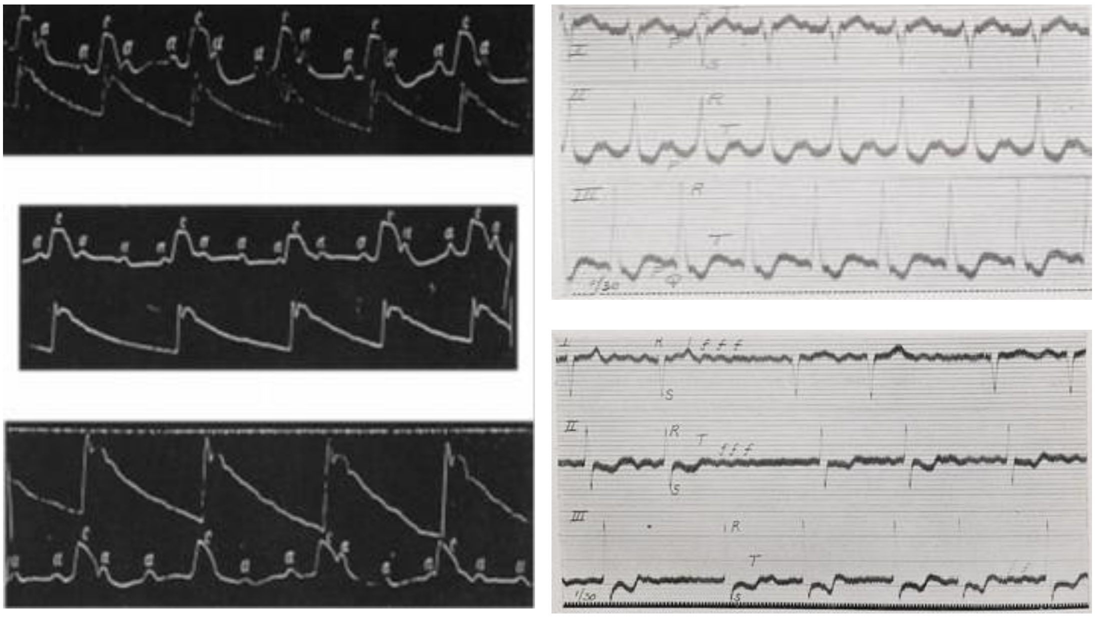

A) Pulse recordings of arrhythmias by Mackenzie

B) Electrocardiogram recordings of arrhythmias by Lewis

Figure I-1: *A) Pulse tracings of complete heart block recorded from a 66 year old man. a = atrial contraction; c = carotid pulse. The other tracing represents the radial pulse. These were first published in Mackenzie's 1902 book.[6] B) Electrocardiogram tracings of regular tachycardia (upper panel) and auricular fibrillation (lower panel) as recorded by Lewis.[10]*

Common types of arrhythmias

Arrhythmias originating from the upper chambers of the heart are classified as supraventricular tachycardias (SVT). The most common SVTs are atrioventricular nodal reentrant tachycardia, Wolff-Parkinson-White syndrome, atrial flutter, atrial tachycardia, and atrial fibrillation. Arrhythmias originating from the lower chambers of the heart are classified as ventricular tachycardias (VT) and are generally life-threatening. The most common VTs are monomorphic VT, polymorphic VT, torsades de pointes, and ventricular fibrillation.

Treatment of arrhythmias

The mechanisms of most arrhythmias except for atrial fibrillation (AF) are well known. As such, most arrhythmias can be managed successfully by pharmaceutical or/and non-pharmaceutical treatments. The mechanism of atrial fibrillation is still unclear, and therefore this arrhythmia is the most difficult to treat. Since the mid-20th century, management of atrial fibrillation has been achieved by pharmacological treatment.[12,13,14] In the early 1960s, non-pharmacological treatment based upon electric cardioversion was introduced.[15] After 30 years however, this treatment alone showed limited long-term efficacy,[16,17,18] even when combined with antiarrhythmic drugs.[19] Moreover, studies in the early 1990s reported high mortality in those patients taking antiarrhythmic drugs.[18,19] Implanted atrial defibrillators were safe and effective to restore sinus rhythm in patients with AF.[20] However, its success was restricted by patient discomfort and immediate re-initiation of AF.[21]

Catheter ablation as treatment of arrhythmias

Catheter ablation (by radiofrequency, microwave, cryo, thermal, laser, etc...) of the diseased cardiac tissue has emerged in the past few decades. Currently, radiofrequency (RF) is the most common type of energy used in catheter ablation procedures. The RF used for ablation of cardiac tissue is characterized by unmodulated current ranging from 30 KHz to 300 MHz.[22] The delivery of RF energy to the tissue in contact with the ablation catheter causes irreversible tissue destruction due to thermal injury (> 50C).[23, 24]

Ablation strategies are defined based upon the type of arrhythmia. For instance, in focal tachycardia, the site of the earliest activation (could be referred to as the source) is usually targeted. In macro-reentry, an ablation line is performed to break the circuit and restore normal conduction. Atrial fibrillation on the other hand, requires more complex strategies (isolation of triggers in pulmonary veins, linear lesions, ablation of complex fractionated electrograms, rotors, dominant frequency, etc…). As such, RF ablation procedures are guided by electro-anatomical mapping systems to identify appropriate ablation targets. Electro-anatomical mapping - performed by a mapping catheter - combines the 3D geometry of the heart chamber and the local electric properties of the intracardiac tissue. This provides a visual representation of the electrical activity of the chamber (3D color-coded activation maps). For accurate construction of the activation maps and correct identification of ablation targets, appropriate analysis of the recorded electric signals is essential. Intracardiac recordings are usually either bipolar electrograms (difference in electric potential between two intracardiac electrodes) or unipolar (difference in electric potential between an intracardiac electrode and an external reference), each having advantages and limitations. For most electrophysiologists, visual interpretation and analysis of intracardiac electrograms remains challenging. As such, algorithmic methods to analyze electrograms are required in order to facilitate and improve safety and efficacy of the ablation procedure in atrial tachycardia (AT), ventricular tachycardia (VT), and atrial fibrillation (AF).

Signal processing and analysis of intracardiac electrograms

Algorithmic analysis of intracardiac electrograms is necessary to characterize and identify the activation pattern of tachyarrhythmias. Several methods based upon time-domain analysis and spectral analysis have been implemented in current clinical electro-anatomical mapping systems and are used to map and guide ablation procedures in daily clinical practice.

A *time-domain method* (interval confidence level, ICL) to quantify complex and fractionated atrial electrograms (CFAE) recorded during atrial fibrillation was introduced by Nademanee et al and Biosense Webster Inc. (Diamond Bar, CA, USA) in 2004.[25,26] The CFAE-ICL algorithm counts the positive and negative peaks (positive deflection followed by negative deflection and vice versa respectively) above a fixed noise threshold. A duration interval is set to define the blanking time between two peaks. If the duration between two consecutive peaks is smaller or larger than the pre-defined blanking interval, both peaks are considered invalid and excluded from the ICL count (Figure 2).

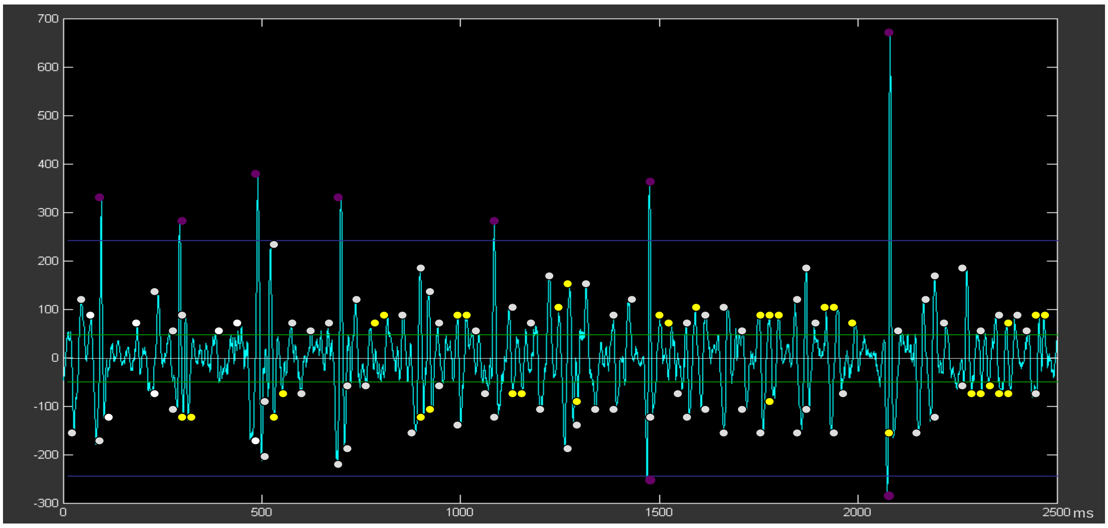

Figure I-2: *Interval confidence level (ICL) algorithm applied to a high fractionated atrial electrogram. ICL score = 78. Peaks within the blanking window (10-50ms) are discarded from counting (yellow circles). Peaks above the ventricular far-field threshold are blanked (purple circles). Blue line= ventricular far-field threshold set at 0.25mV, green line= noise threshold set at 0.05mV.*

Others have suggested using the mean of the intervals (CFE-mean) as an alternative parameter to the ICL peak count. In this algorithm valid peaks are above the pre-defined fixed noise threshold, the duration between two consecutive peaks has to be greater than the pre-defined blanking interval. The annotation of valid peaks is placed at the instant of maximum-negative slope (-dv/dt) of the peaks (Figure 3).

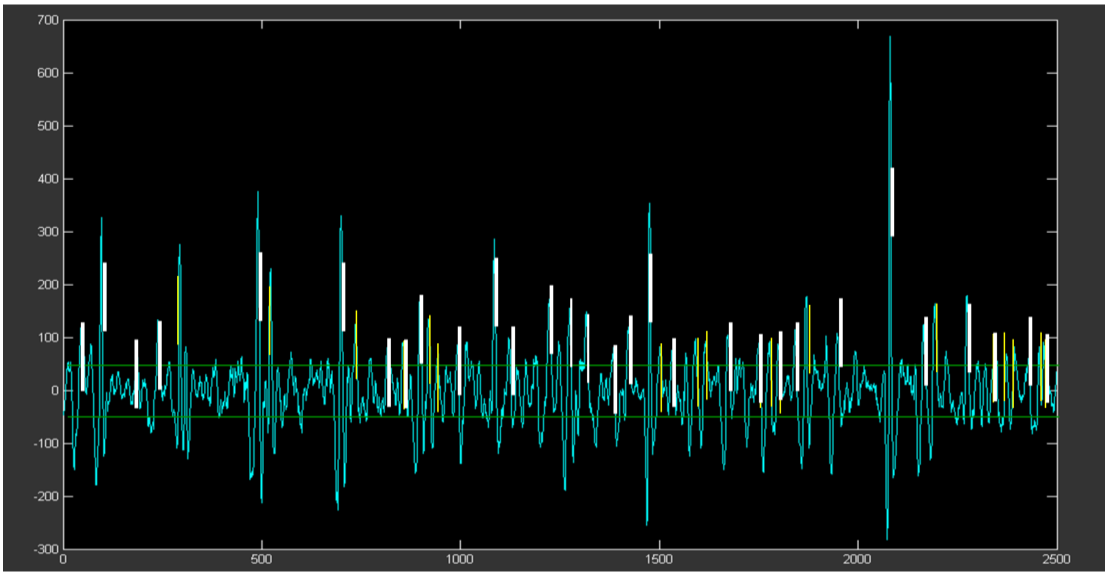

Figure I-3: *CFE-mean algorithm applied to a high fractionated atrial electrogram. CFE-mean value = 45ms. The maximal -dv/dt following the positive peaks are annotated (white lines). Peaks within the blanking window (10-30ms) are discarded from counting (yellow lines). Green line= noise threshold set at 0.05mV.*

These two CFAE algorithms are embedded in the CARTO mapping system and the NavX mapping system (St Jude Medical, St. Paul, MN, USA) respectively. Although many studies reported high success rates using these methods to guide CFAE ablation,[25-32] many centers and research groups still doubt the efficacy of the CFAE-ICL and CFE-mean algorithms in guiding atrial fibrillation ablation due to low success rates.[27, 32, 33,34]

Several *frequency domain methods* have been introduced to map and guide ablation of AF. Analysis based on the frequency spectrum assumes that the complexity of fractionated electrograms is a summation of several waves (sinusoidal). As such, the Fast-Fourier transformation (FFT) is able to differentiate complex signals by analyzing their components (Figure 4).

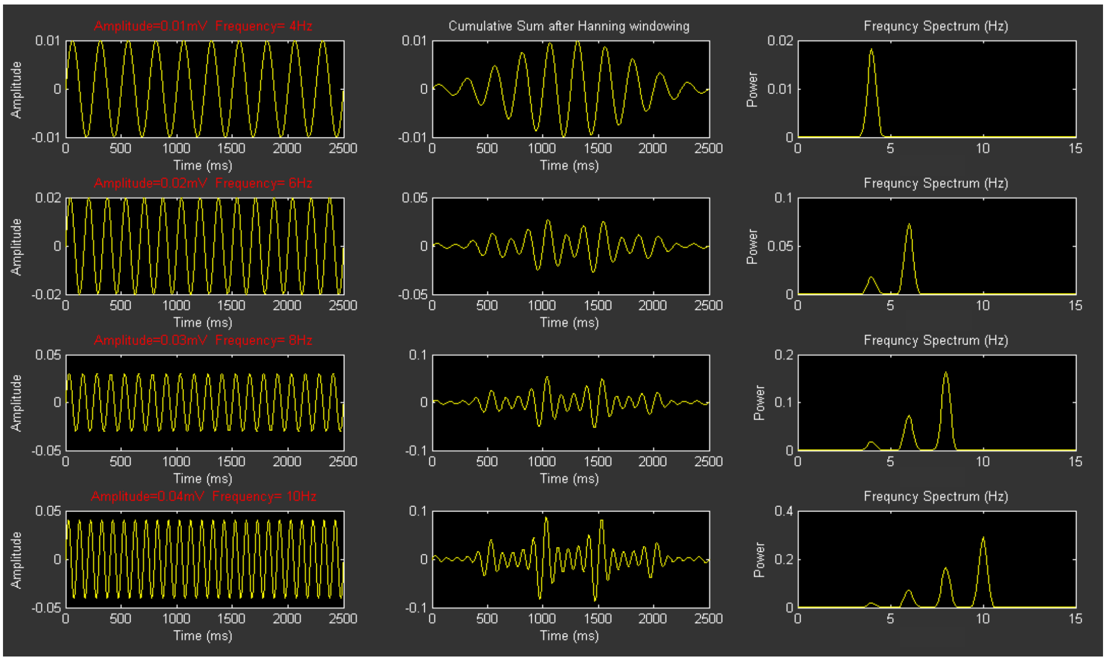

Figure I-4: *Reconstruction of signals (middle panel) by summing several sinusoidal waves of different frequencies and amplitudes (left panel). The corresponding magnitude spectrum for each step is shown on the right panel. It can be seen from the spectrum in the lower right panel that the component at 10Hz is the dominant frequency.*

Prior studies have used the dominant frequency (DF) of the spectrum as a parameter to identify fast-firing locations in the atria which are suitable targets for ablation.[36-39] DF was defined as the highest (most powerful) frequency component in the frequency spectrum. For atrial electrograms, the frequency bandwidth of interest lies between 3 and 15Hz and DF mainly within 4–9 Hz (Figure 5). Another commonly used parameter in frequency analysis is the regularity index (RI) or organization index

(OI).[35-38] The RI is calculated as the ratio of the power of the DF and its adjacent frequencies within 0.75Hz to the power of the other harmonics in the bandpass of interest (3-15Hz). RI is commonly used as a reliability parameter for DF. A very low RI (<0.2) indicates a poor signal-to-noise ratio.[39] Similar to the time-domain analysis algorithms, the DF and RI algorithms showed modest efficacy in clinical outcome.[39-41]

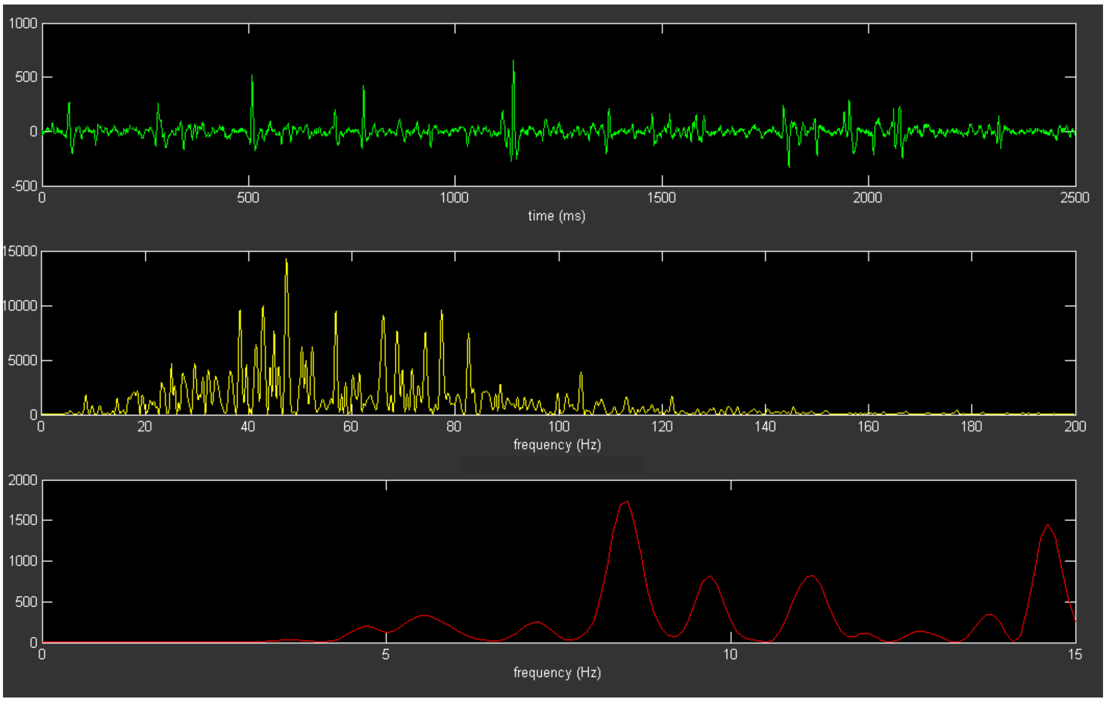

Figure I-5: *Top panel, intracardiac bipolar electrogram of 2.5 seconds. Middle panel, complete frequency spectrum of the electrogram. Low panel, Frequency spectrum of interest (3-15 Hz). In this example, the dominant frequency (DF) is 8.5 Hz and regularity index (RI) is 0.29.*

Given the above, novel algorithmic tools are required to improve the outcome of ablation procedures in terms of long term success, fewer complications, shorter procedure time, and less repeat ablations.

Scope of the dissertation

This dissertation reports the research performed on signal processing and analysis of intracardiac electrograms. The aim of the research was to introduce novel algorithmic methods to optimize mapping and ablation in tachyarrhythmias. In particular, this book describes the introduction, development, and validation of novel algorithmic methods to facilitate and guide ablation procedures in the three common arrhythmias: atrial tachycardia (AT), ventricular tachycardia (VT), and atrial fibrillation (AF).

References

1. Zipes DP, Jalife J, eds: Cardiac Electrophysiology. From Cell to Bedside. Fifth Edition. Philadelphia, PA: W.B. Saunders, 2009, p.577-579, 589

2. Macfarlane, P.W.; Oosterom, A.; Pahlm, O.; Kligfield, P.; Janse, M.; Camm, J. Comprehensive Electrocardiology, 2010

3. Lüderitz B. Historical perspectives of cardiac electrophysiology. Hellenic J Cardiol. 2009;50:3-16.

4. Mackenzie, J., The Study of the Pulse, Arterial, Venous, and Heptic, and of the Movements of the Heart. Edinburgh: Pentland, 1902.

5. Wenckebach, K.F., Arhythmia of the Heart: A Physiological and Clinical Study. Edinburgh: Green, 1904

6. Cushny AR, Edmunds CW. Paroxysmal irregularity of the heart and auricular fibrillation. Am J Med Sci. 1907;133:66–77.

7. Mackenzie, J., Diseases of the Heart. London: Frowde, 1908

8. Lewis T. Auricular fibrillation: a common clinical condition. Br Med J. 1909;2:1528.

9. Rothberger CJ, Winterberg H. Vorhofflimmern und Arhythmia perpetua. Wien Klin Wochenschr. 1909;22:839–44.

10. De La Chapelle CE, Rose OA. The management of acute cardiac emergencies. Circulation, 1951;IV:764-774.

11. McCord MC, Taguchi JT. A study of the effect of procaine amide hydrochloride in supraventricular arrhythmias. Circulation 1951;IV:387-393.

12. Sokolow M, Ball RE. Factors influencing conversion of chronic atrial fibrillation with special reference to serum quinidine concentration. Circulation 1956;XIV;568-583.

13. Lown B, Amarasingham R, Neuman J. New method for terminating cardiac arrhythmias. Use of synchronized capacitor discharge. JAMA. 1962;182:548-55.

14. Nattel S. Newer development in the management of atrial fibrillation. AM Heart J 1995;130:1094-1096.

15. Sopher SM, Camm AJ. Atrial fibrillation: maintenance of sinus rhythm versus rate control. Am J Cardiol. 1996;77:24A-37A.

16. Prystowsky EN, Benson DW Jr, Fuster V, Hart RG, Kay GN, Myerburg RJ, Naccarelli GV, Wyse DG. Management of patients with atrial fibrillation. A Statement for Healthcare Professionals. From the Subcommittee on Electrocardiography and Electrophysiology, American Heart Association. Circulation. 1996;93:1262-77.

17. Golzari H, Cebul RD, Bahler RC. Atrial fibrillation: restoration and maintenance of sinus rhythm and indications for anticoagulation therapy. Ann Intern Med. 1996;125:311-23.

18. Preliminary report: effect of encainide and flecainide on mortality in a randomized trial of arrhythmia suppression after myocardial infarction. The Cardiac Arrhythmia Suppression Trial (CAST) Investigators. N Engl J Med. 1989;321:406-12.

19. Mortality and Morbidity in Patients Receiving Encainide, Flecainide, or Placebo. The Cardiac Arrhythmia Suppression Trial. N Engl J Med. 1991;324:781-8.

20. Wellens HJ, Lau CP, Lüderitz B, Akhtar M, Waldo AL, Camm AJ, Timmermans C, Tse HF, Jung W, Jordaens L, Ayers G. Atrioverter: an implantable device for the treatment of atrial fibrillation. Circulation. 1998;98:1651-6.

21. Timmermans C, Rodriguez LM, Smeets JL, Wellens HJ. Immediate reinitiation of atrial fibrillation following internal atrial defibrillation. J Cardiovasc Electrophysiol. 1998;9:122-8.

22. Borggrefe M, Hindricks G, Haverkamp W, Breithardt G. Catheter ablation using radiofrequency energy. Clin Cardiol. 1990;13:127-31.

23. Simmers TA, de Bakker JMT, Wittkampf FHM, Hauer RNW. Effects of heating with radiofrequency power on myocardial impulse conduction: is radiofrequency ablation exclusively thermally mediated? J Cardiovasc Electrophysiol 1996;7:243-7.

24. Calkins H, Prystowsky E, Carlson M, Klein LS, Saul JP, Gillette P. Temperature monitoring during radiofrequency catheter ablation procedures using closed loop control. Circulation 1994;90:1279-86.

25. Nademanee K, McKenzie J, Kosar E, Schwab M, Sunsaneewitayakul B, Vasavakul T, Khunnawat C, Ngarmukos T: A new approach for catheter ablation of atrial fibrillation: Mapping of the electrophysiologic substrate. J Am Coll Cardiol 2004;43:2044-2053.

26. Monir G, Pollak SJ. Consistency of the CFAE phenomena using custom software for automated detection of complex fractionated atrial electrograms (CFAEs) in the left atrium during atrial fibrillation. J Cardiovasc Electrophysiol. 2008;19:915-919.

27. Schmitt C, Estner H, Hecher B, Luik A, Kolb C, Karch M, Ndrepepa G, Zrenner B, Hessling G, Deisenhofer I. Radiofrequency ablation of complex fractionated atrial electrograms (CFAE): preferential sites of acute termination and regularization in paroxysmal and persistent atrial fibrillation. J Cardiovasc Electrophysiol. 2007;18:1039-1046.

28. Nademanee K, Schwab M, Porath J, Abbo A: How to perform electrogram-guided atrial fibrillation ablation. Heart Rhythm 2006;3:981-984.

29. Scherr D, Dalal D, Cheema A, Cheng A, Henrikson CA, Spragg D, Marine JE, Berger RD, Calkins H, Dong J: Automated detection and characterization of complex fractionated atrial electrograms in human left atrium during atrial fibrillation. Heart Rhythm 2007;4:1013-1020.

30. Stiles MK, Brooks AG, John B; Shashidhar, Wilson L, Kuklik P, Dimitri H, Lau DH, Roberts-Thomson RL, Mackenzie L, Willoughby S, Young GD, Sanders P. The effect of electrogram duration on quantification of complex fractionated atrial electrograms and dominant frequency. J Cardiovasc Electrophysiol 2008; 19: 252 – 258.

31. Takahashi Y, O'Neill MD, Hocini M, Dubois R, Matsuo S, Knecht S, Mahapatra S, Lim KT, Jaïs P, Jonsson A, Sacher F, Sanders P, Rostock T, Bordachar P, Clémenty J, Klein GJ, Haïssaguerre M. Characterization of electrograms associated with termination of chronic atrial fibrillation by catheter ablation. J Am Coll Cardiol. 2008;51:1003-1010.

32. Porter M, Spear W, Akar JG, Helms R, Brysiewicz N, Santucci P, Wilber DJ. Prospective study of atrial fibrillation termination during ablation guided by automated detection of fractionated electrograms. J Cardiovasc Electrophysiol. 2008;19:613-620.

33. Oral H, Chugh A, Good E, Wimmer A, Dey S, Gadeela N, Sankaran S, Crawford T, Sarrazin JF, Kuhne M, Chalfoun N, Wells D, Frederick M, Fortino J, Benloucif-Moore S, Jongnarangsin K, Pelosi F Jr, Bogun F, Morady F. Radiofrequency catheter ablation of chronic atrial fibrillation guided by complex electrograms. Circulation. 2007;115:2606-2612.

34. Estner HL, Hessling G, Ndrepepa G, Luik A, Schmitt C, Konietzko A, et al. Acute effects and long-term outcome of pulmonary vein isolation in combination with electrogram-guided substrate ablation for persistent atrial fibrillation. Am J Cardiol 2008; 101: 332 – 337.

35. Pachon M JC, Pachon M EI, Pachon M JC, Lobo TJ, Pachon MZ, Vargas RN, Pachon DQ, Lopez M FJ, Jatene AD. A new treatment for atrial fibrillation based on spectral analysis to guide the catheter RF-ablation. Europace. 2004;6:590-601.

36. Ng J, Goldberger JJ. Understanding and interpreting dominant frequency analysis of AF electrograms. J Cardiovasc Electrophysiol. 2007;18:680-685.

37. Sanders P, Berenfeld O, Hocini M, Jaïs P, Vaidyanathan R, Hsu LF, Garrigue S, Takahashi Y, Rotter M, Sacher F, Scavée C, Ploutz-Snyder R, Jalife J, Haïssaguerre M. Spectral analysis identifies sites of high-frequency activity maintaining atrial fibrillation in humans. Circulation. 2005;112:789-797.

38. Takahashi Y, Sanders P, Jaïs P, Hocini M, Dubois R, Rotter M, Rostock T, Nalliah CJ, Sacher F, Clémenty J, Haïssaguerre M. Organization of frequency spectra of atrial fibrillation: relevance to radiofrequency catheter ablation. J Cardiovasc Electrophysiol. 2006;17:382-388.

39. Rostock T, Salukhe TV, Steven D, Drewitz I, Hoffmann BA, Bock K, Servatius H, Müllerleile K, Sultan A, Gosau N, Meinertz T, Wegscheider K, Willems S. Long-term single- and multiple-procedure outcome and predictors of success after catheter ablation for persistent atrial fibrillation. Heart Rhythm. 2011;8:1391-1397.

40. Tilz RR, Chun KR, Schmidt B, Fuernkranz A, Wissner E, Koester I, Baensch D, Boczor S, Koektuerk B, Metzner A, Zerm T, Ernst S, Antz M, Kuck KH, Ouyang F. Catheter ablation of long-standing persistent atrial fibrillation: a lesson from circumferential pulmonary vein isolation. J Cardiovasc Electrophysiol. 2010;21:1085-93.

41. Lin YJ, Tsao HM, Chang SL, Lo LW, Hu YF, Chang CJ, Tsai WC, Suenari K, Huang SY, Chang HY, Wu TJ, Chen SA. Role of high dominant frequency sites in nonparoxysmal atrial fibrillation patients: insights from high-density frequency and fractionation mapping. Heart Rhythm. 2010;7:1255-62.

PART II

Optimization of mapping and ablation in regular and irregular tachyarrhythmias

We have introduced and developed novel algorithmic methods to optimize mapping and ablation in regular and irregular tachyarrhythmias. These algorithms and their clinical implications are described in this section.

Chapters 1 to 3 describe the algorithms in regular atrial tachycardia (AT) and ventricular tachycardia (VT). The first chapter describes the development and validation of the algorithms in atrial tachycardias. The second chapter describes the evaluation of the performance of the methods in mapping and ablation of atrial and ventricular tachycardias. The third chapter reports a unique case of spiral wave reentry atrial tachycardia mapped by wave activation mapping.

Chapters 3 to 6 describe the algorithms in irregular tachyarrhythmias, namely atrial fibrillation (AF). Chapter 4 describes the development and prospective validation of an algorithm to identify electrical isolation in pulmonary veins during sinus rhythm. Chapter 5 describes the development of a novel method to quantify and map fractionation in the left atria as a substrate-guide for ablation. Finally, chapter 6 provides an editorial about a meta-analysis for adjunctive ablation of fractionated electrograms.

CHAPTER 1

Algorithmic detection of the beginning and end of bipolar electrograms: Implications for novel methods to assess local activation time during atrial tachycardia

Milad El Haddad, MS; Richard Houben, PhD; Roland Stroobandt, MD, PhD; Frederic Van Heuverswyn, MD; Rene Tavernier, MD, PhD; Mattias Duytschaever, MD, PhD

This original research article was published in the journal Biomedical Signal Processing and Control, volume 8, issue 6, pages 981-991 in November 2013

Abstract

Introduction: Activation mapping is required to effectively ablate atrial tachycardia (AT). Conventional tools to assess local activation time (LAT) are based upon the peak of the bipolar electrogram (B-EGM, LAT_{Peak}) and the maximal negative slope of the unipolar electrogram (U-EGM, LAT_{Slope}). Bipolar electrograms are influenced by wavefront direction, bipole orientation, and inter-electrode spacing causing ambiguity in peak detection, whereas unipolar electrograms are disturbed by the presence of far-field signals. We developed a new algorithm to detect the beginning and end of bipolar electrograms (t_{begin} and t_{end}). Then, we introduced new LAT methods related to the onset of B-EGMs (LAT_{Onset}), the center of mass of B-EGMs (LAT_{CoM}), and the slope of U-EGMs within a pre-defined window ($LAT_{Slope\text{-}hybrid}$).

Methods and Results: In total 3,752 recordings from 31 AT patients were retrospectively analyzed. The signal-to-noise ratio (SNR) for B-EGMs was calculated to differentiate algorithmically high from low quality electrograms (HQ and LQ). In a subset of 328 B-EGMs, five experts validated the tbegin as determined by the algorithm by visual rating. The newly developed LAT methods were compared to the conventional LAT methods and to one another (Bland-Altman plots) in both HQ (n= 3003) and LQ EGMs (n = 749).

The t_{begin} algorithm was accurate (deviation < ± 10ms) in 96 ± 4% of HQ and 91 ± 8% of LQ B-EGMs. BA plots revealed the following difference (bias) and variation in HQ and LQ EGMs respectively: 1) LAT_{Onset} vs. LAT_{Peak}: 27 ± 30ms and 24 ± 62ms; 2) LAT_{CoM} vs. LAT_{Peak}: 0 ± 16ms and 2 ± 38ms; 3) $LAT_{Slope\text{-}hybrid}$ vs. LAT_{Slope}: 1 ± 32ms and 15 ± 110ms; 4) LAT_{Onset} vs. LAT_{CoM}: 22 ± 24ms and 18 ± 22ms; 5) LAT_{Onset} vs. $LAT_{Slope\text{-}hybrid}$: 16 ± 18ms and 13 ± 22ms; and 6) LAT_{CoM} vs. $LAT_{Slope\text{-}hybrid}$: 5 ± 20ms and 4 ± 18ms.

Conclusions: In the present study, we introduced three new methods to assess local activation time in AT, based upon an algorithm detecting accurately the beginning and end of the B-EGM complex. BA analysis of the new methods showed similar variation in high and low quality EGMs, suggesting that they introduce less ambiguity than the conventional peak method. LAT_{Onset} consistently yielded an earlier activation moment. $LAT_{Slope\text{-}hybrid}$ - by blanking far-field potentials - seems to be the optimal method for detection of the maximal negative slope in U-EGMs. Interestingly, LAT_{CoM} in B-EGMs coincided with the maximal negative slope in U-EGMs, suggesting its physiological sense and future use. The new LAT methods can be implemented in real-time mapping applications.

Keywords: Atrial tachycardia (AT); mapping algorithms; catheter ablation;
local activation time (LAT);

1.1 Introduction

Catheter ablation is an effective non-pharmacological method to treat symptomatic atrial tachycardia (AT). Combining 3D anatomical maps of the atria with assessment of local activation time (LAT) provides a powerful tool (electro-anatomical mapping) to guide ablation. Electro-anatomical mapping is usually performed by sequential point-by-point acquisition of coordinates and electrograms.

Assessment of LAT can be performed using unipolar and bipolar electrograms. Considering unipolar electrograms (U-EGM), Spach et al.[1, 2] showed that the maximum negative slope of U-EGM coincides with the upstroke of the action potential and the true moment of activation. U-EGMs, however, are susceptible to far-field potentials and are therefore rarely used in clinical practice.[3] For bipolar electrograms (B-EGM), the maximal positive and/or negative peak and the maximal negative slope (-dV/dt) have been suggested as fiducial markers for LAT.[4,5] B-EGM morphology, however, is influenced by wavefront direction, bipole orientation, electrode size, and inter-electrode spacing.[6] As such, assessment of LAT based upon the B-EGM peak or slope can introduce ambiguity, especially when electrograms become more complex due to multiple wavelets, showing various peaks and variation in morphology.

We aimed to develop an automated algorithm to reliably detect the beginning (t_{begin}) and the end (t_{end}) of the activation complex in the B-EGM. Then we introduced new methods to determine LAT within the time window demarcated by the t_{begin} and t_{end}: a) the onset of B-EGM (LAT_{Onset}), b) the center of mass of B-EGM (LAT_{CoM}), and c) the slope of U-EGM ($LAT_{Slope-hybrid}$).

1.2 Methods

Study subjects and database

A database of 3,752 recordings was collected from 31 patients who underwent catheter ablation of AT guided by the CARTO® system (Biosense-Webster, Diamond Bar, CA, USA) at the University Hospital of Ghent and Sint-Jan Hospital Bruges. An irrigated-tip ablation catheter with a distal 3.5mm tip and three 1mm ring electrodes spaced by 2-5-2mm (Navistar® Thermocool, Biosense-Webster, Diamond Bar, CA, USA) was used for both mapping and ablation. A decapolar catheter was placed in the coronary sinus and the proximal bipole was selected as a reference for activation mapping. The ablation strategy consisted of targeting the area of earliest activation for focal tachycardia and creation of a line of block for macro-reentry tachycardia. Prior to ablation, high-density point-by-point mapping (122±45 points) was performed. Care was taken to have 1) a stable position of the distal bipole for >3s, and 2) a homogeneous spatial distribution of the recorded EGMs. A U-EGM (tip electrode, band-pass filtered 0.5-500Hz) and a B-EGM (tip minus ring electrodes, band-pass filtered 30-240Hz) were recorded for 2.5 seconds from each site. After the procedure, all electrograms were extracted from the system and offline analysis was performed in Matlab v7.10 (The MathWorks, Inc., Natick, MA, USA). All algorithms were developed and executed on a regular Microsoft Windows PC with Intel Core 2 CPU clock rate of 3.0 GHz. On average, 120 EGMs (corresponding to one high-density map) were analyzed within 500 micro-seconds. From this database, 328 recordings from four random patients were used for visual validation of the tbegin algorithm. For comparison of the LAT algorithms, all 3752 electrograms were analyzed. Data is presented as mean ±SD unless otherwise stated. A P value < 0.05 was considered statistically significant. Bland-Altman (BA) plots were constructed to evaluate the variation between the conventional and the new methods. The study was approved by the ethics committee at the University of Ghent.

Algorithm to detect the t_{begin} and t_{end} of the activation complex in B-EGM

An algorithm was developed to detect the beginning (t_{begin}) and end (t_{end}) of the activation complex of the B-EGM. Figure 1 shows a block diagram of the t_{begin} and t_{end} algorithm and the LAT methods. Two main steps can be identified; 1) detection of the t_{begin} and t_{end} of the activation complex, and 2) determination of LAT by three different methods and signal-to-noise ratio (SNR).

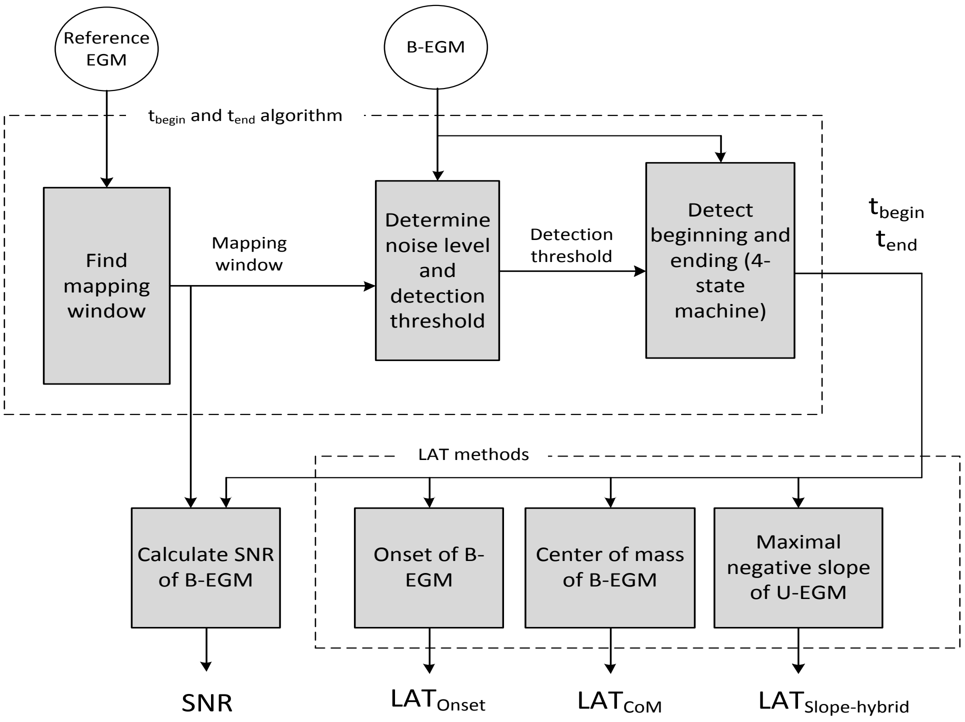

Figure 1-1: *Block diagram of the t_{begin} and t_{end} algorithm and LAT methods. In the t_{begin} and t_{end} algorithm, a mapping window is first determined from the reference electrogram. Then a detection threshold for the B-EGM is estimated. The detection threshold is used in the final step to detect the t_{begin} and t_{end} of the B-EGM by a 4-state machine. LAT methods (LAT_{Onset}, LAT_{CoM}, and $LAT_{Slope-hybrid}$) of the B-EGM are detected and SNR of the B-EGM is calculated using the mapping window, t_{begin}, and t_{end}. B-EGM: bipolar electrogram. U-EGM: unipolar electrogram. LAT: local activation time. CoM: center-of-mass. SNR: signal-to-noise ratio.*

The different steps of the t_{begin} and t_{end} algorithm are plotted in Figure 2 and 3. In the first step (Fig. 2, panel A), an A-wave detection algorithm was used to calculate the A-A intervals in the 2.5s reference recording (i.e. B-EGM recorded at the coronary sinus). The average of A-A intervals was taken as the atrial tachycardia cycle length (ATCL). For each 2.5 seconds recording, the second last complex was analyzed. A mapping window was calculated (ATCL minus 10ms to prevent overlapping from the previous and following beats) and centered around the A peak (i.e. 0ms) on the reference EGM. Next, the detection threshold was determined based upon the B-EGM noise level calculated within the isoelectric windows before and after the complex. To determine the isoelectric windows, first the B-EGM of interest (Fig.2, panel B) was smoothed and rectified using a 2-15 Hz second order bi-directional Butterworth band-pass filter (Fig. 2, panel C). The band-pass 2-15Hz was chosen to remove high frequency components from the signal, thus generating a smoothed signal to clearly identify the isoelectric windows. Then, the minimum signal threshold was calculated as the 5th percentile (P5) of the B-EGM amplitudes plus 20% of the top 95th percentile (P100 - P5) amplitudes (Fig.2 panel D). The intersection points between the minimum signal threshold and the signal were used as markers to demarcate the signal window and (by exclusion) the isoelectric windows before and after the signal complex (Fig. 2, panel E). For all subsequent steps, the original unfiltered B-EGM of interest (Fig. 2 panel B) was differentiated, filtered (second order bidirectional Butterworth band-pass filter 5-300Hz), and rectified (Fig. 2 panel F). The band-pass 5-300Hz was chosen to eliminate low frequency components and preserve the sharp high frequency component of the noise. The noise level was calculated as the maximum peak amplitude in the isoelectric windows (Fig. 2, panel G). Finally, a detection threshold was then calculated as the 98th percentile of the noise level (Fig. 2, panel H).

A 4-state machine algorithm then was used to determine the beginning and the end of the activation complex in the 5-300Hz filtered and rectified B-EGM (Fig. 3 upper panel). Starting at the peak amplitude within the mapping window, the filtered B-EGM was scanned backwards to reach the beginning (t_{begin}) of the complex (Fig. 3, lower left panel). The end of the complex (t_{end}) was detected by reversing the B-EGM and applying the same algorithm (Fig. 3, lower right panel).

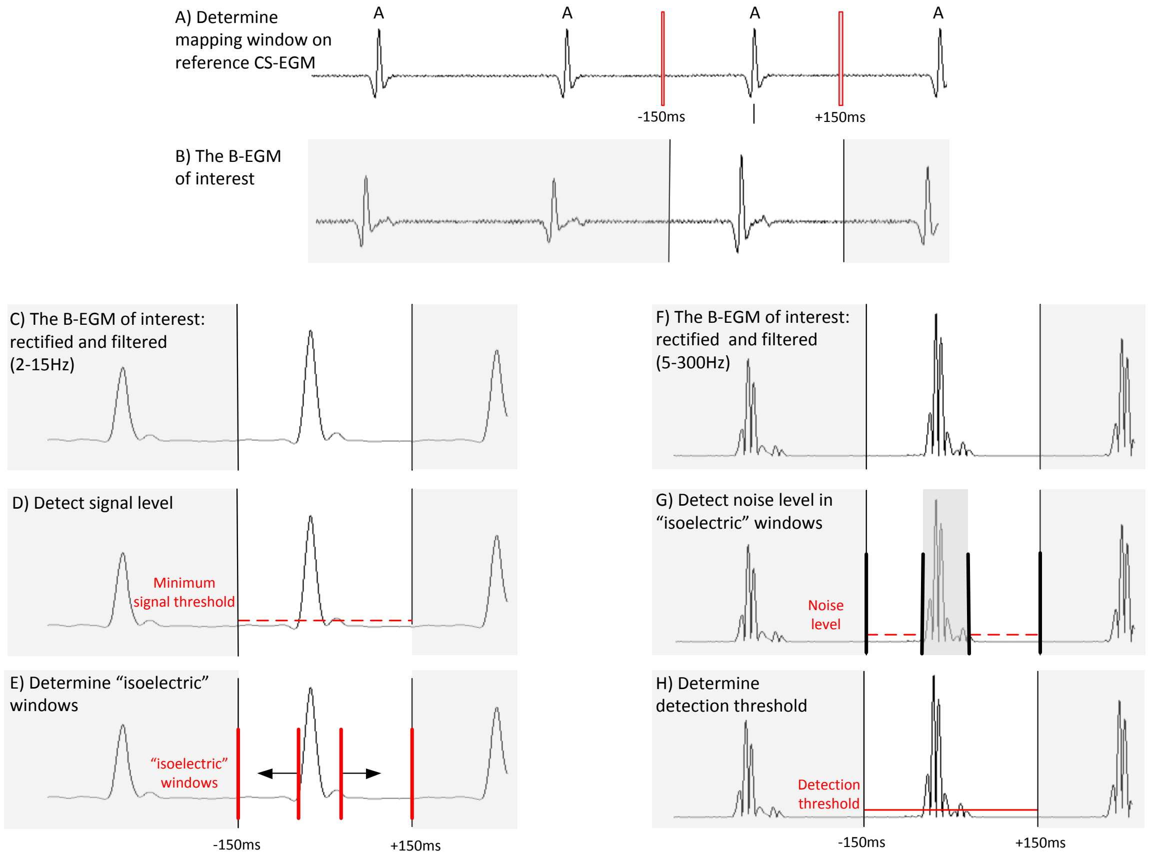

Figure 1-2: *Description of the steps to determine the detection threshold. A) Determining the mapping window on the reference CS electrogram; B) the B-EGM of interest; C) Filtering (2-15Hz) and rectifying the B-EGM of interest; D) Detecting the minimum signal level; E) Determining the isoelectric windows; F) Filtering (5-300Hz) and rectifying the B-EGM of interest; G) Detecting the noise level in isoelectric windows; H) Determining the detection threshold. CS: Coronary sinus. B-EGM: bipolar electrogram.*

The state machine starts and remains in State_A until the detection threshold is underceeded. When crossing the detection threshold, an incremental counter (CNT) is initialized and the state machine moves to State_B. In State_B, back scanning continues as long as the signal is below the detection threshold. When CNT reaches a predefined maximum (CNTSTATE_B), the algorithm moves to State_C. While in State_B, and the signal rises above the detection threshold, the algorithm moves back to State_A. The state machine may switch multiple times between states A and B before switching to State_C. Once in State_C, the state machine cannot switch back to State_B. In State_C, back scanning continues as long as the signal is below the detection threshold and CNT is below CNTSTATE_C. When CNT reaches CNTSTATE_C while the signal is still under the detection threshold, the algorithm terminates and assigns the last detected moment above the detection threshold as the t_{begin}. While in State_C, if the signal crosses the detection threshold, the state machine switches to State_D and a secondary counter (GCNT) is initialized to zero. In State_D, GCNT is incremented as long as the signal remains above the detection threshold. When GCNT reaches the counter preset value (CNTSTATE_D), the state machine moves back to State_A. If the signal crosses the detection threshold while in State_D, the algorithm terminates and assigns the last time instance above the detection threshold as the t_{begin}.

The settings for CNSTATE_B, CNSTATE_C, and CNSTATE_D can be manually adjusted. For the present study, the optimal settings were chosen by trial-and-error in > 500 electrograms and based upon the opinion of the two developing engineers (MEH and RH) who were not involved in the later validation process. The optimal parameters in atrial tachycardia were found to be 8, 16 and 4 respectively.

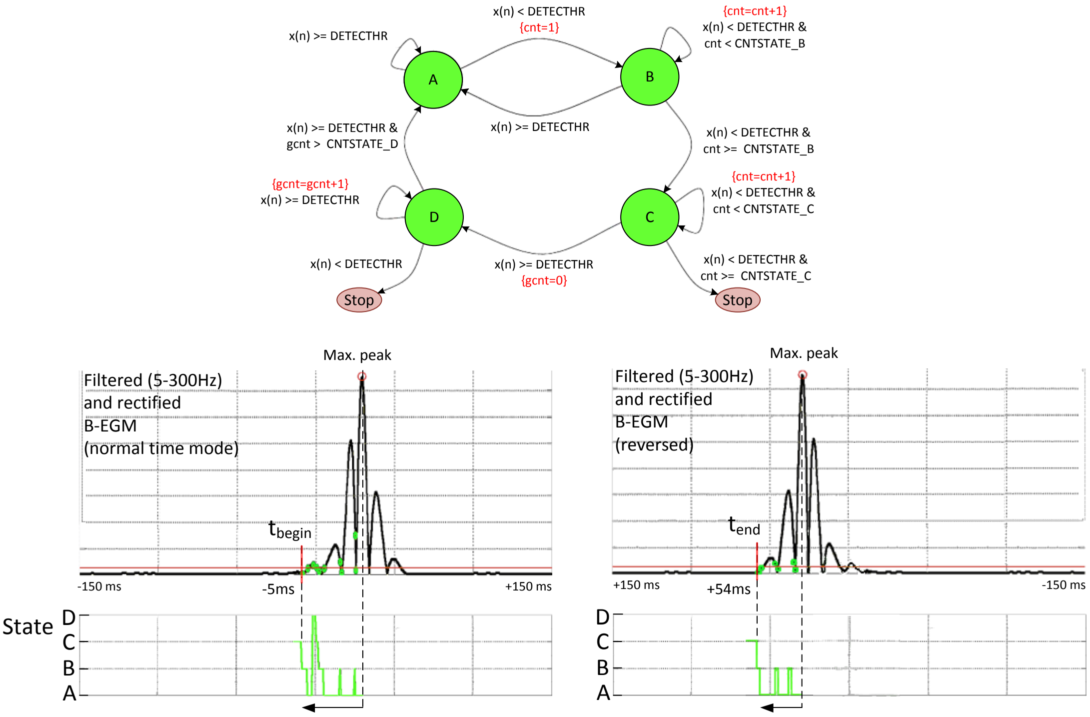

Figure 1-3: *Upper panel: Flowchart of the 4-state machine: the algorithm detects the maximum peak of the signal and scans back to reach the starting moment (t_{begin}) of the complex by moving from one state to the other when the conditions are satisfied (see text for further explanation). Lower panels: filtered and rectified B-EGM with the corresponding 4-state machine annotation. The green circles indicate at which moment of the signal the state is switched. The green line tracks the transition of the algorithm from one state to another. In the left tracing, the B-EGM is analyzed in the normal time mode (to detect t_{begin}), in the right tracing, the B-EGM is analyzed in the reversed mode (to detect t_{end}).*

Onset of the bipolar electrogram (LAT_{Onset})

After detecting the t_{begin} and t_{end} of the activation complex of the B-EGM (Fig. 4, upper panel), the onset of the B-EGM (LAT_{Onset}) was defined as the t_{begin} (Fig. 4 panel A).

Center of mass of the bipolar electrogram (LAT_{COM})

Using the t_{begin} and t_{end} of the activation complex of the B-EGM, the center of mass (LAT_{CoM}) of the 5-300Hz filtered and derived B-EGM was determined. The total ‘mass’ of the signal was calculated as the area under the rectified bipolar signal between t_{begin} and t_{end}. The center of mass was defined as the moment from the t_{begin} where the cumulative area of the signal reaches 50% of the total area between the t_{begin} and t_{end} (Fig. 4, panel B).

Maximal negative slope of the unipolar electrogram within a predefined window ($LAT_{Slope\text{-}hybrid}$)

The maximal negative slope (max. –dv/dt) of the U-EGM ($LAT_{Slope\text{-}hybrid}$), was determined within the narrow time window demarcated by the t_{begin} and t_{end} (Fig. 4, panel C).

Algorithmic quantification of the quality of B-EGM

After identification of the t_{begin} and t_{end} of the complex of the B-EGM, the quality of the B-EGM was determined. The quality was defined by the signal-to-noise ratio (SNR) and was calculated in dB as:

$20 \times log\left[\frac{A_{(S+N)}-A_{(N)}}{A_{(N)}}\right]$ where,

$A_{(S+N)}$ is the root-mean-square (RMS) amplitude of the B-EGM within t_{begin} and t_{end}. $A_{(N)}$ is the RMS amplitude of the B-EGM within the mapping window before t_{begin} and after t_{end} (Fig. 4, lower panel).

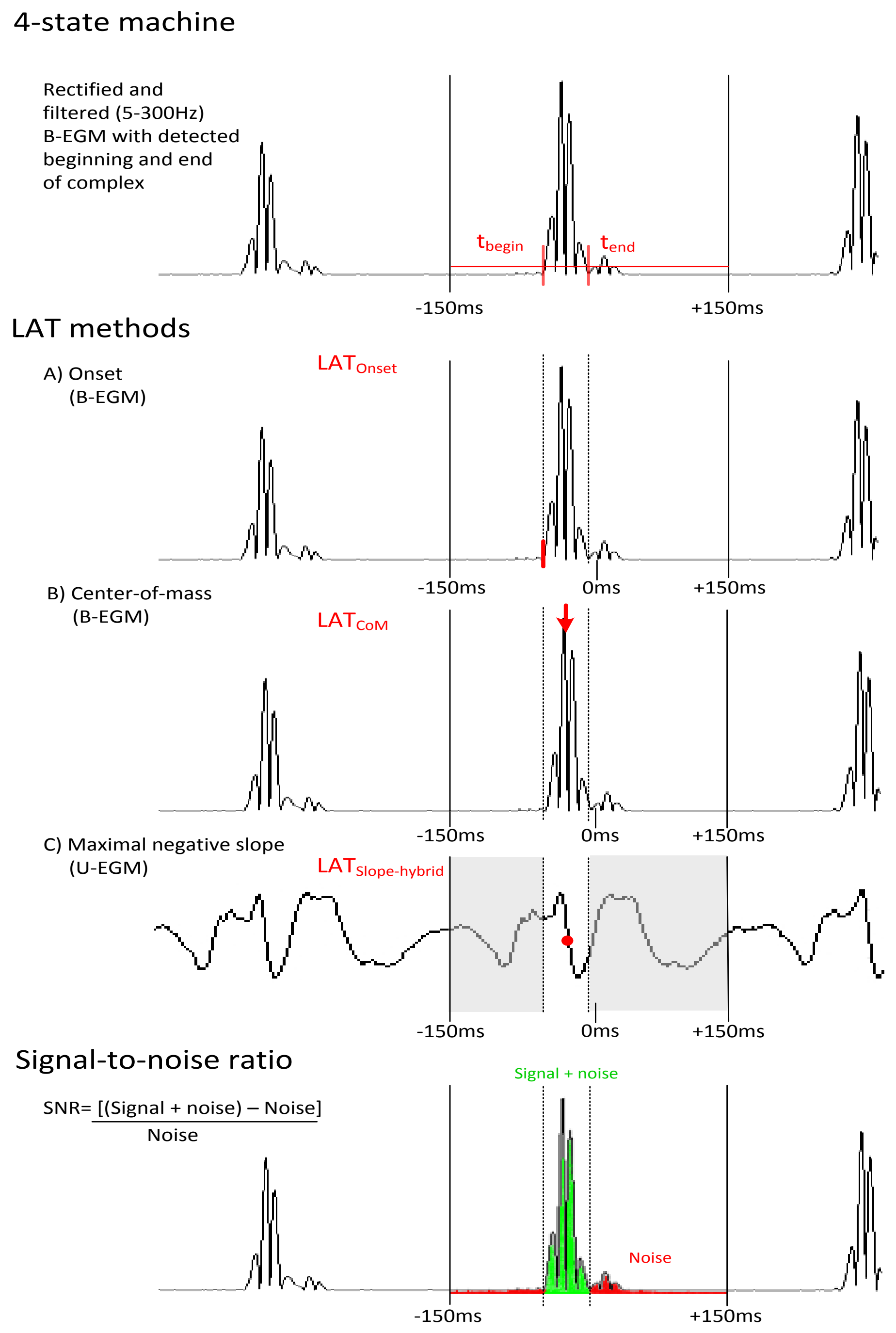

Figure 1-4: *Representative description of LAT detection methods and SNR calculation. LAT_{Onset} (panel A) is defined as the t_{begin} of B-EGM. LAT_{CoM} (panel B) is calculated as the moment from t_{begin} when the signal is 50% of the total cumulative power. $LAT_{Slope\text{-}hybrid}$ (panel C) is calculated as the maximal negative slope of the U-EGM within the window demarcated by the t_{begin} and t_{end}. To calculate SNR (lower panel), the window between the t_{begin} and t_{end} (green) is considered signal plus noise. The windows outside t_{begin} and t_{end} (red) are considered only noise. LAT: local activation time. B-EGM: bipolar electrogram. U-EGM: unipolar electrogram. SNR: signal-to-noise ratio. CoM: center-of-mass.*

Expert analysis of B-EGM

Five experts individually rated the performance of the t_{begin} algorithm. Since both t_{begin} and t_{end} were determined by the same algorithm, rating of the t_{end} was not performed. A grade “Highly accurate” was assigned by the experts when the t_{begin} was detected by the algorithm within ± 5ms. Grade “Accurate” was assigned when the algorithm detects the t_{begin} within ±10ms. Grade “Inaccurate” was assigned when the detection inaccuracy was more than ±10ms. If the expert could not interpret the recording, the EGM was excluded from validation

In addition, the experts classified the B-EGMs into two groups (high- and low confidence). Receiver operating characteristic (ROC) curves of SNR and expert confidence were used to determine the SNR cutoff to detect low confidence EGMs with a specificity of 90%.

1.3 Results

Quality of bipolar electrograms

Analysis of the individual ROC curves revealed a mean SNR cutoff of 13dB (12.8 ± 1.3dB, range 11 to 14 dB) among all experts to discriminate low confidence B-EGM with a specificity of 90%. Based upon this cutoff, 20% (n= 749) of the EGMs were defined as low quality (LQ, SNR<13dB).

Algorithm to detect t_{begin} and t_{end}

Representative examples of high and low quality B-EGMs with their corresponding detection of t_{begin} and results of expert ratings are shown in Fig. 5. As can be seen from

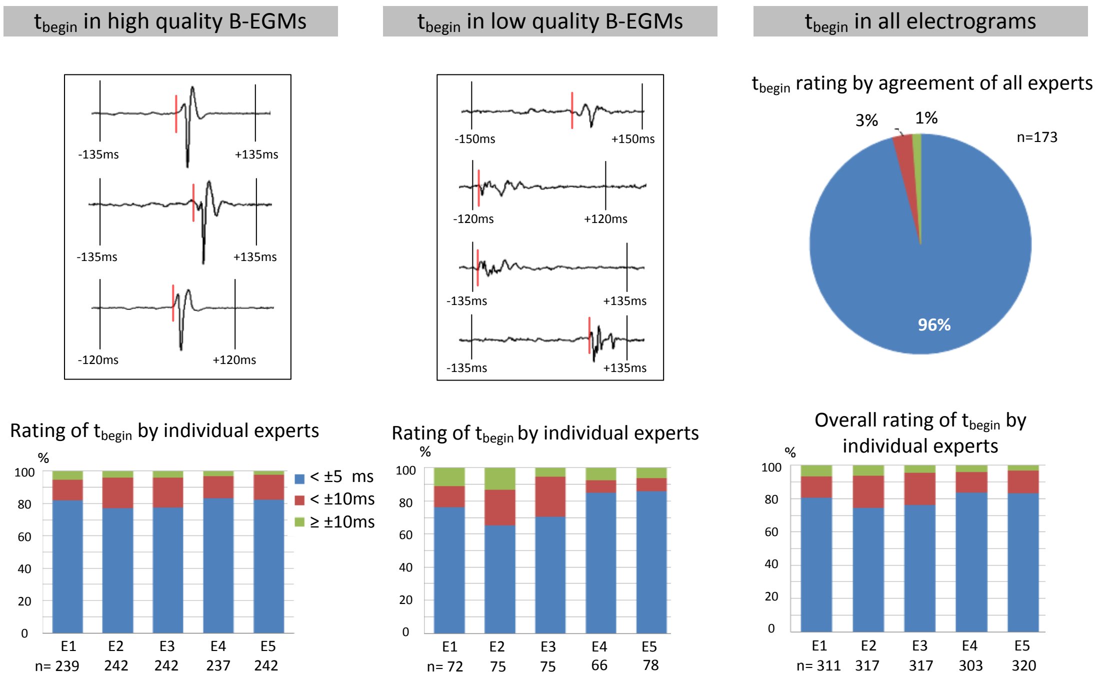

Figure 1-5: Left upper panel: representative high quality B-EGMs with the corresponding tbegin detection (red bar). Left lower panel: results of individual experts' rating of tbegin detection algorithm in HQ electrograms. Middle upper panel: representative low quality B-EGMs with the corresponding tbegin detection (red bar). Middle lower panel: results of individual experts' rating of tbegin detection algorithm in LQ electrograms. Right upper panel: the performance of the tbegin algorithm for B-EGMs which were rated similarly by all experts. Right lower panel: overall performance rating of the tbegin detection by individual experts. HQ: high quality. LQ: low quality. U-EGM: unipolar electrogram. B-EGM: bipolar electrogram.

the HQ B-EGMs (upper left panel), showing a typical triphasic morphology, the t_{begin} detection as obtained from the algorithm shows a good performance. Indeed, the average rating of the algorithm in HQ B-EGMs (lower left panel) was 80 ± 3% within ±5ms (highly accurate), 16 ± 3% within ± 10ms (accurate), and 4 ± 1% more than ± 10ms (inaccurate). Even in LQ B-EGMs (upper middle panel) showing complexes of long duration and low amplitude with multiple peaks, the algorithm accurately detected the t_{begin}. Similarly, the average rating of the algorithm in LQ B-EGMs (lower middle panel) was 77 ± 9% within ± 5ms, 14 ± 8% within ± 10ms, and 9 ± 3% more than ±10ms. The proportion of highly accurate and accurate ratings was not different between HQ and LQ EGMs (80 ± 3% vs 77 ± 9%, p = 0.25 and 16 ± 3% vs 14 ± 8%, p = 0.68 respectively). The proportion of inaccurate rating was significantly different between HQ and LQ (4 ± 1% vs 9 ± 3%, p = 0.02). Overall, on average (lower right panel), the experts graded the algorithm with 80±4% within ±5ms, 15±4% within ±10ms, and 5±2% greater than ±10ms.

Figure 5 upper right panel shows the degree of accuracy of the t_{begin} algorithm in those B-EGMs in which there was agreement in between all experts. There was similar grading of accuracy for 173 (53%) EGMs. For these EGMs, the rating of the algorithm was up to 96% within ±5ms, 3% within ±10ms, and only 1% more than ±10ms.

Methods to assess local activation time: LAT_{Onset}, LAT_{COM}, and $LAT_{Slope-hybrid}$

Figure 6 shows four representative electrograms with the corresponding detection of LAT_{Onset}, LAT_{CoM}, and $LAT_{Slope-hybrid}$. In the upper left panel, a high quality high amplitude triphasic B-EGM is plotted with its corresponding high frequency biphasic U-EGM. In both electrograms, the detection of LAT (LAT_{Onset} and $LAT_{Slope-hybrid}$ respectively, dots) is accurate, though there was a difference of 17ms (-29 vs -12ms) between the two methods. LAT_{CoM} coincided with the $LAT_{Slope-hybrid}$ (-11 vs. -12ms).

In the upper right panel, the B-EGM complex is triphasic with accurate detection of the LAT_{Onset}. The U-EGM is disturbed by far-field potentials with multiple slopes making detection of the maximal negative slope by visual annotation or by a conventional –dV/dt algorithm inaccurate. Using the bipolar window of interest demarcated by t_{begin} and t_{end}, however, blanks far-field potentials and enables more reliable detection of the maximal negative slope (LAT$_{\text{Slope-hybrid}}$). Again, LAT$_{\text{CoM}}$ and LAT$_{\text{Slope-hybrid}}$ coincide (79 vs 74ms), both 20ms later than LAT$_{\text{Onset}}$ (55ms).

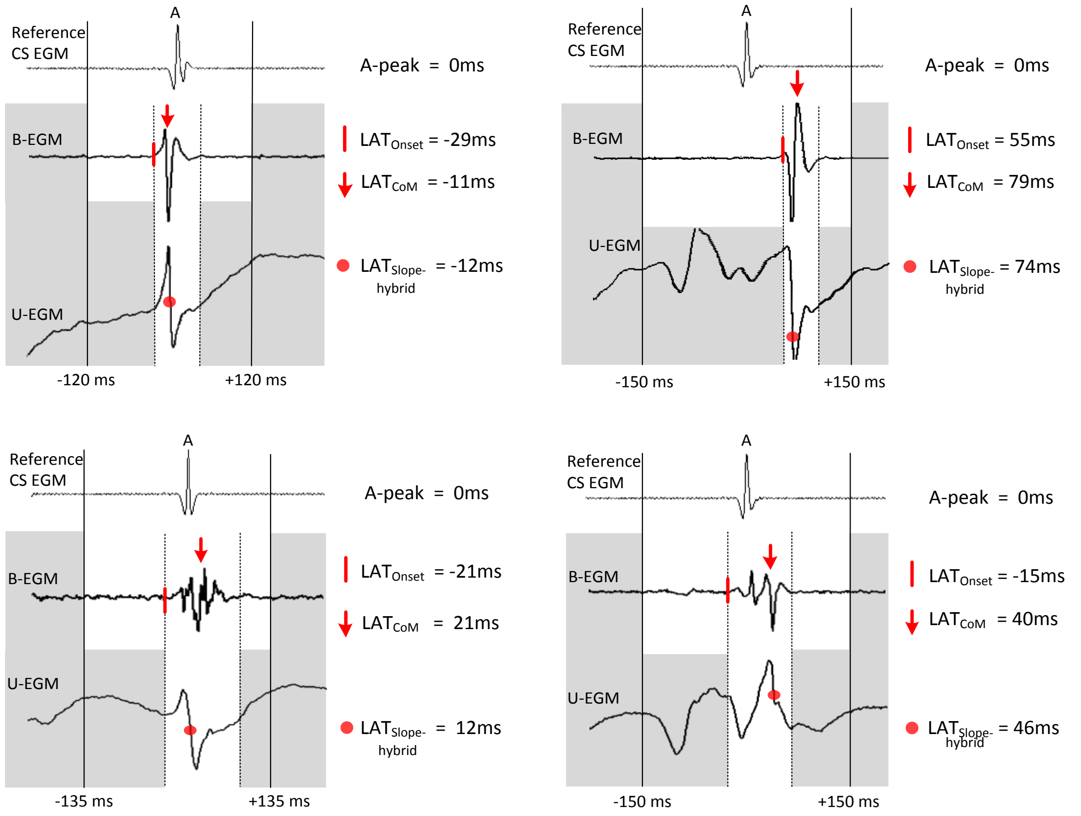

Figure 1-6: *Representative B-EGM and U-EGM with the corresponding detection of LAT$_{\text{Onset}}$ (red line), LAT$_{\text{CoM}}$ (arrow), and LAT$_{\text{Slope-hybrid}}$ (dot). See text for explanation. LAT: local activation time. B-EGM: bipolar electrogram. U-EGM: unipolar electrogram. CoM: center-of-mass.*

In the lower left panel, a fractionated (multiple peaks) low amplitude B-EGM of long duration is shown. LAT$_{\text{Onset}}$ accurately detects the unique moment of the onset of the B-EGM (-21ms). Interestingly, in contrast to the B-EGM, the U-EGM is characterized by one single high frequency biphasic potential, with straightforward detection of the maximal negative slope. The LAT$_{\text{Slope-hybrid}}$ slightly differs from the LAT$_{\text{CoM}}$ (12 vs. 21ms respectively).

In the lower right panel, a fractionated and long duration B-EGM is plotted. Now the U-EGM reveals multiple slopes. LAT_{Onset} proceeds LAT_{CoM} by 55ms (-15 vs. 40ms). Detection of the maximal negative slope of the U-EGM was only possible due to blanking of the far-field potentials. The $LAT_{Slope-hybrid}$ suggests that the true moment of activation occurs late relative to the onset of the B-EGM (46ms).

Conventional versus new LAT methods

The conventional LAT method in B-EGM was determined as the maximal positive peak within the full mapping window (LAT_{Peak}). In U-EGM, the conventional LAT method was determined as the maximal negative slope (max. – dV/dt) within the full mapping window (LAT_{Slope}). Figure 7 shows the Bland-Altman (BA) plots of the conventional methods vs. the new methods to calculate the LAT.

Comparing LAT_{Onset} to LAT_{Peak}, the BA plot shows a mean of difference (bias) between LAT_{Peak} and LAT_{Onset} of 27ms with a variation (2xSD) of 30ms for HQ electrograms (upper left panel), and 24±62ms for LQ electrograms (lower left panel). It is evident that the bias is explained by the nature of the methods (by definition, the onset will precede the peak). The variation on the other hand, is expected to be due to ambiguity of peak detection. This is supported by our data showing an increased variation in LQ electrograms (multiple peaks) compared to HQ electrograms.

Comparing LAT_{CoM} to LAT_{Peak}, the BA plot shows a mean of difference (bias) between LAT_{Peak} and LAT_{CoM} of 0ms with a variation (2xSD) of 16ms for HQ electrograms (upper middle panel), and 2±38ms for LQ electrograms (lower middle panel). Interestingly, the zero bias reveals that the moment of the CoM coincides with the moment of the peak; suggesting that the energy of the signal is symmetrically distributed around the peak. Again, the variation is due to ambiguity of peak detection.

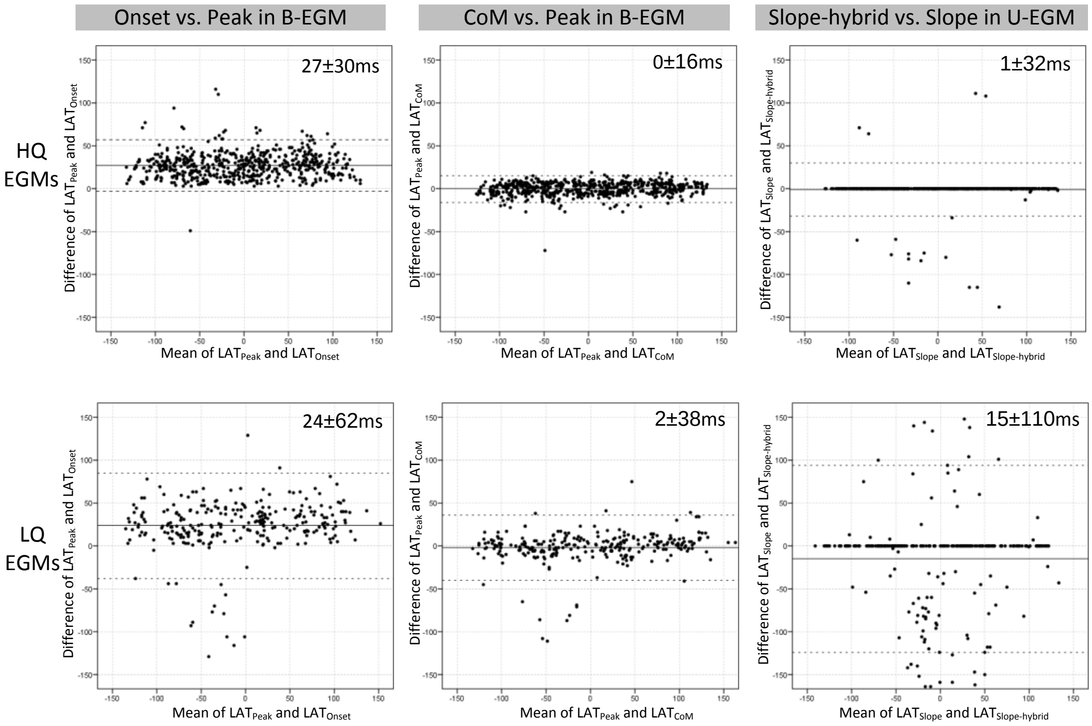

Figure 1-7: *Bland-Altman plots of conventional methods versus the new methods to assess LAT for high (upper panels) and low quality (lower panels) electrograms. See text for explanation. LAT: local activation time. B-EGM: bipolar electrogram. U-EGM: unipolar electrogram. CoM: center-of-mass. HQ: high quality. LQ: low quality.*

In the right panels, BA plots are shown comparing LAT$_{\text{Slope}}$ and LAT$_{\text{Slope-hybrid}}$. It is evident from both BA plots that LAT$_{\text{Slope}}$ and LAT$_{\text{Slope-hybrid}}$ either show exactly the time instant related to the same slope, or large deviations resulting from erroneous slope detection by LAT$_{\text{Slope}}$. In HQ electrograms, the percentage of LAT$_{\text{Slope}}$ values deviating from LAT$_{\text{Slope-hybrid}}$, i.e. absolute difference > 0ms was 4%. As expected, due to the less steep slope of the U-EGM and more far-field potentials in LQ electrograms, this percentage increased to 33% in LQ electrograms.

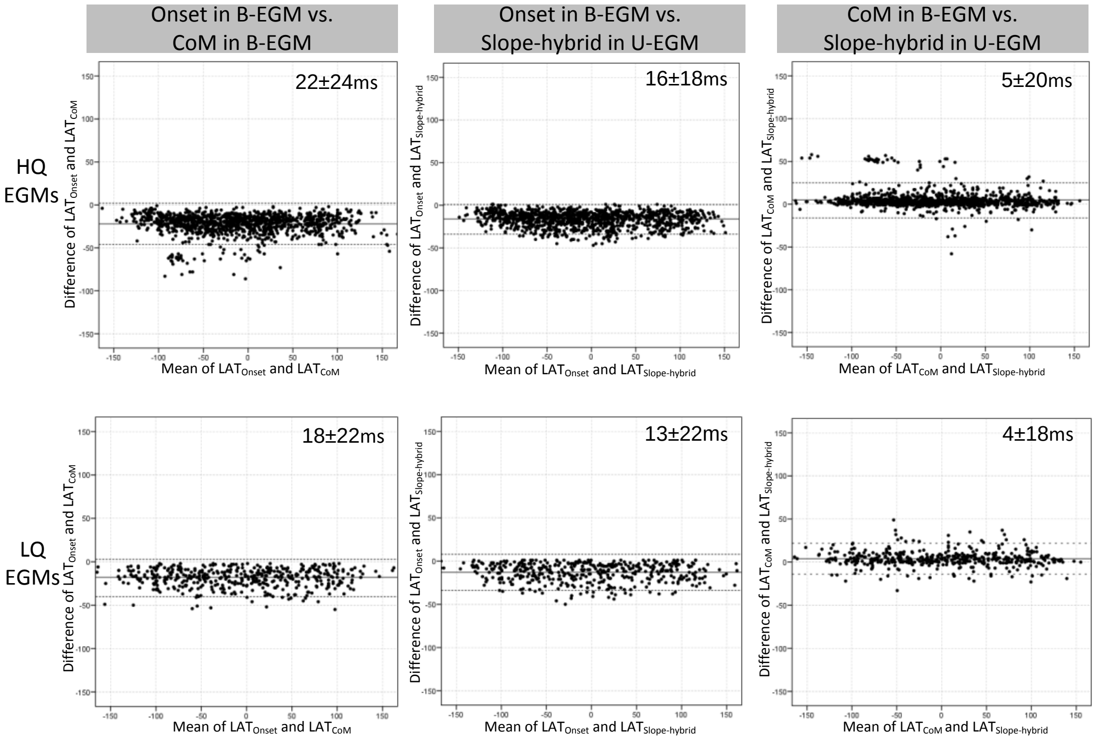

Figure 1-8: *Bland-Altman plots of new methods to assess LAT for high (upper panels) and low quality (lower panels) electrograms. See text for explanation. LAT: local activation time. B-EGM: bipolar electrogram. U-EGM: unipolar electrogram. CoM: center-of-mass. HQ: high quality. LQ: low quality.*

Comparison of new LAT methods

The new methods to assess LAT were compared to one another (Figure 8). In HQ EGMs, the LAT_{Onset} and LAT_{CoM} in B-EGMs showed mean difference of 22 ± 24ms (upper left panel). When compared to $LAT_{Slope\text{-}hybrid}$ in U-EGMs, the LAT_{Onset} in B-EGM showed a mean difference of 16 ± 18 ms (upper middle panel). Interestingly, comparing LAT_{CoM} in B-EGMs to $LAT_{Slope\text{-}hybrid}$ in U-EGMs, the BA plots showed a mean difference (bias) of only 5 ms, with a variation of 20 ms (upper right panel). This small difference indicates that LAT as determined by CoM and slope-hybrid coincides. In LQ EGMs, BA plots revealed similar results to HQ EGMs for all comparisons (lower panels).

The variation in difference between LAT_{Onset} vs. LAT_{CoM} (22ms) was less compared to LAT_{Onset} vs. LAT_{Peak} (62ms). This supports the hypothesis that the ambiguity of peak detection rather than changes in local conduction is causing the variation.

1.4 Discussion

Main findings

We developed a new algorithm to reliably detect in both low and high-quality electrograms the beginning (t_{begin}) and the end (t_{end}) of the activation complex of the B-EGM. This algorithm allows the introduction of new methods to assess local activation time in unipolar ($LAT_{Slope-hybrid}$) and bipolar (LAT_{Onset}, LAT_{CoM}) electrograms.

In B-EGM, compared to the conventional peak detection method, LAT_{Onset} and LAT_{CoM} detect a different fiducial marker which is potentially less ambiguous, especially in low quality electrograms. The $LAT_{Slope-hybrid}$ method is a new 2-step approach (using blanking of the far-field potentials) to detect the maximal negative slope in U-EGM. This method is potentially superior to the conventional maximal negative slope method, especially in LQ electrograms.

Conventional methods to assess local activation time

Mapping of arrhythmias requires accurate detection of the local activation time, denoting the instant in time the activation wave is passing under the recording electrode. Spach et al.[1, 2] showed that the maximal negative slope in U-EGM is the most accurate parameter associated with the activation of cardiac tissue underneath the electrode. A clear limitation of unipolar EGMs for the assessment of the local activation time is the presence of far-field potentials.[3]

Although filtering can be used to differentiate local from far-field potentials in U-EGMs,[7] far-field potentials in clinical recordings remain a clear limitation for the implementation of unipolar EGMs in the assessment of local activation time. In bipolar electrograms, the maximal positive and/or negative peak and the maximal negative slope (-dV/dt) have been used as fiducial markers for LAT.[4,5,8,9] B-EGM morphology, however, is the result of subtraction of the unipolar electrograms recorded from the tip and ring electrode and as such is influenced by wavefront direction, bipole orientation, electrode size, and inter-electrode spacing.[6] In the case of a broad propagating wavefront, the B-EGM will record a triphasic complex with one single clearly identifiable peak. More complex activation of the myocardium on the other hand will introduce multiple peaks and more ambiguity to correctly identify the activation time. Although in unipolar electrograms, the steepest slope is related to the upstroke of the action potential and moment of activation,[1,2] this will not hold for bipolar electrograms since these signals are the result of subtraction of two unipolar electrograms which generates multiple artificial slopes not related to wavefront propagation.

New algorithm to detect the beginning and end of the activation complex in B-EGM

Detection of the beginning of the bipolar electrogram complex requires an accurate and dynamic detection threshold. To define an accurate detection threshold, the signal complex was excluded after heavy filtering and a noise level was determined for the windows before and after the signal components (i.e. “isoelectric windows”). This noise level which varies among electrograms was then used to determine a dynamic detection threshold. It is expected that such threshold is superior to fixed thresholds or other dynamic thresholds which simply are calculated as a certain percentile of the maximum amplitude of the signal. The concept of using dynamic multi-thresholds has been previously used in an algorithm to detect and discriminate atrial from ventricular activations in epicardic U-EGMs recorded from the human atria.[7] It was shown that the performance of detection was optimal when using two thresholds. Moreover, the variation of the thresholds over time within the same patient and as well as between patients, suggests the necessity of using dynamic thresholds.[7] In the present study, we used a first threshold to intersect with the signal at low level amplitude (i.e. at minimum signal level) in order to contain above it utmost signal amplitude. This threshold was set to 5% of the maximum amplitude of the signal. To enhance the threshold, we raised it by a proportion equals to 20% of the top 95% amplitude of the signal. A second threshold (detection threshold) which was used for the detection of tbegin and tend was set to 98% of the noise level (i.e. maximum amplitude within the isoelectric windows). These values were chosen by trial-and-error and were specific for AT.

The detection threshold is then used by a state-machine enabling a structured way to detect the beginning and the end of the complex. Since each state can be labeled with a specific meaning, only conditions need to be defined for each state to determine the next state. When encountering an exit state, the t_{begin} of the bipolar complex will be found. Additionally, the 4-state machine was designed to be programmable. Pre-specified counters for each state indicate how much time the machine is allowed to stay in that specific state. These counter parameters can be tweaked to yield better performance and adjusted to detect or exclude several physiological components of the bipolar electrograms such as double potentials and far-field residuals. In the current study we validated the algorithm to get the optimal performance using specific preset parameters based upon our experience, however, the algorithm remains an open system which can be tailored according to the acquisition and electro-anatomical mapping equipment.

New methods to assess local activation time

In the current study we introduced three new methods to assess the local activation time (LAT_{Onset}, LAT_{CoM}, and $LAT_{Slope\text{-}hybrid}$) within the window demarcated by the t_{begin} and t_{end}.

The onset of the bipolar electrogram (LAT_{Onset}) as proposed in this study was defined as the beginning of the bipolar electrogram complex. In prior clinical studies reporting the onset of the bipolar electrograms as a marker for the assessment of the local activation time,[9,10,11,12] annotations were performed manually. Paul et al[9] used the onset of B-EGM for the assessment of the LAT and reported that the activation times were earlier by 10 to 12ms; thus introducing misinterpretation in the timing and location of the earliest activation time.[9] However, more recent studies,[10,11,12] showed that using onset of B-EGM to assess LAT is useful to guide ablation especially in focal tachycardias. We hypothesized that compared to the conventional peak detection; the new onset method has the major advantage of detecting a single, unambiguous, and unique moment in the bipolar electrogram. This hypothesis was underscored by our comparison of both methods in low quality electrograms. On the other hand, despite the unambiguous and intuitive nature of LAT_{Onset}, it should be interpreted with vigilance because the onset does not necessary reflect the true moment of activation.[9] As the beginning of the activation complex of the B-EGM reflects the first activation recorded by either the tip or the ring of the bipolar electrode, it might pick up distant activation waves approaching and travelling away from the recording electrodes ("far-field residuals"). Apart from a time delay, the unipolar near- and far-field components will have different morphologies. When the tip is in contact with the myocardium and the ring is floating in blood, the downward slope of the electrogram recorded from the ring will be of longer duration with a less steep slope. Far-field components will also be represented differently in the tip and ring electrodes due to various factors including distance, contact force and electrode shape and area. As a result of subtraction, the morphology of the bipolar complex will be influenced by these factors. Far-field residuals will emerge from subtraction of different unipolar far-field components concealing the true onset of the bipolar complex.

The concept of center of mass - a morphology rather than single point based approach - has been previously introduced and validated to estimate the local activation time in B-EGMs.[13,14,15,16] In the studies by Holm et al, Faes et al, and Sandirini et al, local activation times on B-EGMs recorded during human atrial fibrillation were assessed using the center of mass method (termed “local barycenter”) and the conventional methods (maximum peak and slope). Compared to expert annotation, the COM showed superiority over the conventional methods especially in multi-peak, fragmented, and complex B-EGMs.[13,14,15] Similarly, Pieper et al showed in an experimental and clinical setting, that compared to unipolar slope detection, a morphology based approach (similar to COM) in B-EGMs is more accurate to assess local activation time than the conventional algorithms in B-EGMs (peak and slope). [16] The concept of CoM was also validated in the analysis of the surface electrogram and

U-EGMs.[7,17] Moody et al showed that a morphology-based approach (similar to COM) can be used for QRS detection,[17] whereas Dube et al showed that the COM in U-EGMs (called the "median energy") coincided (difference of 2ms) with the maximum negative slope in AF recordings.[7] The center of mass may be a good alternative for conventional LAT methods since there is equal signal energy before and after the CoM (i.e. same wave propagates towards and away from the electrode, therefore the midst energy moment is when the wave is underpassing the electrode). As the center of mass is not based upon a single data-point, it is less sensitive to morphology variation. On the other hand, this method is strictly a computational parameter that cannot be visually validated. Our data show that LAT_{CoM} provides another marker than the peak and is potentially less ambiguous especially in low quality electrograms. The observation that the activation time determined by LAT_{CoM} almost coincides with the maximal unipolar slope (5ms), furthermore supports its physiological sense and clinical validity. As such, it might be superior to the conventional LAT methods and therefore, should be tested in clinical applications.

The maximal negative slope of unipolar electrograms within a predefined window as proposed in this study combines the analysis of the bipolar and unipolar electrograms ($LAT_{Slope\text{-}hybrid}$). The maximal negative slope of unipolar electrograms has been proved experimentally to coincide with the upstroke of the action potential.[1,2] However, due to presence of far-field potentials, it is not commonly used in daily clinical practic.[3] In the proposed new method however, the steepest negative slope is detected only within the bipolar window demarcated by the beginning and the end of the activation complex. This way of time-filtering of the unipolar data prevents detection of erroneous slopes not related to underpassing of the activation wavefront. This two-step approach was shown to blank effectively far-field potentials in the unipolar electrograms. When compared to the conventional slope method, our data suggested incremental benefit of the new method especially in LQ electrograms.

Limitations

In the present study we only validated the t_{begin} and t_{end} algorithm with one pre-defined set of parameters for the 4-state machine (8, 16, and 4 for state counters B, C, and D respectively). Changing those parameters is expected to alter the accuracy of the algorithm.

The new methods to assess activation time in B-EGMs (LAT_{Onset} and LAT_{CoM}) were compared to the LAT_{Peak} method. This latter method however has its limitations (see above) and will, by definition, give other values than the new algorithms (e.g. onset consistently earlier than peak). On the other hand, peak detection so far is considered the most objective and reproducible automated tool to assess LAT in B-EGMs.

Clinical implications

Visual and manual assessment of LAT is time consuming and subjective. This is a main limitation especially in patients with multiple AT and in case of new mapping systems acquiring multiple recordings simultaneously (non-contact mapping and multi-electrode catheters). Therefore, automated annotation of the LAT is required. The current proposed methods (LAT_{Onset}, LAT_{CoM}, and $LAT_{Slope-hybrid}$) were executed with low computational time. Because this is expected to be similar using other platforms and systems, they can be implemented in mapping systems. Further investigation is warranted to determine whether they have incremental benefits over the conventional methods. It is tempting to speculate that different methods have different values according to the type of AT (focal source vs. macroreentry tachycardia). These methods might also be useful in mapping other arrhythmias such as ventricular tachycardias or atrial fibrillation.

1.5 References

1. Spach MS, Miller WT, III, Miller-Jones E, Warren RB, Barr RC. Extracellular potentials related to intracellular action potentials during impulse conduction in anisotropic canine cardiac muscle. CircRes 1979;45:188-204.

2. Spach MS, Dolber PC. Relating extracellular potentials and their derivatives to anisotropic propagation at a microscopic level in human cardiac muscle. Evidence for electrical uncoupling of side-to-side fiber connections with increasing age. CircRes 1986;58:356-71.

3. Stevenson WG, Soejima K. Recording techniques for clinical electrophysiology. J Cardiovasc Electrophysiol. 2005;16:1017-22.

4. De Bakker JMT, Hauer RNW, Simmers TA: Activation mapping: Unipolar versus bipolar recording. In: Zipes DP, Jalife J, eds: Cardiac Electrophysiology. From Cell to Bedside. Second Edition. Philadelphia , PA : W.B. Saunders, 1995, p. 1068.

5. Biermann M, Sheanasa M, Borggrefe M, et al. The interpretation of cardiac electrograms. In: Sheanasa M, Borggrefe M, Breithardt G, eds. Cardiac Mapping. New York, NY: Futura Publishing; 1993: 11–34.

6. Ndrepepa G, Caref EB, Yin H, el-Sherif N, Restivo M. Activation time determination by high-resolution unipolar and bipolar extracellular electrograms in the canine heart. J Cardiovasc Electrophysiol. 1995;6:174-88.

7. Dubé B, Vinet A, Xiong F, Yin Y, LeBlanc AR, Pagé P. Automatic detection and classification of human epicardial atrial unipolar electrograms. Physiol Meas. 2009;30:1303-25.

8. Shah, D. C., Haissaguerre, M., Jais, P., Clementy, J. High-resolution mapping of tachycardia originating from the superior vena cava: evidence of electrical heterogeneity, slow conduction, and possible circus movement reentry. Journal of Cardiovascular Electrophysiology. 2002;13:388–392.

9. Paul T, Moak JP, Morris C, Garson A Jr. Epicardial mapping: how to measure local activation? Pacing Clin Electrophysiol. 1990;13:285-92.

10. Kalman JM, Olgin JE, Karch MR, Hamdan M, Lee RJ, Lesh MD. "Cristal tachycardias": origin of right atrial tachycardias from the crista terminalis identified by intracardiac echocardiography. J Am Coll Cardiol. 1998;31:451-9.

11. Weiss C, Willems S, Rueppel R, Hoffmann M, Meinertz T. Electroanatomical Mapping (CARTO) of ectopic atrial tachycardia: impact of bipolar and unipolar local electrogram annotation for localization of the focal origin. J Interv Card Electrophysiol. 2001;5:101-7.

12. Volkmer M, Antz M, Hebe J, Kuck KH. Focal atrial tachycardia originating from the musculature of the coronary sinus. J Cardiovasc Electrophysiol. 2002;13:68-71.

13. Holm M, Johansson R, Olsson SB, Brandt J, Lührs C. A new method for analysis of atrial activation during chronic atrial fibrillation in man. IEEE Trans Biomed Eng. 1996:43:198-210.

14. Faes L, Nollo G, Antolini R, Gaita F, Ravelli F. A method for quantifying atrial fibrillation organization based on wave-morphology similarity. IEEE Trans Biomed Eng. 2002:49:1504-13.

15. Sandirini L, Faes L, Ravelli F, Antolini R, Nollo G. Morphology-based measurements of activation time in human atrial fibrillation. Computers in Cardiology 2002:29:593-96.

16. Pieper CF, Blue R, Pacifico A. Simultaneously collected monopolar and discrete bipolar electrograms: comparison of activation time detection algorithms. Pacing Clin Electrophysiol. 1993:16:426-33.

17. Moody G, Mark R: QRS Morphology Representation and Noise Estimation using the Karhunen-Loève Transform. Computers in Cardiology 1989:269-272.

CHAPTER 2

Novel algorithmic methods in mapping of atrial and ventricular tachycardia

Milad El Haddad, MS; Richard Houben, PhD; Roland Stroobandt, MD, PhD; Frederic Van Heuverswyn, MD; Rene Tavernier, MD, PhD; Mattias Duytschaever, MD, PhD

This original research article was published in the journal Circulation: Arrhythmia and Electrophysiology volume 7, issue 3, pages 463-472 in June 2014

Abstract

Background: Conventional methods to assess local activation time (LAT) detect the peak of the bipolar electrogram (B-EGM, B-LAT$_{Peak}$) or the maximal negative slope of the unipolar electrogram (U-EGM, U-LAT$_{Slope}$). We evaluated three novel methods to assess LAT: onset (B-LAT$_{Onset}$) and center of mass (B-LAT$_{CoM}$) of B-EGM, and maximal negative slope of U-EGM within a predefined bipolar window (U-LAT$_{Slope-hybrid}$).

Methods and Results: In 1,753 AT and 1,426 VT recordings, the performance of the methods in detecting LAT was evaluated paired-wise (e.g. B-LAT$_{Peak}$ vs. B-LAT$_{Onset}$). For each comparison, histogram analysis of the differences in LAT values was performed. Variation in differences (P95-P5) in low quality (LQ) was compared to high quality (HQ) EGMs. In a separate dataset (12 AT and 10 VT) we evaluated for each method the accuracy in algorithmic activation mapping.

Both in AT and VT, the variation in difference between the conventional and the novel methods was larger in LQ EGMs. In contrast, variation in difference between the novel methods was comparable in LQ and HQ EGMs. Except for LAT$_{Slope-hybrid}$, all methods showed decreased mapping accuracy with increasing percentage of LQ EGMs. U-LAT$_{Slope-hybrid}$ accurately mapped activation in 16 out of 22 maps (vs. B-LAT$_{CoM}$, 14; B-LAT$_{Peak}$, 14; B-LAT$_{Onset}$, 13; U-LAT$_{Slope}$, 4).

Conclusions: In LQ atrial and ventricular electrograms, the novel LAT methods (B-LAT$_{Onset}$, B-LAT$_{CoM}$, and U-LAT$_{Slope-hybrid}$) show less variation than the conventional methods. The U-LAT$_{Slope\ hybrid}$ -a hybrid method which accurately detects the maximal negative unipolar slope- is associated with the highest accuracy in algorithmic mapping of AT/VT.

2.1 Introduction

Mapping of arrhythmias requires accurate detection of the local activation time (LAT) in unipolar (U-EGM) or bipolar electrograms (B-EGM). The maximal negative slope (-dV/dt) of the U-EGM coincides with the upstroke of the action potential (i.e. the true moment of activation).[1,2] U-EGMs are susceptible to noise and far-field potentials and are therefore not often used in clinical practice.[3] In B-EGMs, the peak and the maximal –dV/dt are used as fiducial LAT markers.[4,5,6,7,8] B-EGM morphology however, is influenced by wavefront direction, bipole orientation, electrode size, and inter-electrode spacing.[9] As such, assessment of LAT based upon B-EGMs, can introduce ambiguity, especially in low-voltage EGMs with multiple peaks.

Recently we validated an automated algorithm which reliably detects the beginning (t_{begin}) and end (t_{end}) of the B-EGM.[10]

In the present study, we evaluated three novel methods to determine LAT based upon the t_{begin} and t_{end} algorithm: 1) the onset of B-EGM (B-LAT_{Onset}), 2) the center of mass of B-EGM (B-LAT_{CoM}), and 3) the maximal -dV/dt of U-EGM within the time window demarcated by t_{begin} and t_{end} (U-$LAT_{Slope\text{-}hybrid}$). First we evaluated the performance of LAT methods in detecting the moment of activation in both high quality (HQ) and low quality (LQ) atrial and ventricular EGMs. Second we evaluated in another dataset their accuracy in algorithmic activation mapping of atrial (AT) and ventricular tachycardia (VT). Finally, for validation, we provided preliminary results on ablation of AT guided by U-$LAT_{Slope\text{-}hybrid}$.

2.2 Methods

Database of electrograms

We analyzed 1,753 and 1,426 recordings from 31 AT and 23 VT patients (Table 1). All patients had undergone endocardial CARTO-guided ablation using an irrigated ablation catheter with a 3.5mm tip and three 1mm-ring electrodes (2-5-2mm, Navistar® Thermocool, Biosense-Webster, Diamond Bar, CA, USA).

Table 2.1: *Clinical characteristics of AT and VT patients (mapping dataset)*

	AT (n=12)	**VT** (n=10)
Age, yrs	60±13	66±10
Males, n (%)	7(58%)	8(80%)
Structural heart disease, n (%)	11(92%)	9(90%)
Hypertension, n (%)	1(8%)	4(40%)
Hypercholesterolemia, n (%)	1(8%)	8(80%)
Diabetes, n (%)	2(17%)	0(0%)
CHA_2DS_2-VAS_C	2±1.3	2.6±1.5
NYHA Class I, n (%)	10 (83%)	0 (0%)
NYHA Class II, n (%)	1 (8%)	4 (40%)
NYHA Class III, n (%)	1 (8%)	6 (60%)
Left atrial diameter, mm	45±5	N/A
Atrial fibrillation, n(%)	5(42%)	2(20%)
LVEF %	N/A	31±21
ICD, n(%)	0(0%)	8(80%)
Prior ADT, n(%)	9(75%)	9(90%)
Prior ablation, n(%)	7(58%)	3(30%)
Prior cardiac surgery, n(%)	7(58%)	2(20%)

AT: atrial tachycardia, VT: ventricular tachycardia; LVEF: left ventricular ejection fraction; ICD: implantable cardioverter defibrillator; ADT: anti-arrhythmic drug treatment; N/A: not available.

Prior to ablation, point-by-point mapping (122±45 points) was performed. We ensured a stable position (>3s), and a homogeneous spatial distribution of the recorded EGMs. In AT, a bipole of a coronary sinus catheter was selected as reference for activation mapping (A peak =0ms). In VT, a surface-ECG lead was selected as reference (R peak =0ms). At each site, a U-EGM (tip, filtered 0.5-500Hz) and B-EGM (tip minus ring, filtered 30-240Hz) were recorded for 2.5 seconds (sampled at 1000Hz).

Ablation then was performed by targeting the area of earliest activation (if focal activation), the core of a spiral wave (if rotor-like activation) or the critical isthmus (if macro-reentry).

All EGMs were exported for offline analysis in Matlab v7.10 (The MathWorks, Inc., Natick, MA, USA). The study was approved by the ethics committee at Ghent University.

Beat of interest and its mapping window

By default, Carto assigns the 2nd last beat of the recording as the beat of interest. For that given beat, we routinely set a mapping window equal to the tachycardia cycle length minus 10ms, symmetrically positioned around the reference A or R peak. In Matlab, we analyzed the same beat together with its mapping window.

Quality of B-EGMs

Algorithmic quantification of the quality of the B-EGMs was previously described.[10] Compared to visual classification of quality, SNR cutoff to detect LQ EGMs with 90% sensitivity was 13dB and 9dB in AT and VT respectively.

Conventional LAT methods

$\text{B-LAT}_{\text{peak}}$ was calculated as the maximal positive bipolar peak within the full mapping window. $\text{U-LAT}_{\text{slope}}$ was based upon the maximal unipolar -dV/dt within the full mapping window.

Novel LAT methods

$\text{B-LAT}_{\text{Onset}}$ was defined as the t_{begin} of B-EGM. $\text{B-LAT}_{\text{CoM}}$ was calculated as the moment when the cumulative area of the signal reached 50% of the total area between t_{begin} and t_{end}. $\text{U-LAT}_{\text{Slope-hybrid}}$ (a hybrid method based upon both the B-EGM and U-EGM) was defined as the maximal unipolar -dV/dt within the time window demarcated by the t_{begin} and t_{end}.

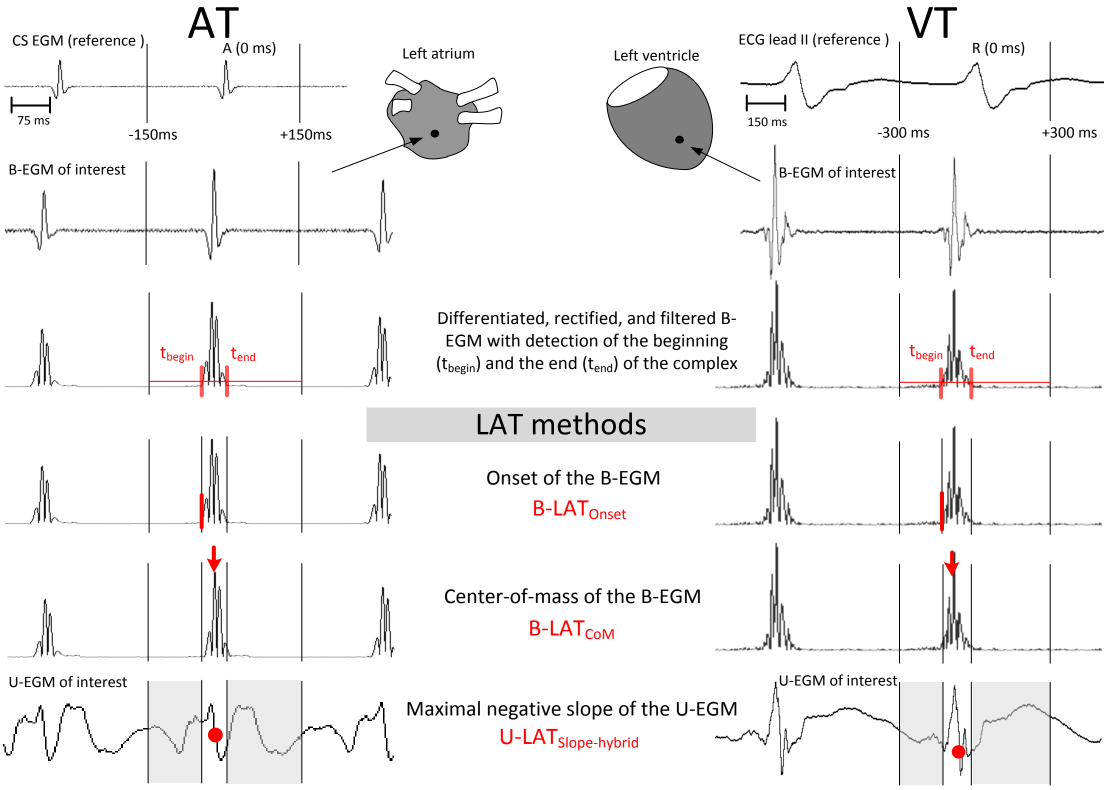

Figure 2-1: *The novel algorithmic methods to assess LAT*

Database of activation maps

The accuracy of the LAT methods in algorithmic (unedited) activation mapping was evaluated in another 12 AT and 10 VT patients. These patients were selected based upon the presence of high density maps (>100 sites) and an unambiguous activation pattern confirmed by ablation-induced termination at the target set forward by the activation map.

Initially, activation maps were generated by Carto (peak detection) after which they were further edited by manual re-annotation of LAT based upon the interpretation of double potentials, timing of neighboring electrograms, and putative activation sequences (MD, RT). These edited comprehensive activation maps were considered the gold-standard. For each comprehensive map, five activation maps were created based upon each LAT method. These unedited algorithmic LAT maps were created in Carto by manually resetting each marker to the respective LAT value generated offline in Matlab. In each unedited algorithmic map, we (MEH, RH; blinded to the comprehensive maps) determined the activation pattern and possible ablation target. Post-hoc, each algorithmic map was scored based upon its accuracy compared to the comprehensive map (3=correct activation pattern and ablation target for focal tachycardia or correct activation pattern for macro-reentry, 2=correct recognition of the tachycardia type but incomplete activation pattern, 1=incorrect activation pattern).

Prospective validation of U-LAT$_{\text{Slope-hybrid}}$

U-LAT$_{\text{Slope-hybrid}}$ was prospectively validated in another 8 AT patients. Via a special add-on module, U-LAT$_{\text{Slope-hybrid}}$ values calculated in Matlab could be imported in

Carto3 system, resulting in a color-coded activation map. This U-LAT$_{\text{Slope-hybrid}}$ map was used to define the ablation target.

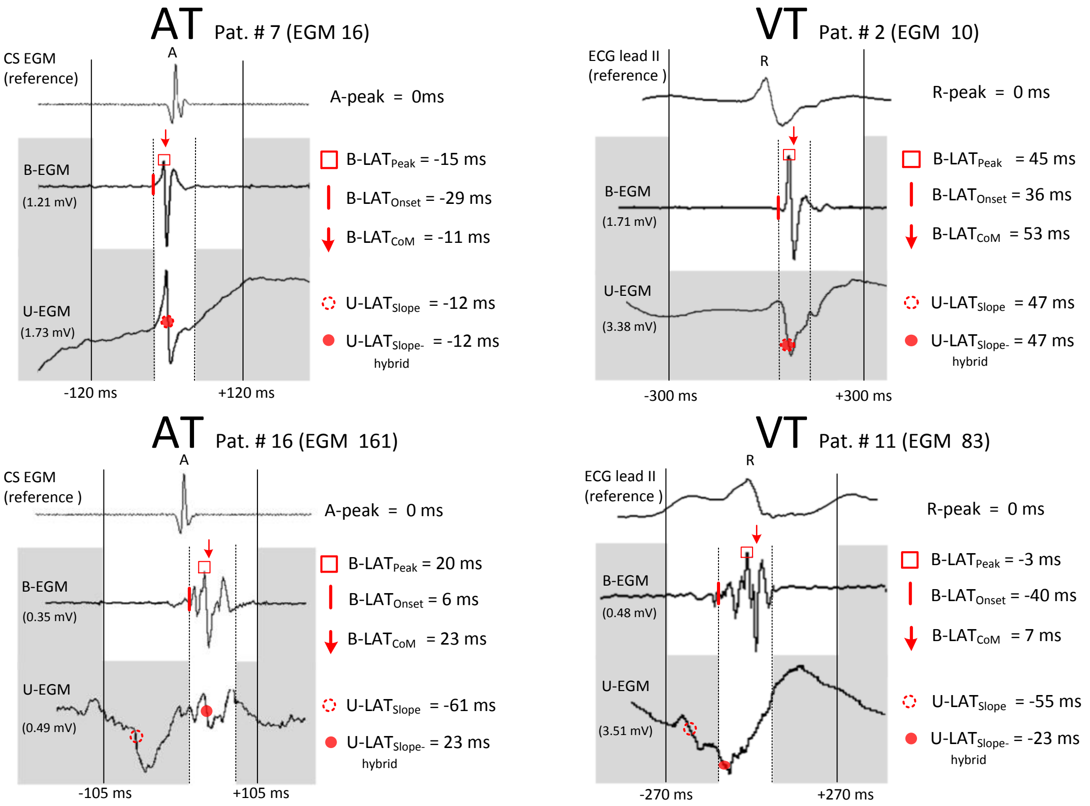

Figure 2-2: *Performance of the conventional and novel methods in detecting LAT in high and low quality atrial and ventricular EGMs*

Statistics

Data are presented as mean±SD unless stated otherwise. Significance in mean difference in peak-to-peak voltage between AT and VT was tested in SPSS v.15 using linear mixed-effect model. To account for multiple recordings within the same patient, prevalence of HQ and LQ in AT and VT, mean peak-to-peak voltage in HQ and LQ, prevalence of fragmented and double potentials in HQ and LQ were analyzed per patient. Significance in mean difference was tested using Wilcoxon-Mann-Whitney test. The performance of the LAT methods in detecting LAT was evaluated paired-wise. Linear regression with Cook's distance was used to identify outliers (a distance > 4/n was considered an outlier). For each comparison, histogram analysis (P5, P50, P95) of the differences in LAT values was performed. The variation in differences (P95-P5) in LQ EGMs was descriptively compared to HQ EGMs.

2.3 Results

Quality of the B-EGMs

Peak-to-peak bipolar voltage in AT was lower than in VT (0.57±0.79 vs. 1.93±2.27mV, linear mixed-effect model $p<0.001$). Further results of the analysis (per patient) of prevalence of HQ and LQ in AT and VT, and peak-to-peak-voltage, double potentials, and fragmented potentials in HQ and LQ (for both AT and VT) are given in Table 2.

Performance of LAT methods in detecting LAT in high and low quality EGMs in AT

Representative examples are given in Figure 2 (left panels). In the upper panel, a HQ B-EGM with its corresponding U-EGM is shown. Visually, annotation of B-$\text{LAT}_{\text{Onset}}$ and U-$\text{LAT}_{\text{Slope-hybrid}}$ are accurate. B-LAT_{CoM} coincided with U-$\text{LAT}_{\text{Slope-hybrid}}$. In the LQ EGM (lower panel, 0.35mV, multiple peaks), B-$\text{LAT}_{\text{Onset}}$ again accurately detects the unique moment of onset. The U-EGM is disturbed by far-field potentials and multiple slopes making conventional detection of maximal -dV/dt inaccurate (-61ms). Demarcation of the bipolar window of interest enables reliable detection of the maximal -dV/dt (U-LAT$_{\text{Slope-hybrid}}$). Again, B-LAT$_{\text{CoM}}$ and U-LAT$_{\text{Slope-hybrid}}$ coincided, both 17ms later than B-LAT$_{\text{Onset}}$.

Table 2.2: *Characteristics of high and low quality electrograms (HQ and LQ) in AT and VT patients*

	Prevalence of		**Peak-to-peak bipolar voltage in**		**Prevalence of fragmented potentials in**		**Prevalence of double potentials in**	
	HQ EGMs (%)	**LQ EGMs** (%)	**HQ EGMs (mV)**	**LQ EGMs (mV)**	**HQ EGMs (%)**	**LQ EGMs (%)**	**HQ EGMs (%)**	**LQ EGMs (%)**
AT (n=31 patients)	71±22	29±2 *	0.67±0.49	0.17±0.1 *	0.43±1.11	3.99±5.28 *	1.41±1.69	7.51±10.70
	63	15	0.28	0.07	0	0	0	0
	75	25	0.50	0.13	0	0	0	2.78
	85	37	1.04	0.25	0	6.45	3.03	10.53
VT (n=23 patients)	81±15	19±1 *†	2.23±0.67 †	0.33±0.3 *†	2.46±3.54 †	4.66±7.08	0.54±1.42	2.03±6.16 †
	74	9	1.96	0.21	0	0	0	0
	83	17	2.18	0.27	0.60	0	0	0
	91	26	2.55	0.31	3.48	8.74	0	0

Data is given as mean ± standard deviation; median and interquartile range (25th and 75th).

**Difference between HQ and LQ (Wilcoxon-Mann-Whitney test)*

†Difference between AT and VT (Wilcoxon-Mann-Whitney test)

In Figure 3 we plotted the histograms of the differences between the LAT methods in all HQ (blue bins) and LQ EGMs (green bins). The median difference between B-LAT$_{\text{Peak}}$ and B-LAT$_{\text{Onset}}$ (left upper histogram) is 20ms with a variation in differences of 36ms in HQ EGMs, and 16ms with a variation of 101ms in LQ EGMs. The median differences (20, 16ms) are due to the nature of the methods (onset preceding peak). The variation is expected to be due to ambiguity of peak detection. This is supported by the larger variation in LQ EGMs (101 vs. 36ms).

When comparing B-LAT$_{\text{Peak}}$ to B-LAT$_{\text{CoM}}$, the histogram shows a median difference of -1ms with 26ms variation in HQ EGMs, and a median difference of -2ms with 66ms variation in LQ EGMs. The median differences suggest that CoM coincides with the peak (i.e. the energy of the signal is symmetrically distributed around the peak). The increased variation in LQ EGMs is due to ambiguity of peak detection (66 vs. 26ms).

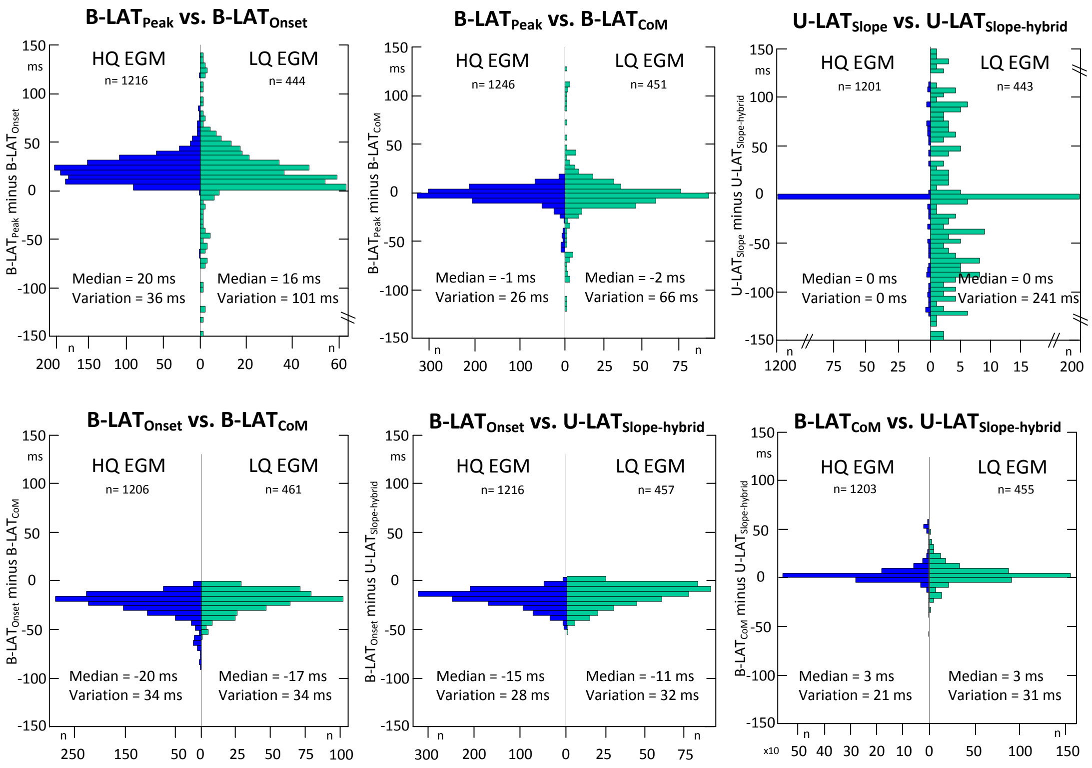

Figure 2-3: *Histogram plots of the difference between LAT methods in HQ (blue bins) and LQ (green bins) EGMs in AT.*

Comparing U-LAT$_{Slope}$ to U-LAT$_{Slope-hybrid}$ (right upper panel) shows that they either detect an identical time instant (median 0ms), or a completely different time instant (resulting from erroneous slope detection by U-LAT$_{Slope}$). In HQ EGMs, the percentage of U-LAT$_{Slope}$ values differing from U-LAT$_{Slope-hybrid}$ was 4%, compared to 33% in LQ EGMs.

The median difference between B-LAT$_{Onset}$ and B-LAT$_{CoM}$ was -20ms with a 34ms variation in HQ EGMs and -17ms with 34ms variation in LQ EGMs (left lower histogram). The low and equal variation in differences in HQ and LQ EGMs (34ms, 34ms) is explained by the low ambiguity of both methods.

The same is true when comparing B-LAT$_{Onset}$ and U-LAT$_{Slope\text{-}hybrid}$ (median difference of -15ms with a 28ms variation in HQ EGMs vs. median difference of -11ms with a 32ms variation in LQ EGMs, middle lower panel).

Interestingly, the median difference between B-LAT$_{CoM}$ and U-LAT$_{Slope\text{-}hybrid}$ (right lower panel) is only 3ms with a 21ms variation in HQ EGMs and 3ms with a 31ms variation in LQ EGMs. This small difference indicates that LAT as determined by CoM and slope-hybrid coincides.

Performance of LAT methods in detecting LAT in high and low quality EGMs in VT

Representative examples are given in Figure 2. In the right upper panel, the B-LAT$_{Onset}$ accurately detects the onset of the HQ B-EGM (1.71mV). The morphology of the U-EGM allows straightforward detection of maximal -dV/dt. The U-LAT$_{Slope\text{-}hybrid}$ slightly differs from the B-LAT$_{CoM}$ (47 vs. 53ms). In the lower panel, a fragmented, long-duration B-EGM is plotted together with its U-EGM revealing multiple slopes. B-LAT$_{Onset}$ precedes B-LAT$_{CoM}$ by 47ms. Now, detection of the maximal –dV/dt of the U-EGM was only accurate after blanking of the far-field potentials (U-LAT$_{Slope\text{-}hybrid}$, -23ms). Overall, the LAT methods performed similar in VT compared to AT (Figure 4).

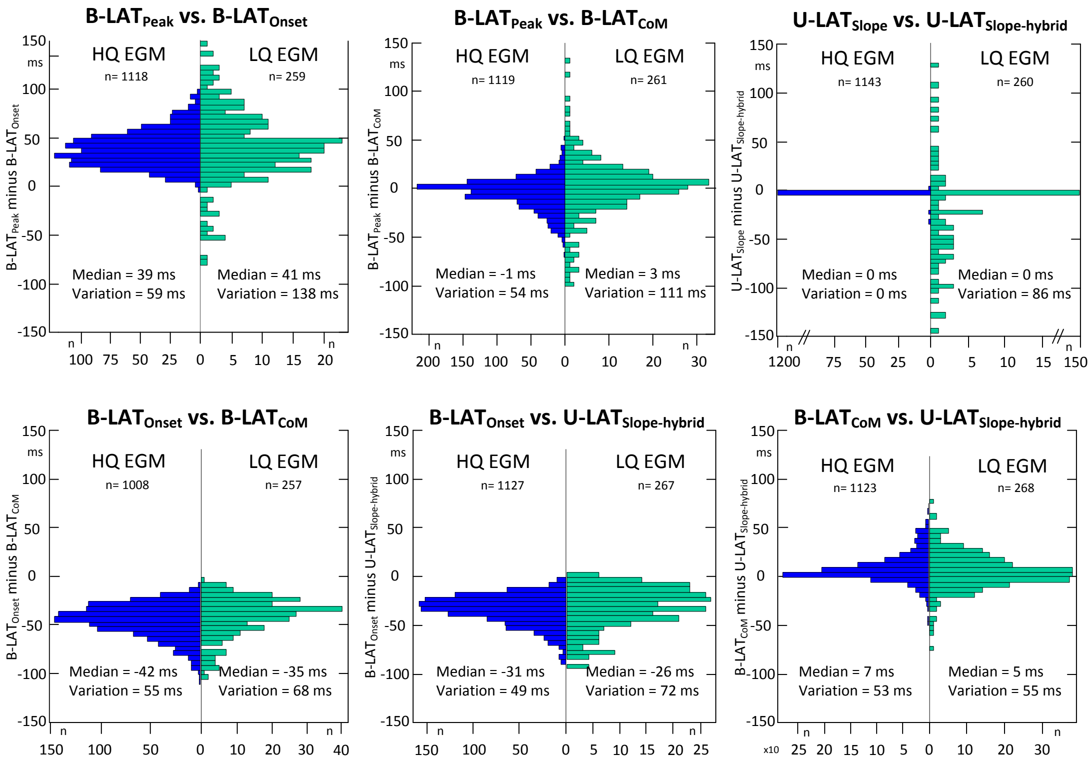

Figure 2-4: *Histogram plots of the difference between LAT methods in HQ (blue bins) and LQ (green bins) EGMs in VT.*

Accuracy of the LAT methods in algorithmic activation mapping of AT

In Figure 5 a representative example is shown (patient ID: AT-8, 17% LQ EGMs). The comprehensive map (upper panel) displays a rotor-like spiral activation pattern located on the posterolateral wall of the right atrium. A single RF application at the epicenter (white circle) resulted in immediate AT termination. Corresponding B-EGMs and U-EGMs from five different sites are shown. By visual tracking of the B-EGMs (but not the U-EGMs), activation can be traced in a counter clockwise rotation from site 1 to site 5.

On each EGM, the fiducial markers determined by the respective LAT methods are plotted (yellow). In the B-EGMs from sites 1 and 4, all LAT methods detected comparable activation moments. In contrast, in the EGMs from sites 2, 3 and 5, the conventional U-LAT$_{\text{Slope}}$ method erroneously detected ventricular far-field. The correct negative slope was only detected by the U-LAT$_{\text{Slope-hybrid}}$ method. Interestingly at site 2 (LQ), the U-EGM consists of two components and U-LAT$_{\text{Slope-hybrid}}$ annotated the second component corresponding to the peak and CoM on the B-EGM.

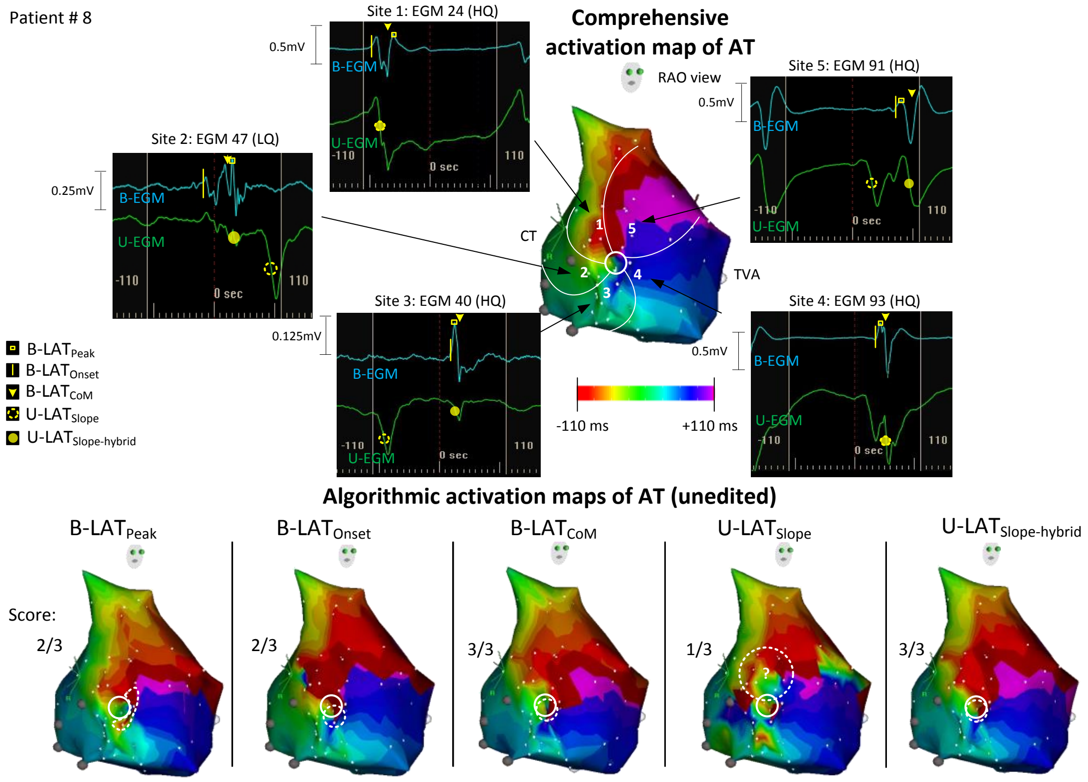

__Figure 2-5:__ Accuracy of the LAT methods in algorithmic activation mapping in AT. The AT cycle length was 230ms.

The unedited algorithmic LAT maps are shown in the lower panels. B-LAT$_{\text{Peak}}$, B-LAT$_{\text{Onset}}$, B-LAT$_{\text{CoM}}$, and U-LAT$_{\text{Slope-hybrid}}$ identified the correct activation pattern or the appropriate ablation target (respective scores of 2, 2, 3, and 3). The U-LAT$_{\text{Slope}}$ method did not indicate the correct ablation site (score of 1).

In Figure 6 another example of an AT is shown (patient ID: AT-13, 41% LQ EGMs). The edited map displays macroreentrant activation around the mitral annulus. Creating a line of block from the annulus to the left inferior pulmonary vein resulted in termination of the AT. By visual tracking of the B-EGMs (but not the U-EGMs), the spread of activation can be traced in a clockwise rotation from site 1 to site 5.

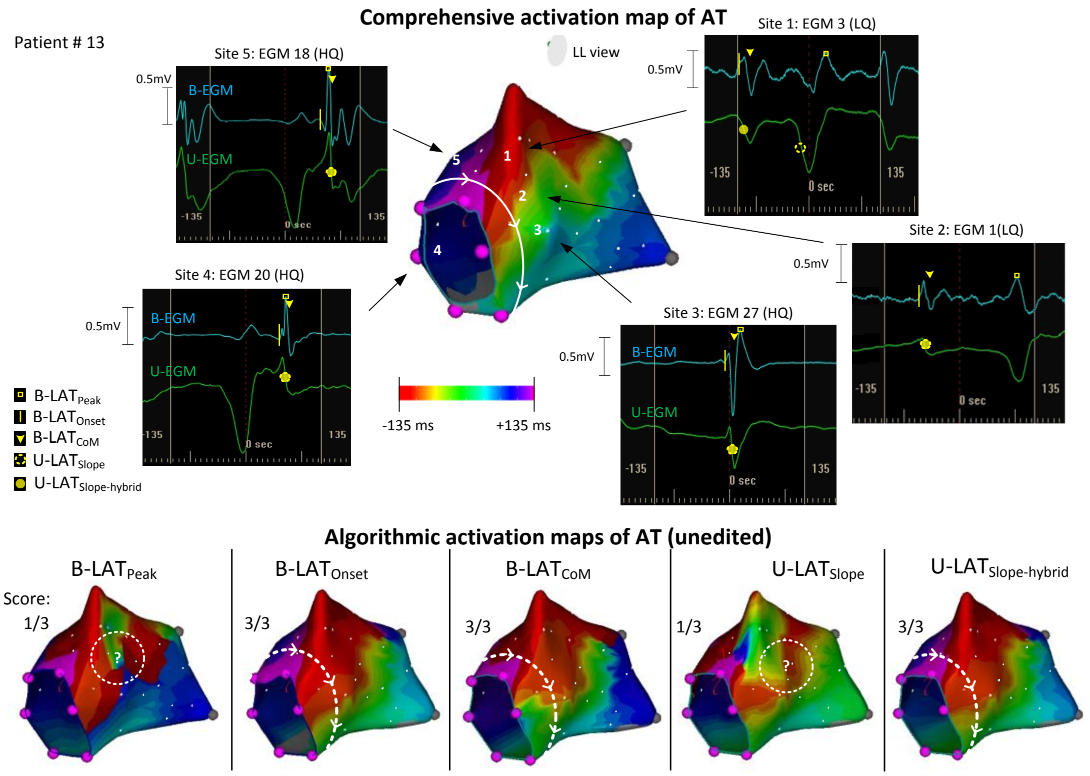

Figure 2-6: *Accuracy of the LAT methods in algorithmic activation mapping of AT. The AT cycle length was 280ms.*

In the HQ B-EGMs from sites 3, 4, and 5, all LAT methods detected comparable activation moments. In contrast, in the LQ EGMs from sites 1 and 2, the B-LAT$_{\text{Peak}}$ method erroneously detected the second ventricular far-field potential. In the U-EGM (site 1), conventional U-LAT$_{\text{Slope}}$ erroneously detected ventricular far-field. The unedited algorithmic LAT maps are shown below. The three novel LAT methods identified the correct activation pattern and appropriate ablation target (white line, score =3). The conventional LAT methods B-$\mathrm{LAT}_{\mathrm{Peak}}$ and U-$\mathrm{LAT}_{\mathrm{Slope}}$, were not able to indicate the correct ablation pattern (score =1).

Accuracy of the LAT methods in algorithmic activation mapping of VT

In Figure7, a representative example of ischemic VT is shown (patient ID: VT-23, 15% LQ EGMs). The comprehensive map displays a focal VT in the left ventricle. A single RF application at the earliest site of activation (white circle) resulted in termination of the VT. Visually, the centrifugal spread of activation can be traced (from site 1 to 2 to 3; and from site 1 to 2’ to 3’).

At the area of earliest activation (site 1), the B-EGM was fractionated and the U-EGM revealed two separate components. Whereas U-$\mathrm{LAT}_{\mathrm{Slope}}$ identified the second component (of unknown origin) as the moment of activation (green zone in the activation map), U-$\mathrm{LAT}_{\mathrm{Slope\text{-}hybrid}}$ correctly assigned the first component as the LAT. In the B-EGM from site 2 and 2’, the difference between B-$\mathrm{LAT}_{\mathrm{Onset}}$ and the LAT determined by the other methods was considerable due to the long duration of the B-EGM. In the EGM from site 3 and 3’, all LAT methods detected comparable activation moments. The unedited algorithmic LAT maps are shown in the lower panel. All LAT methods showed the correct activation pattern (focal pattern). B-$\mathrm{LAT}_{\mathrm{Onset}}$ and U-$\mathrm{LAT}_{\mathrm{Slope}}$ however, pointed to a large and non-precise ablation target (score =2). U-$\mathrm{LAT}_{\mathrm{Slope\text{-}hybrid}}$ method however, pointed to the most appropriate ablation target (score =3).

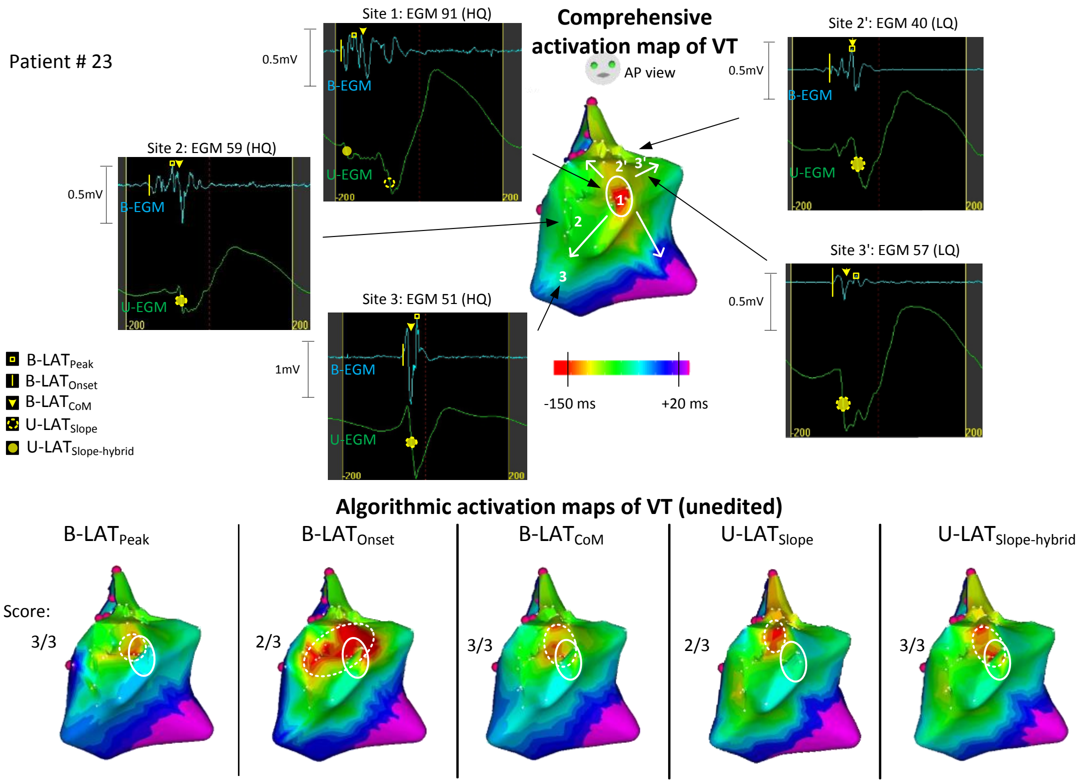

Figure 2-7: *Accuracy of the LAT methods in algorithmic activation mapping in VT. The ventricular cycle length was 410ms. See text for explanation.*

Overall accuracy of the LAT methods in algorithmic mapping of AT and VT

The accuracy of the LAT methods in AT and VT (n=22) is summarized in Table 3. Maps were ranked according to the % of LQ EGMs (up to 60% in AT and 34% in VT). All LAT methods showed high accuracy in identifying the correct activation pattern and defining the optimal ablation target (mean score ≥2.55), except for U-LAT$_{\text{Slope}}$ in which accuracy was significantly lower than the other methods (score 1.91±0.68, p<0.001).

Table 2.3: Accuracy of LAT methods in algorithmic activation mapping of AT and VT

Patient ID	Type of tachycardia	Chamber	Localization	Tachycardia cycle length (ms)	% of LQ EGMs per map	Accuracy score of unedited maps (score 1 to 3)				
						B-LAT Peak	B-LAT Onset	B-LAT CoM	U-LAT Slope	U-LAT Slope-Hybrid
VT-13	Focal	LV	Inferoapical free wall	400	4%	3	3	3	3	3
AT-6	Focal	LA	Septum	310	6%	2	3	3	2	3
VT-14	Focal	RV	Inferoapical septum	310	8%	3	2	2	3	3
VT-10	Focal	LV	Anteroapical septum	500	9%	2	2	2	2	2
VT-8	Focal	LV	Inferoapical free wall	456	10%	3	3	3	2	3
AT-14	Rotor	LA	Base of LAA	420	15%	3	3	3	2	3
VT-23	Focal	LV	Anterobasal free wall	410	15%	3	2	3	2	3
AT-18	Focal	LA	LIPV	270	16%	3	2	2	2	2
AT-8	Rotor	RA	Posterolateral	230	17%	2	2	3	1	3
VT-2	Macro-reentry	LV	Anterior wall	670	19%	3	3	3	3	3
VT-11	Focal	LV	Anterobasal and midseptum	350	19%	3	3	3	1	2
AT-2	Macro-reentry	RA	Peri-tricuspid	275	24%	3	3	3	2	3
AT-1	Macro-reentry	LA	Peri-mitral	318	25%	3	3	3	2	3
AT-9	Macro-reentry	RA	Peri-tricuspid	275	26%	3	3	3	2	3
VT-12	Macro-reentry	LV	Apex	450	26%	3	3	1	2	3
AT-7	Double loop macro-reentry	LA	Peri-mitral & roof dependent	240	32%	3	3	3	1	3
VT-1	Macro-reentry	LV	Apex	540	32%	3	1	3	2	3
VT-6	Focal	LV	Inferoapical free wall	460	34%	2	3	2	3	3
AT-30	Focal	LA	Septum	310	37%	1	2	2	2	2
AT-4	Macro-reentry	LA	Peri-mitral	460	41%	2	2	2	1	2
AT-13	Macro-reentry	LA	Peri-mitral	280	41%	1	3	3	1	3
AT-17	Macro-reentry	LA	Roof dependent	235	60%	2	2	2	1	2
						2.55 ± 0.67	**2.55 ± 0.60**	**2.59 ± 0.59**	**1.91* ± 0.68**	**2.73 ± 0.46**

** Statistically significant from all the other methods (Student's t-test p<0.05). LA: left atrium, RA: right atrium, LV: left ventricle, RV: right ventricle, LAA: left atrial appendage, LIPV: left inferior pulmonary vein.*

All LAT methods showed a trend towards decreased accuracy with increasing percentage of LQ EGMs (LQ≤25% vs. LQ>25%, 2.54±0.58 vs. 2.22±0.76, p=0.035), except for $\text{LAT}_{\text{Slope-hybrid}}$ (LQ≤25% vs. LQ>25%, 2.75±0.45 vs. 2.70±0.39, p=NS), the only method that did not fail in any of the maps (no score of 1).

Overall (Fig. 8), algorithmic mapping of AT and VT showed that $\text{U-LAT}_{\text{Slope-hybrid}}$ performed the best by accurately mapping 16 out of 22 maps compared to $\text{B-LAT}_{\text{CoM}}$ (n=14), $\text{B-LAT}_{\text{Peak}}$ (n=14), $\text{B-LAT}_{\text{Onset}}$ (n=13), and $\text{U-LAT}_{\text{Slope}}$ (n=4).

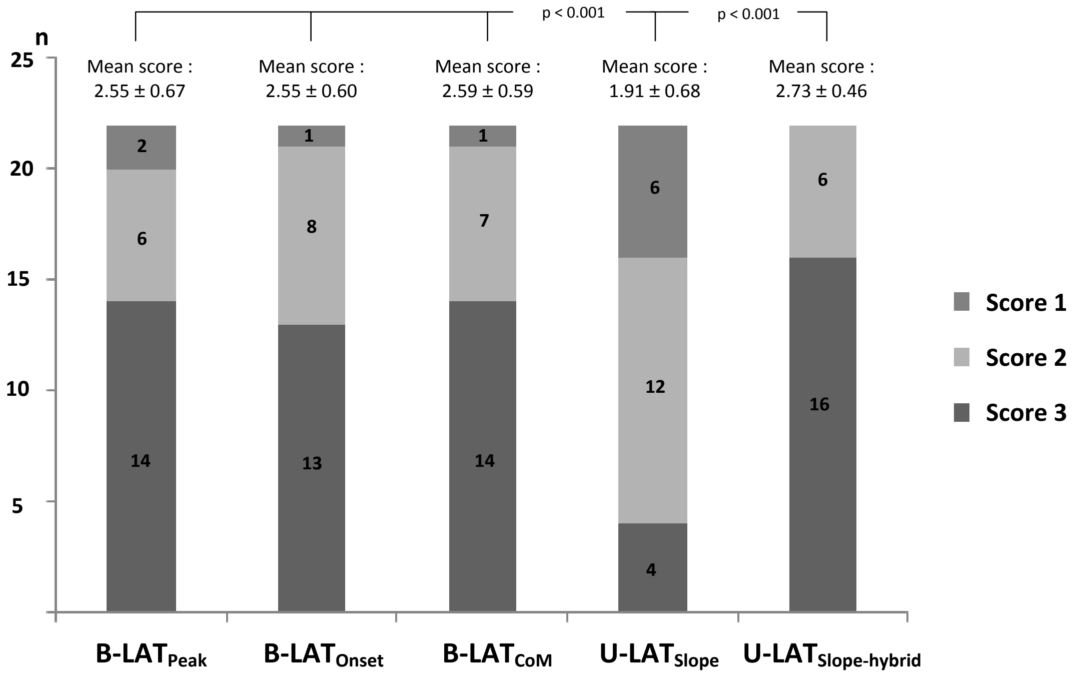

Figure 2-8: *Overall accuracy of the LAT methods in unedited algorithmic mapping of AT and VT. Accuracy scores explained in text.*

Prospective validation of $\text{U-LAT}_{\text{Slope-hybrid}}$

Mapping of AT using $\text{U-LAT}_{\text{Slope-hybrid}}$ revealed 4 macro-reentrant, 3 focal, and 1 spiral wave tachycardia. Ablation guided by $\text{U-LAT}_{\text{Slope-hybrid}}$ resulted in 8/8 (100%) termination of AT.

2.4 Discussion

Main Findings

1) We introduced three algorithmic methods to assess LAT in bipolar and unipolar electrograms. 2) In B-EGMs, compared to peak detection, B-LAT$_{\text{Onset}}$ and B-LAT$_{\text{CoM}}$ detect a more reliable fiducial marker in low quality electrograms. 3) In U-EGMs, the U-LAT$_{\text{Slope-hybrid}}$ method accurately detects the true moment of activation. 4) In algorithmic mapping of AT and VT, U-LAT$_{\text{Slope-hybrid}}$ has incremental benefit over the other methods. These findings were obtained in clinically representative and challenging tachycardias, as many maps included high % of LQ EGMs (up to 60% in AT and 34% in VT) typically recorded in scar regions (0.15±0.25mV in AT and 0.25±0.15mV in VT).

Conventional activation mapping

Conventionally, the B-EGM is used to annotate LAT because B-EGMs - due to subtraction of unipolar electrograms - are devoid of noise and far-field potentials. B-EGMs however are influenced by wavefront direction, bipole orientation, electrode size, and inter-electrode spacing.[9] In addition, in complex myocardial activation, multiple peaks in a B-EGM result in more ambiguity to identify the peak corresponding to the true moment of activation.[8] To overcome these limitations, electrophysiologists often manually re-annotate the LAT. Comprehensive mapping however is time-consuming and requires specific EP skills particularly in complex activation patterns. Moreover, presumption of the activation pattern can lead to misconception.

The onset of the B-EGM (B-$\text{LAT}_{\text{Onset}}$)

Prior clinical studies used the onset of the B-EGM to assess LAT and guide ablation.[7,8,11,12] However, no mapping was performed and the onset was annotated manually. We detected the onset of B-EGM by a robust automated algorithm. Compared to the maximal -dV/dt in U-EGMs, B-$\text{LAT}_{\text{Onset}}$ was 15ms and 31ms earlier in AT and VT. Interestingly, B-$\text{LAT}_{\text{Onset}}$ performed equally in HQ and LQ EGMs. Furthermore, B-$\text{LAT}_{\text{Onset}}$ showed good and comparable (to B-LAT_{peak}) accuracy in activation mapping (appropriate mapping in 13 out of 22).

B-$\text{LAT}_{\text{Onset}}$ has the advantage of detecting a single, unambiguous, and unique moment in the B-EGM (also in LQ electrograms). B-$\text{LAT}_{\text{Onset}}$ however, is sensitive to near-field activation.[7] As the beginning of B-EGM reflects first activation recorded by either the tip or the ring of the bipole, it might pick up distant wavefronts approaching and travelling away from the recording electrodes. In focal tachycardia, this may result in less precise annotation of the area of earliest activation (Figure 6).

The center of mass of the B-EGM (B-LAT_{CoM})

The CoM, a morphology rather than single point based approach, is a computational parameter representing the midst energy moment of the wave underpassing the electrode (i.e. same wave propagates towards and away from the electrode).[13,14,15,16] The observation that B-LAT_{CoM} almost coincided with the maximal unipolar –dV/dt, supports its physiological sense and clinical validity.

Prior studies showed superiority of CoM over conventional methods especially in complex B-EGMs.[13,14,15] No study however, tested the performance of CoM in algorithmic mapping of clinical tachycardias. We introduced a robust automated algorithm to determine CoM and showed that B-LAT$_{\text{CoM}}$ provides a marker that is less ambiguous in LQ electrograms. Moreover, B-LAT$_{\text{CoM}}$ showed a good accuracy in activation mapping (appropriate mapping in 14 out of 22 unedited algorithmic maps).

The maximal negative unipolar slope within a pre-defined 'bipolar' window (U-LAT$_{\text{Slope-hybrid}}$)

Spach et al.[1,2] showed that the maximal -dV/dt in the U-EGM coincides with the upstroke of the action potential. Moreover, U-EGM morphology allows interpretation of wavefront direction. The presence of far-field potentials however makes algorithmic detection virtually impossible.[3] Inferior outcome of the U-LAT$_{\text{Slope}}$ algorithm (both in EGM detection and mapping accuracy) confirms this limitation.

Although complex filtering, statistical approaches, frequency analysis, electrode size and inter-electrode spacing could optimize U-EGMs,[17,18,19,20,21] their use remains limited in the clinical setting. We optimized the U-EGMs by searching for the maximal unipolar –dV/dt only within the window demarcated by the beginning and the end of B-EGM complex. This way of blanking effectively prevented detection of erroneous slopes not related to underpassing of the wavefront. Our data suggested incremental benefit of the U-LAT$_{\text{Slope-hybrid}}$ in LQ electrograms. This benefit was further underscored by the highest accuracy among all LAT methods in mapping AT and VT (appropriate mapping in 16 out of 22). These findings suggest that our method allows U-EGMs not only to compete but also to outperform B-EGMs in detecting LAT in clinical EP settings.

Clinical implications

Patients more and more undergo ablation for AT/VT with LQ electrograms and challenging activation patterns (fibrosis, prior complex ablation strategies, …). We showed that the novel LAT methods have incremental benefit in complex activation maps with LQ EGMs (all <0.5mV). As such, their implementation in existing or new mapping technologies could improve both comprehensive (less manual re-annotation needed) and automated mapping of these tachycardias in the future. Prospective validation of $LAT_{\text{Slope-hybrid}}$ revealed high performance in guiding ablation. Further validation in a larger multi-center study is needed and will be possible once these algorithms are available online (ongoing project).

The novel LAT methods combined with multi-electrode catheters could even outperform mapping by experienced electrophysiologists, eventually making ablation possible in “unmappable” AT and VT. These methods could be even used to map atrial and ventricular fibrillation. Especially in atrial fibrillation characterized by rotors, longitudinal waves, epicardial breakthrough, etc…, the novel U-EGM method could be potentially advantageous. Finally, the novel U-EGM method could improve substrate-guided VT ablation, since unipolar endocardial electrograms can unmask an epicardial substrate.[22]

Limitations

There is no true gold standard for activation mapping in clinical practice, human assignment of activation times is not necessarily correct, and due to the size of the ablation area, some focal tachycardias could terminate even if the mapping target was not accurate. These limitations however, cannot be overcome with the current mapping technology.

We tested the accuracy of the novel methods in a limited dataset of tachycardias. However, the maps were representative for a larger scale of clinically encountered AT and VT.

Care should be taken when extrapolating our findings to scar-related ischemic VT, as our database contained 70% focal VT.

In theory, all methods could perform better if beat-selection was performed by the operator. This speaks however against fully automated mapping.

2.5 References

1. Spach MS, Miller WT, III, Miller-Jones E, Warren RB, Barr RC. Extracellular potentials related to intracellular action potentials during impulse conduction in anisotropic canine cardiac muscle. CircRes 1979;45:188-204.

2. Spach MS, Dolber PC. Relating extracellular potentials and their derivatives to anisotropic propagation at a microscopic level in human cardiac muscle. Evidence for electrical uncoupling of side-to-side fiber connections with increasing age. CircRes 1986;58:356-71.

3. Stevenson WG, Soejima K. Recording techniques for clinical electrophysiology. J Cardiovasc Electrophysiol. 2005;16:1017-22.

4. Biermann M, Sheanasa M, Borggrefe M, et al. The interpretation of cardiac electrograms. In: Sheanasa M, Borggrefe M, Breithardt G, eds. Cardiac Mapping. New York, NY: Futura Publishing, 1993, p.11–34.

5. De Bakker JMT, Hauer RNW, Simmers TA: Activation mapping: Unipolar versus bipolar recording. In: Zipes DP, Jalife J, eds: Cardiac Electrophysiology. From Cell to Bedside. Second Edition. Philadelphia, PA: W.B. Saunders, 1995, p.1068.

6. Shah D, Haissaguerre M, Jais P, Clementy J. High-resolution mapping of tachycardia originating from the superior vena cava: evidence of electrical heterogeneity, slow conduction, and possible circus movement reentry. Journal of Cardiovascular Electrophysiology. 2002;13:388–392.

7. Paul T, Moak JP, Morris C, Garson A Jr. Epicardial mapping: how to measure local activation? Pacing Clin Electrophysiol. 1990;13:285-92.

8. Liuba I, Walfridsson H. Activation mapping of focal atrial tachycardia: the impact of the method for estimating activation time. J Interv Card Electrophysiol. 2009;26:169-80.

9. Ndrepepa G, Caref EB, Yin H, el-Sherif N, Restivo M. Activation time determination by high-resolution unipolar and bipolar extracellular electrograms in the canine heart. J Cardiovasc Electrophysiol. 1995;6:174-88.

10. El Haddad M, Houben M, Stroobandt R, Van Heuverswyn F, Tavernier R, Duytschaever M. Algorithmic detection of the beginning and end of bipolar electrograms: Implications for novel methods to assess local activation time during atrial tachycardia. Biomed Signal Process Control. 2013;8:981-991.

11. Kalman JM, Olgin JE, Karch MR, Hamdan M, Lee RJ, Lesh MD. "Cristal tachycardias": origin of right atrial tachycardias from the crista terminalis identified by intracardiac echocardiography. J Am Coll Cardiol. 1998;31:451-9.

12. Weiss C, Willems S, Rueppel R, Hoffmann M, Meinertz T. Electroanatomical Mapping (CARTO) of ectopic atrial tachycardia: impact of bipolar and unipolar local electrogram annotation for localization of the focal origin. J Interv Card Electrophysiol. 2001;5:101-7.

13. Holm M, Johansson R, Olsson SB, Brandt J, Lührs C. A new method for analysis of atrial activation during chronic atrial fibrillation in man. IEEE Trans Biomed Eng. 1996:43:198-210.

14. Faes L, Nollo G, Antolini R, Gaita F, Ravelli F. A method for quantifying atrial fibrillation organization based on wave-morphology similarity. IEEE Trans Biomed Eng. 2002:49:1504-13.

15. Sandirini L, Faes L, Ravelli F, Antolini R, Nollo G. Morphology-based measurements of activation time in human atrial fibrillation. Computers in Cardiology 2002:29:593-96.

16. Pieper CF, Blue R, Pacifico A. Simultaneously collected monopolar and discrete bipolar electrograms: comparison of activation time detection algorithms. Pacing Clin Electrophysiol. 1993:16:426-33.

17. Dubé B, Vinet A, Xiong F, Yin Y, LeBlanc AR, Pagé P. Automatic detection and classification of human epicardial atrial unipolar electrograms. Physiol Meas. 2009;30:1303-25.

18. Anderson KP, Walker R, Ershler PR, Fuller M, Dustman T, Menlove R, Karwandee SV, Lux RL. Determination of local myocardial electrical activation for activation sequence mapping: A statistical approach. Circ Res 1991; 69:898–917.

19. Cabo C, Wharton JM, Wolf PD, Ideker RE, Smith WM. Activation in unipolar cardiac electrograms: A frequency analysis. IEEE Trans Biomed Eng 1990; 37:500–508.

20. Caref EB, Ndrepepa G, Turitto G, Restivo M, El-Sherif N. Improved activation time assignment of unipolar electrograms from ischemic canine epicardium. Pacing Clin Electrophysiol. 2011;34:1105-15.

21. Blanchard SM, Damiano RJ, Asano T, Smith WM, Ideker RE, Lowe JE. The effects of distant cardiac electrical events on local activation in unipolar epicardial electrograms. IEEE Trans Biomed Eng 1987; 34:539–546.

22. Hutchinson MD, Gerstenfeld EP, Desjardins B, Bala R, Riley MP, Garcia FC, Dixit S, Lin D, Tzou WS, Cooper JM, Verdino RJ, Callans DJ, Marchlinski FE. Endocardial unipolar voltage mapping to detect epicardial ventricular tachycardia substrate in patients with nonischemic left ventricular cardiomyopathy. Circ Arrhythm Electrophysiol. 2011;4:49-5.

CHAPTER 3

A stable reentrant circuit with spiral wave activation driving atrial tachycardia

Milad El Haddad, MS; Richard Houben, PhD; Rene Tavernier, MD, PhD; Mattias Duytschaever, MD, PhD

This challenging case was published in the journal Heart Rhythm, volume 11, issue 4, pages 716-718 in April 2014

3.1 Introduction

According to the joint expert committee from the Working Group of the European Society of Cardiology and the Heart Rhythm Society,[1] atrial tachycardia (AT) is categorized as *focal* if the activation starts rhythmically at a small area and spreads centrifugally, or *macro-reentrant* if characterized by reentrant activation around a “large” central obstacle. We mapped and ablated a stationary reentrant circuit with *spiral* activation driving AT in the left atrium (LA). Because of its regular cycle length, this case offered the unique opportunity to study in detail the characteristics of intracardiac activation and electrograms during spiral wave activation.

3.2 Activation mapping and ablation of the reentrant circuit

A 79-year old female patient with mild mitral valve regurgitation was referred for ablation of symptomatic tachycardia (regular AT cycle length of 290ms). The surface ECG revealed upright P waves with iso-electric segments in leads II, III, aVF, and V1 (Figure 1, upper tracing). An irrigated-tip ablation catheter with a distal 3.5mm tip and three 1mm ring electrodes spaced by 2-5-2mm (Navistar® Thermocool, Biosense-Webster, Diamond Bar, CA, USA) was used for detailed endocardial, point-by-point (230 points) mapping of the LA (CARTO® system, Biosense-Webster, Diamond Bar, CA, USA). The bipole of a decapolar coronary sinus catheter (CS 5-6) was selected as a reference for activation mapping (A peak = 0 ms) (Figure 1 upper tracing). At each site, a bipolar electrogram (B-EGM, tip minus ring, band-pass filtered 30-240Hz) was recorded for 2.5 seconds at a sampling rate of 1000 Hz.

The LA was characterized by a region of low-voltage at the anterior wall (peak-to-peak voltage <0.5mV, green zone, see voltage map) with even denser scar at the base of the LA appendage near the mitral annulus (<0.05mV, red zone). A representative B-EGM (recorded at site 2) illustrating the true low-voltage nature of the potentials (dotted oval), is plotted below the B-EGM at the CS (recorded at the same amplification).

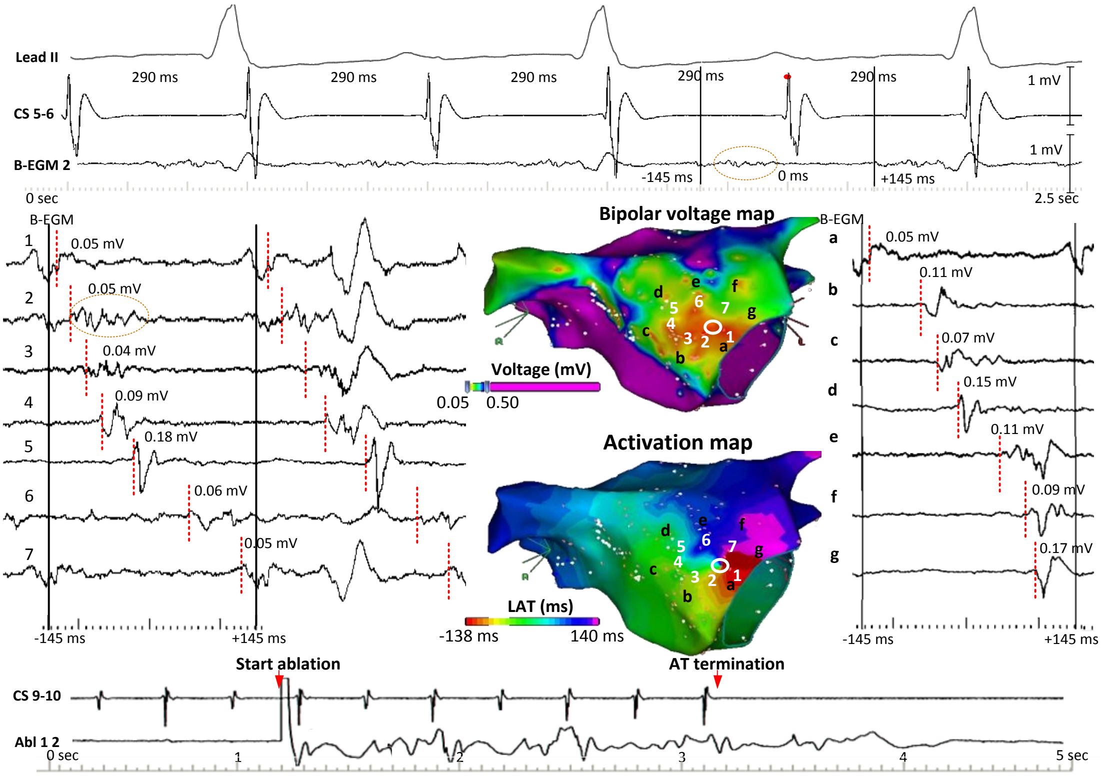

Figure 3-1: *Upper panel: EGM tracings of surface ECGF lead II, coronary sinus (CS), and intra-cardiac bipolar EGM from site 2. Orange circle shows how low the voltage potential in the B-EGM 2. Left and right panels: EGM tracing from sites 1 to 7 and a to b respectively. Red dotted bars indicate the local activation time in each B-EGM. Middle panels: Bipolar voltage map showing a dense scar zone (red) and the activation map showing a spiral wave activation pattern. Low panel: tracings of CS and ablation catheter EGMs showing termination of the tachycardia after only 2 seconds of RF ablation.*

Left atrial activation was analyzed via manual annotation of the onset of all (including the low-voltage) B-EGMs [MD]. Annotation was validated by 2 operators [MEH, RT]. The color-coded activation map showed reentry with clockwise spiral activation within the scar around an apparent epicenter at the base of the left atrial appendage near the mitral annulus (white circle). The isochrones (plotted at 10ms intervals) are curved and allow visual tracking of a wavefront apparently turning 360 degrees around its central core. Interestingly, the core of the vortex was anchored at the area with the lowest voltage. The presence of short double potentials in both unipolar and bipolar EGMs near the mitral annulus, suggests that the wavefront circumnavigating around the mitral annulus collides (rather than merges) with the spiral wave.

Of interest, the activation pattern might be misinterpreted (Figure 2) in case of low density mapping (e.g. 75 sites, falsely generating radial spread) or in case of lack of activation mapping within the dense scar (<0.1mV, falsely generating a macroreentry).

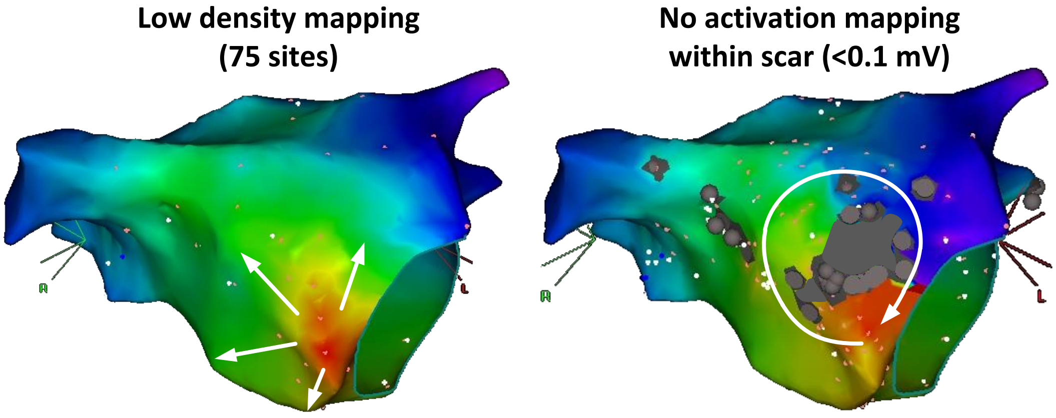

Figure 3-2: *Left panel: focal pattern tachycardia is observed with low density mapping (< 100 site). Right panel: macro-reentrant circuit is observed when no activation mapping within the scar is performed.*

Analysis of the B-EGMs itself revealed the following findings. At the inner part of the spiral wave (site 1 to 7) the B-EGMs are low-voltage (0.04 to 0.18mV) and fractionated (see respective amplified B-EGM tracings at the left). Except for an apparent gap in between sites 5 and 6, the local activation times (dashed vertical lines) are homogeneously distributed over the full cycle length (ranging from -143 to 132ms, i.e. 95% of the cycle length). The similar activation pattern in between two consecutive beats indicates the stability of the circuit. At the outer part of the spiral wave (site a to g), the B-EGMs are low-voltage (0.05 to 0.17 mV) and fractionated as well (see amplified B-EGM tracings on the right). Again EGMs suggest continuous activation covering the full cycle length (except for d to e). We did not observe any clear double potentials in the LA.

To avoid degeneration or termination by pacing, we chose not to perform entrainment maneuvers. Finally, two seconds of RF in the vicinity of the core of the spiral wave terminated the AT (see lower tracing). After continued ablation (for 60-seconds), AT was no longer inducible by burst pacing.

3.3 Discussion

We mapped and ablated a reentrant circuit driving regular AT with a spiral wave activation pattern on color-coded mapping. The reentrant circuit was characterized by stationary spiral wave activation around a central core and the presence of low-voltage, fractionated electrograms. Delivery of RF energy at the vicinity of the core promptly terminated the arrhythmia.

The apparent 360 degree turn of the wavefront around a central core is compatible with spiral wave reentry. Despite high-density mapping (an equivalent of >200 “electrodes”) two mechanisms can still be invoked to explain the observed spiral activation pattern: 1) functional reentry (excitable tissue at the pivoting point) or 2) anatomical reentry (an obstacle at the pivoting point). Experimental data have shown that spiral wave reentry can act as a driver for AT and atrial fibrillation (AF).[2,3]

In functional reentry, spiral wave activation is explained by wavefront curvature dependent changes in conduction velocity surrounding the pivoting point.[4] Although no double potentials were recorded to suggest a functional reentry, the larger time interval between sites 5 and 6 as compared to sites d and e might support this hypothesis. However, ablation at the core is not expected to terminate spiral wave reentry, except if its core is located in the vicinity of a substrate critical for perpetuation.

In the present case, termination by a single focal ablation could be explained by the presence of an isolated narrow channel in the scar area or in between the scar and the mitral annulus.[5] This “isthmus” might span not just anatomical non-conducting barriers but also functionally determined ones (e.g. slow conduction or scar).

The present case has direct implications for mapping and ablation of regular AT. To the best of our knowledge, there is no description of spiral wave activation during regular AT in human. Conventionally, activation patterns during AT are categorized as focal (due to automaticity, triggered activity or micro-reentry) or macro-reentrant.[1] The currently described activation pattern does not fit any of the above categories. Most likely however this pattern is under detected because of misinterpretation of color-coded activation maps (low density maps, no mapping within scar, interpolation, inaccurate annotation, etc…).

The present case may have indirect implications for mapping and ablation in AF as well. Although spiral wave activation was not observed using high density multi-electrode epicardial mapping of AF,[6] the experimental evidence for rotors is growing and new mapping algorithms showing spiral wave activation support the presence of ablatable rotors.[7,8] Our case confirms that spiral wave activation can be observed at or in the vicinity of regions driving tachyarrhythmias. One could speculate that the current reentrant circuit - even if remained fixed - could result in AF at a shorter CL or in the absence of a fixed collision site.[9]

On the other hand, our findings suggest that color-coded mapping (even if based upon more than 200 “electrodes”) introduces ambiguity by interpolation of activation times, and that spiral wave patterns can be due to reentry around a short line of block as well. This ambiguity is likely to increase with increasing complexity of activation (like in AF) and can be overcome only by improving the spatial resolution of mapping (arrays of microelectrodes, smaller electrode size and spacing, unipolar recordings, sampling rate of EGM acquisition, …).

3.4 References

1. Saoudi N, Cosio F, Waldo A, et al. Classification of atrial flutter and regular atrial tachycardia according to electrophysiologic mechanism and anatomic bases: a statement from a joint expert group from the Working Group of Arrhythmias of the European Society of Cardiology and the North American Society of Pacing and Electrophysiology. J Cardiovasc Electrophysiol. 2001;12:852-66.

2. Allessie MA, Bonke FI, Schopman FJ. Circus movement in rabbit atrial muscle as a mechanism of tachycardia. III. The "leading circle" concept: a new model of circus movement in cardiac tissue without the involvement of an anatomical obstacle. Circ Res. 1973;41:9-18.

3. Jalife J. Rotors and spiral waves in atrial fibrillation. J Cardiovasc Electrophysiol. 2003;14:776–780.

4. Danse PW, Garratt CJ, Mast F, Allessie MA. Preferential depression of conduction around a pivot point in rabbit ventricular myocardium by potassium and flecainide. J Cardiovasc Electrophysiol. 2000;11:262-273.

5. Nakagawa H, Shah N, Matsudaira K, et al. Characterization of reentrant circuit in macro-reentrant right atrial tachycardia after surgical repair of congenital heart

disease: isolated channels between scars allow "focal" ablation. Circulation. 2001;103:699-709.

6. Allessie MA, de Groot NM, Houben RP, et al. Electropathological substrate of long-standing persistent atrial fibrillation in patients with structural heart disease: longitudinal dissociation. Circ Arrhythm Electrophysiol. 2010;3:606-615.

7. Narayan SM, Krummen DE, Shivkumar K, Clopton P, Rappel WJ, Miller JM. Treatment of atrial fibrillation by the ablation of localized sources: CONFIRM (Conventional Ablation for Atrial Fibrillation With or Without Focal Impulse and Rotor Modulation) trial. J Am Coll Cardiol. 2012;60:628-36.

8. Haissaguerre M, Hocini M, Shah AJ, et al. Noninvasive panoramic mapping of human atrial fibrillation mechanisms: a feasibility report. J Cardiovasc Electrophysiol. 2013;24:711-7.

9. Berenfeld O, Zaitsev AV, Mironov SF, Pertsov AM, Jalife J. Frequency-dependent breakdown of wave propagation into fibrillatory conduction across the pectinate muscle network in the isolated sheep right atrium. Circ Res. 2002;90:1173-80.

CHAPTER 4

Bipolar electrograms characteristics at the left atrial – pulmonary vein junction: towards a new algorithm for automated verification of pulmonary vein isolation

Milad El Haddad, MS; Richard Houben, PhD; Benjamin Berte, MD; Frederic Van Heuverswyn, MD; Roland Stroobandt, MD, PhD; Yves Vandekerckhove, MD; Rene Tavernier, MD; Mattias Duytschaever, MD, PhD

This original research article was accepted for publication in the journal Heart Rhythm in August 2014

Abstract

Background: Pulmonary vein (PV) ablation is an effective treatment for recurrent atrial fibrillation. Verification of PV isolation (PVI) is challenging due to the presence of both PV and far-field potentials in the bipolar electrograms (EGM) recorded at the left atrial-pulmonary vein (LA-PV) junction. We aimed 1) to characterize algorithmically LA-PV potentials recorded before and after proven PVI and 2) to develop and validate an algorithm to automatically differentiate non-isolated from isolated PVs.

Methods: We characterized 1440 EGMs (from 160 PV recordings) recorded at the LA-PV junction during sinus rhythm before and after PVI in 61 patients (library). In each EGM (3 seconds), LA-PV potentials were detected and averaged into one LA-PV potential for further analysis. Using custom-made software, we determined for each LA-PV potential its type (low voltage, monophasic, biphasic, triphasic, multiphasic, or double potential) and parameters (peak-to-peak amplitude, maximal slope, minimal slope, and sharpest peak). Based upon the vein-dependent prevalence of a given type before and after PVI (first step) and based upon vein-and type-dependent cutoff values in parameters specific for recordings before and after PVI (second step), we developed a two-step algorithm to differentiate non-isolated from isolated PVs. In another dataset of 20 patients (90 PV recordings) we prospectively validated this algorithm.

Results: Characteristics before and after PVI were as follows: low voltage (10±7% vs. 36±15%, $p<0.01$), monophasic (13±4% vs. 27±9%, $p<0.01$), biphasic (18±4% vs. 21±9%, N.S), triphasic (22±5% vs. 11±13%, $p<0.01$), multiphasic (26±7% vs. 3±3%, $p<0.01$), double potentials (11±5% vs. 2±1%, $p<0.01$), peak-to-peak amplitude

(0.97±0.21 vs. 0.35±0.23 mV, $p<0.01$), maximal slope (0.179±0.033 vs. 0.071±0.029 mV/ms, $p<0.01$), minimal slope (0.030±0.003 vs. 0.024±0.002 mV/ms, $p<0.01$), and sharpest peak (1.82±0.26 vs. 3.45±0.85 degrees, $p<0.01$). Prospective validation of the two-step algorithm showed overall 100% sensitivity and 87% specificity to differentiate non-isolated from isolated PVs.

Conclusions: (1) We algorithmically characterized LA-PV potentials before and after PVI in a large dataset (library of types and parameters). (2) This library enabled us to develop an accurate two-step algorithm to automatically differentiate non-isolated from isolated PVs. The two-step algorithm is objective and reliable to assess PV isolation without the need of pacing maneuvers.

4.1 Introduction

Catheter-based pulmonary vein (PV) ablation is a successful therapeutic strategy in patients with drug-resistant and symptomatic recurrent atrial fibrillation (AF).[1] Complete electrical PV isolation (PVI) is an essential endpoint for successful outcome.[1,2,3] Verification of PVI can be challenging because bipolar electrograms (EGM) recorded by circular mapping catheters (CMC) at the left atrium - pulmonary vein (LA-PV) junction may contain local PV potentials (PVP) and far-field potentials (FFP).[3] We 1) aimed to characterize systematically the type and parameters of LA-PV potentials before and after PVI in a large dataset of recordings (library of 1440 EGMs), and 2) introduced and validated an algorithm to automatically verify PV isolation.

4.2 Methods

Database

Data were collected from 61 patients undergoing electroanatomical mapping (EAM)-guided first circumferential PVI for drug-refractory, symptomatic and recurrent AF (58 ± 9 years, 78% males, 80% paroxysmal AF, no structural heart disease). For characterization of LA-PV potentials, 61 patients were studied. From these patients, we selected only those PV recordings: 1) where PV automaticity was observed after ablation (unambiguous proof of isolation) and 2) where baseline PV recording was available with the CMC at the same position as after PVI. As such, we performed paired analysis in 160 PV recordings: 16 left superior PV (LSPV), 11 left inferior PV (LIPV), 37 right superior PV (RSPV), and 16 right inferior PV (RIPV). This resulted in a library of 1440 LA-PV electrograms (9 bipoles per PV recording). The library (n=1440) was used for the characterization of the LA-PV potentials and development of an algorithm to verify PV isolation.

For prospective validation of the algorithm, we collected from another 20 patients unpaired recordings from 43 PVs before isolation (11 LSPV, 7 LIPV, 18 RSPV, 7 RIPV) and 47 PVs after isolation (11 LSPV, 7 LIPV, 18 RSPV, 11 RIPV). The study received approval from the local ethical committee.

Ablation procedure and recording catheters

A decapolar catheter was positioned in the coronary sinus (CS). After transseptal puncture, 3D reconstruction of the LA was made by an EAM system (Carto®, Biosense Webster, Diamond Bar, CA, USA) using an irrigated-tip ablation catheter (NaviStar ThermoCool, Biosense Webster). The ablation procedure consisted of encircling ipsilateral PVs as a single unit by a continuous circular lesion set during sinus rhythm. Except for the anterior aspect of the left PVs, lesions were created 10 to 20mm outside of the ostia as defined from the 3D map. The continuous lesion set was made by point-by-point radiofrequency (RF) applications (20 to 35 W, 30 to 60s, max 42°C, irrigation 20ml/min). The PVs were continuously assessed for electrical disconnection using a decapolar (2 mm electrodes, spacing 8mm) CMC (Lasso®, 2515 variable catheter, Biosense Webster) placed at the LA-PV junction. The endpoint for ablation was LA-PV entry block, defined as elimination of all PV potentials or PV automaticity (unambiguous proof of entry block).[4]

Intracardiac EGMs were recorded by the Bard EP system (Boston Scientific, Natick, MA, USA) at a sampling rate of 1000 Hz and filtered 10-250 Hz. For each selected PV, we extracted 3 second recordings from the surface ECG (lead II), the proximal bipole of the CS, and 9 bipolar EGMs from the CMC (1-2, 2-3, 3-4,...). Each CMC bipole was assigned a hemisphere (anterior or posterior) based upon its anatomical location determined from the EAM. Representative examples of recordings before and after PVI (with automaticity) are shown in figure 1.

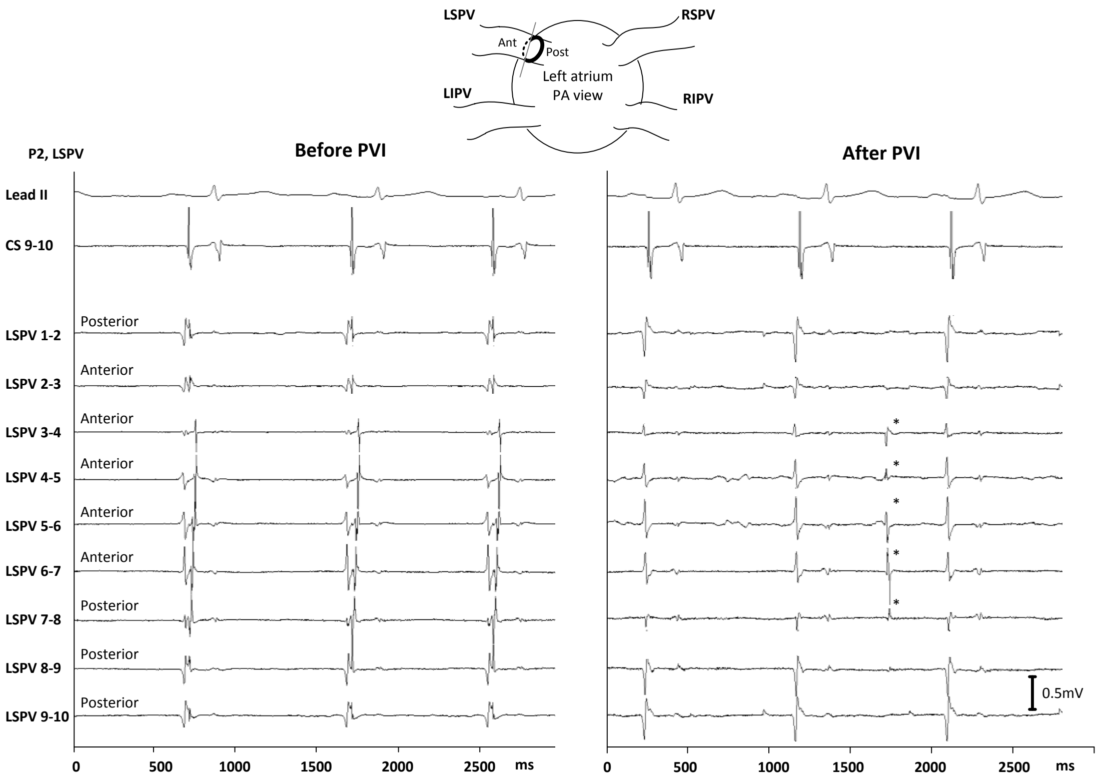

Figure 4-1: *Electrogram tracings from the surface ECG lead II, proximal CS, and circular mapping catheter (CMC) before (left panel) and after PVI (right panel). The CMC is positioned at the LA-PV junction of the LSPV (patient 2). Asterisk = automaticity. CS: coronary sinus, PVI: pulmonary vein isolation, LA-PV: left atrium-pulmonary vein, LSPV: left superior pulmonary vein.*

Pre-processing of LA-PV electrograms

Pre-processing of the EGMs was performed offline in Matlab (The MathWorks, Inc., Natick, MA, USA). First, atrial potentials were detected on the CS electrogram (using a peak detection algorithm) to determine the atrial activation window of interest (Fig.

2, step a). Second, non-atrial potentials were blanked from the LA-PV electrogram of interest (Fig. 2, step b). Third, LA-PV potentials in the LA-PV electrogram were detected using a peak detection algorithm (Fig. 2, step c). Then, all detected LA-PV potentials (ranging from 2 to 6 beats) were time aligned (using the maximal positive or negative peak) and averaged into one LA-PV potential (Fig. 2, step d).

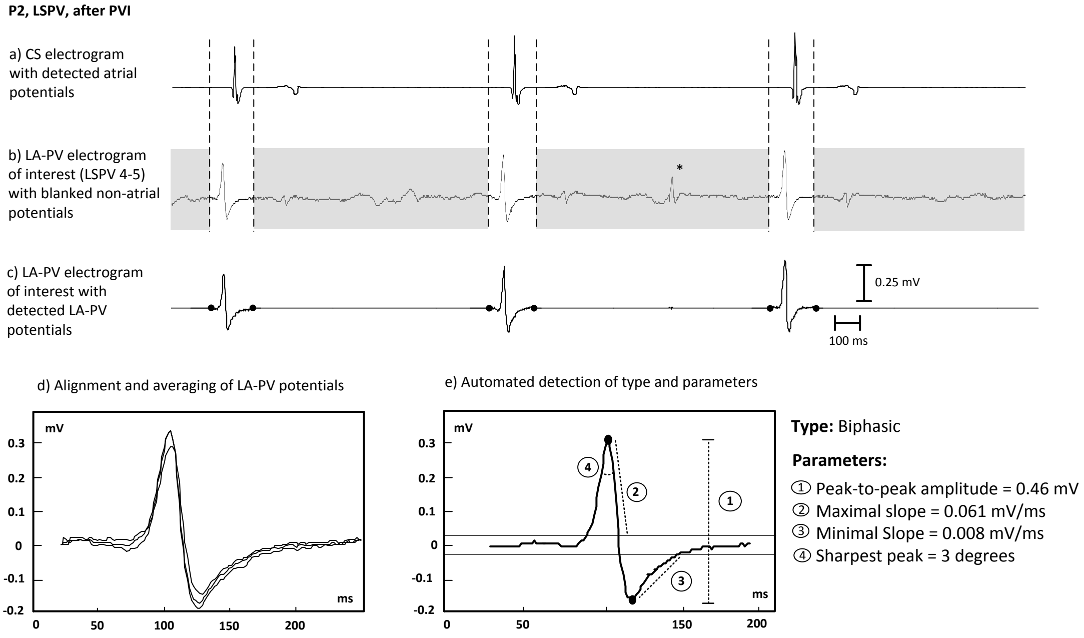

Figure 4-2: *Preprocessing and algorithmic characterization of the LA-PV electrograms resulting in automated detection of type (biphasic) and parameters. LA-PV: left atrium-pulmonary vein, CS: coronary sinus.*

Typology of LA-PV potentials before and after PVI

Custom-made Matlab software was used to determine the type of LA-PV potential based upon the number of detected peaks (Fig. 2, step e). A local maximum was considered a valid peak (regardless of polarity) if the amplitude was above the dynamic EGM noise threshold and if the degree of curvature of the local maximum was more than 22.5 degrees. The LA-PV potential was algorithmically defined as: 1) low voltage (no peaks), 2) monophasic (one peak), 3) biphasic (two peaks), 4) triphasic (three peaks), 5) multiphasic (4 or more peaks), or 6) double potential (in the presence of at least 2 peaks separated by an iso-electric window of 25ms). Analysis was performed for all EGMs (n=1440). To compare typology before and after PVI, results were summarized per PV and hemisphere.

Amplitude, slopes, and peak-angle of LA-PV potentials

Custom-made Matlab software was used to calculate four numerical parameters of the LA-PV potential for every EGM except for low voltage (Fig. 2, step e): 1) peak-to-peak amplitude, defined as the amplitude difference between the maximal positive and negative peaks; 2) maximal slope: to identify the maximal slope within the LA-PV potential, we calculated the average dv/dt for each upstroke and downstroke of the peak(s). The maximal slope was defined as the maximal average dv/dt; 3) minimal slope, defined as the minimal average dv/dt; 4) sharpest peak, defined as the minimal angle between the upstroke and downstroke of the peak(s). Analysis was performed for each EGM (n=1440). To compare the parameters before and after PVI, results were summarized per PV, hemisphere, and type.

Development of an algorithm for automated verification of PV isolation

We hypothesized that vein-dependent prevalence of a given type before and after PVI might be used to differentiate non-isolated from isolated PVs. Therefore, we determined for each PV recording (n=160) the overall likelihood (OL) that the PV (still) contains PVPs. OL (ranging from -100% to +100%) was used as the first step in the algorithm and was calculated as:

$$\frac{\sum_{i=1}^{9} PrevalenceBefore_{(i)} - \sum_{i=1}^{9} PrevalenceAfter_{(i)}}{\sum_{i=1}^{9} PrevalenceBefore_{(i)} + \sum_{i=1}^{9} PrevalenceAfter_{(i)}} x100$$

where i is the number of bipole.

We further hypothesized that PV- and type-dependent cutoff values in parameters specific for LA-PV potentials before and after PVI could be used to differentiate non-isolated from isolated PVs. For this, the number of specific parameters was used as a weighing factor for the prevalence of that type before and after PVI. Therefore, we determined for each PV the modified overall likelihood (MOL) that the PV (still) contains PVPs. MOL (ranging from -100% to +100%) was used as the second step in the algorithm and was calculated as:

$$\frac{\sum_{i=1}^{9} ModifiedPrevalenceBefore_{(i)} - \sum_{i=1}^{9} ModifiedPrevalenceAfter_{(i)}}{\sum_{i=1}^{9} ModifiedPrevalenceBefore_{(i)} + \sum_{i=1}^{9} ModifiedPrevalenceAfter_{(i)}} x100$$

where i is the number of bipole.

In case the LA-PV potential did not have any specific type-dependent parameters, MOL was equal to OL value.

Prospective validation of the two-step algorithm

The overall accuracy of the two-step algorithm to differentiate non-isolated from isolated PVs was prospectively evaluated in 20 patients (dataset of 90 PV recordings).

Statistical analysis

Continuous data are presented as mean±standard deviation. Significant difference in means between groups was calculated using Student’s t-test. A p value of <0.05 was considered statistically significant.

4.3 Results

Types of LA-PV potentials before and after PVI

Overall (n=1440) before PVI, there was a higher prevalence of triphasic (22±5% vs. 11±13%, p=0.036), multiphasic (26±7% vs. 3±3%, p<0.001), and double potentials (11±5% vs. 2±1%, p <0.001) as compared to after PVI. Vice versa, after PVI there was a higher prevalence of low voltage (10±7% vs. 36±15%, p<0.001), and monophasic potentials (13±4% vs. 27±9%, p=0.001). The prevalence of biphasic potentials was not significantly different before and after PVI (18±4% vs. 21±9%, N.S).

We also compared the difference in typology before and after PVI per PV and hemisphere. Representative types of LA-PV potentials recorded at the LA-PV junction at the anterior hemisphere of the RSPV before and after PVI in 4 patients are given in figure 3 (37 LA-PV potentials from the library). Before PVI, there was high prevalence of triphasic (n =4, 24%), multiphasic (n=4, 24%), and double potentials (n=3, 18%), whereas after PVI there was a shift towards more low voltage (n=7, 41%) and monophasic potentials (n=6, 35%). The overall results, for the RSPV anterior (Fig. 4, panel d, 37 PVs, 340 potentials) show a shift in the prevalence of types before and after PVI (low voltage: 26% to 53%, monophasic: 15% to 33%, triphasic: 17% to 1%, multiphasic: 14% to 0%, and double potentials: 15% to 3%). A similar shift was observed for the other PVs and hemispheres (Fig. 4, panels a, b, c, e, f, g, and h): the majority of potentials before PVI were triphasic, multiphasic, and double potentials (except for RSPV anterior - panel d and LIPV anterior -panel e), whereas after PVI, the majority of potentials were low voltage, monophasic, and biphasic.

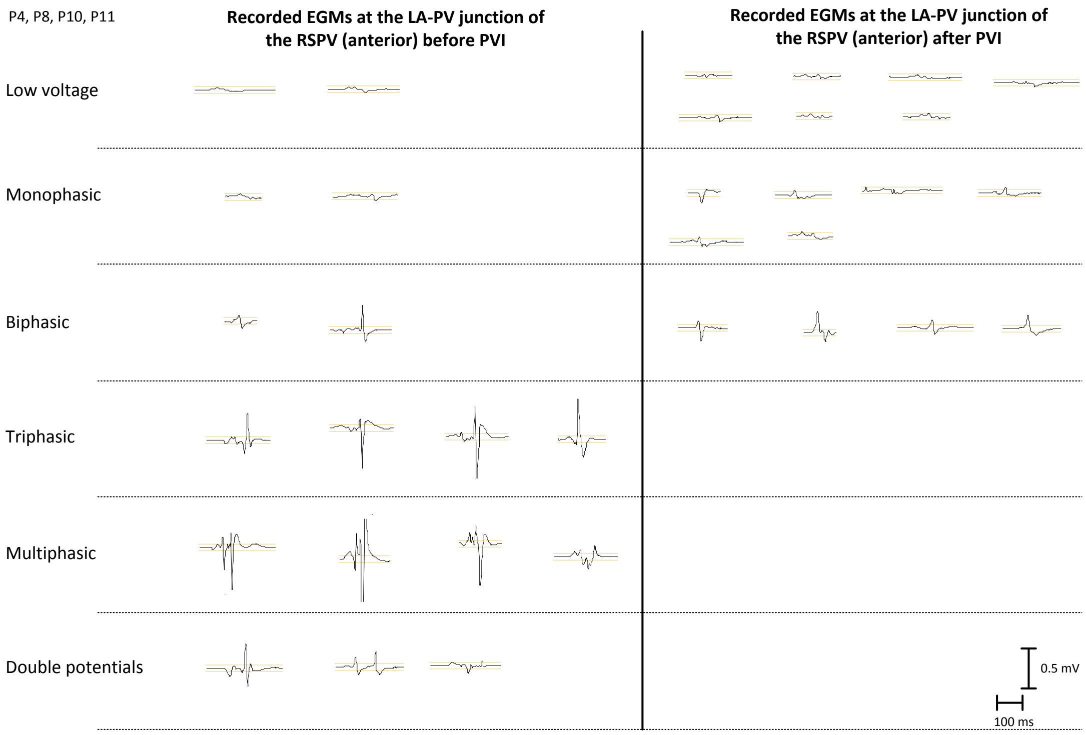

Figure 4-3: *Representative example of morphology distribution of LA-PV potentials in 4 RSPVs before and after PVI. Before PVI (left side), triphasic, multiphasic, and double potentials were more prevalent than after PVI (right side). After PVI, the LA-PV potentials are more low voltage, monophasic, and biphasic potentials. Orange lines represent the dynamic noise levels specific for each potential. LA-PV: left atrium-pulmonary vein, RSPV: right superior pulmonary vein. PVI: pulmonary vein isolation.*

Amplitude, slopes, and peak-angle of LA-PV potentials

Overall (n=1440) and independent of the type of potential, we observed (before compared to after PVI) a higher peak-to-peak amplitude (0.97±0.21 vs. 0.35±0.23 mV, p<0.0001), a higher maximal slope (0.179±0.033 vs. 0.071±0.029 mV/ms, p<0.0001), a higher minimal slope (0.030±0.003 vs. 0.024±0.002 mV/ms, p=0.0003), and a sharper peak (1.82±0.26 vs. 3.45±0.85 degrees, p=0.0015). Despite the significant differences, all parameters showed great overlap in range before and after PVI.

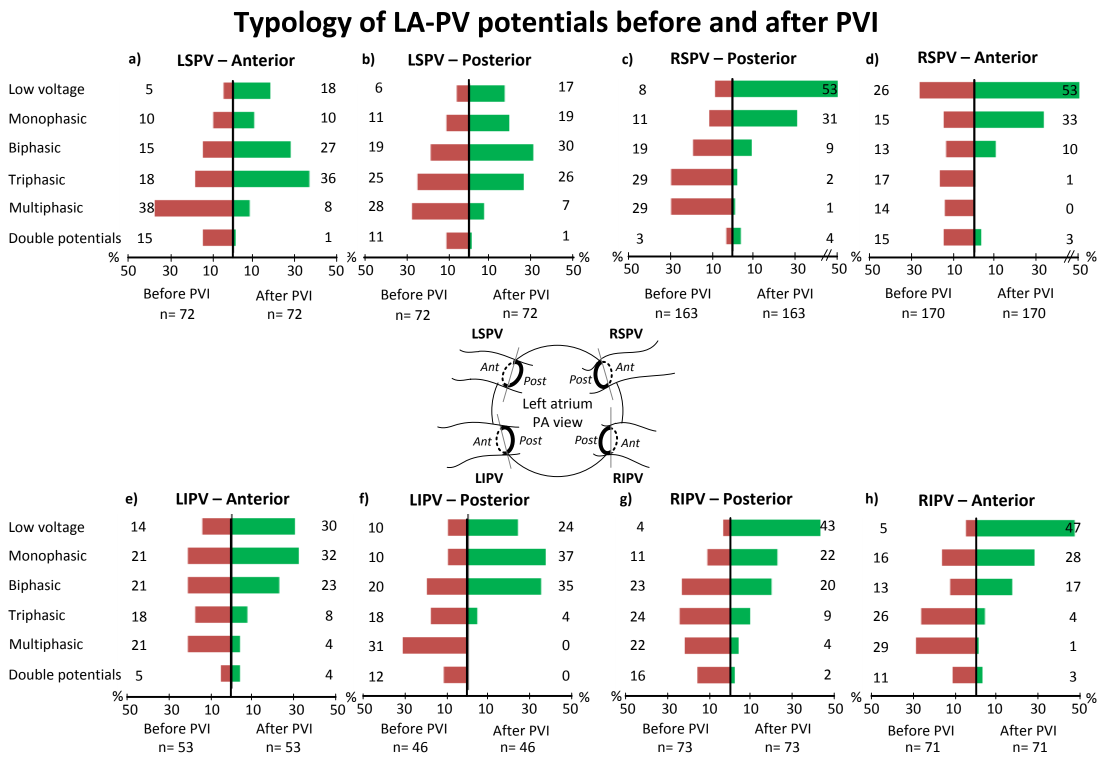

Figure 4-4: *Library of type of LA-PV potentials. Overall distribution of type per hemisphere and PV are expressed in percentages. LSPV: left superior, LIPV: left inferior, RSPV: right superior, RIPV: right inferior pulmonary vein. Ant: anterior, Post: posterior, PVI: pulmonary vein isolation.*

We also compared the difference in the amplitude, slopes, and peak-angle before and after PVI per PV, hemisphere, and type. A representative example of a triphasic potential recorded at the posterior hemisphere of the LSPV before and after PVI is given in figure 5 (top left panel). Compared to the triphasic potential after PVI, the triphasic potential before PVI shows a higher voltage (2.69 vs. 0.73 mV), a steeper slope (0.63 vs. 0.05mV/ms), and a sharper angle (0.4 vs. 3 degrees).

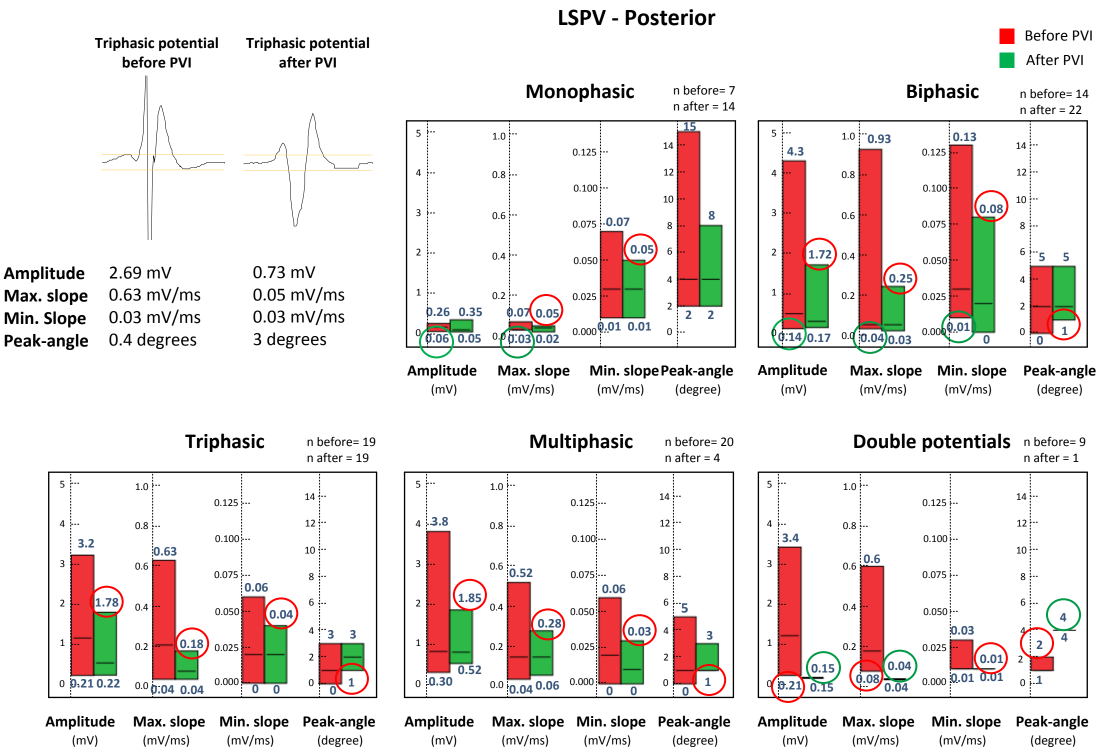

Figure 4-5: *Top left panel, representative example of triphasic potential recorded at the LA-PV junction of the LSPV posterior hemisphere before and after PVI. Box plots show the overall results of parameters specific for each type in the LSPV posterior hemisphere (red: before PVI, green: after PVI). Mono=monophasic, bi=biphasic, tri=triphasic, multi=multiphasic, DP=double potentials, LSPV=left superior pulmonary vein, PVI= pulmonary vein isolation.*

The results of the parameters for each type of potential in the LSPV posterior hemisphere are presented as box plots (P0 to P100) in the other parts of figure 5. Now, based upon the box plots, we could identify the following cutoffs specific for LA-PV potentials in the LSPV posterior hemisphere before PVI (red circles): 1) monophasic: maximal slope >0.05mV/ms, minimal slope >0.05mV/ms, 2) biphasic: amplitude >1.72mV, maximal slope > 0.25mV/ms, minimal slope >0.08mV/ms, angle < 1 degrees, 3) triphasic: amplitude >1.78mV, maximal slope >0.18mV/ms, minimal slope >0.04 mV/ms, peak-angle < 1 degrees, 4) multiphasic: amplitude >1.85mV, maximal slope >0.28mV/ms, minimal slope >0.03mV/ms, peak-angle < 1 degrees, and 5) double potentials: amplitude ≥0.21mV, maximal slope ≥0.08mV/ms, minimal slope >0.01mV/ms, peak-angle ≤2 degrees. Vice versa, the following cutoffs were specific for LSPV posterior recordings after PVI (green dotted circles): 1) monophasic: maximal slope <0.06mV/ms, minimal slope <0.03mV/ms, 2) biphasic: amplitude < 0.14mV, maximal slope <0.04mV/ms, minimal slope <0.01mV/ms, 3) triphasic: no specific parameters, 4) multiphasic: no specific parameters, and 5) double potentials: amplitude ≤0.15mV, maximal slope ≤0.04mV/ms, peak-angle ≥4 degrees.

The other - type dependent - results and cutoffs for each PV and hemispheres are given in a tabular format (supplemental tables 1-4). When compared per type, all parameters showed less overlap in range before and after PVI. Again, per-type-analysis allowed identification of cutoff values specific for LA-PV potentials either recorded before or after PVI.

Table 4.1,2,3,4: *Type dependent parameters*

LSPV - Anterior

Mean Min Max	Peak-to-peak amplitude (mV)		Maximal slope (mV/ms)		Minimal slope (mV/ms)		Sharpest peak (degree)	
	Before	After	Before	After	Before	After	Before	After
Monophasic	0.15 0.05 0.39	0.14 0.06 0.30	0.04 0.03 0.08	0.04 0.02 0.06	0.03 0.01 0.07	0.03 0.01 0.06	3.88 2.00 7.00	4.00 2.00 7.00
Biphasic	0.55 0.08 1.80	0.43 0.17 1.72	0.10 0.02 0.30	0.07 0.03 0.25	0.03 0.01 0.07	0.02 0.00 0.08	2.42 0.00 6.00	2.72 1.00 5.00
Triphasic	1.39 0.22 3.33	1.20 0.22 3.79	0.26 0.06 0.68	0.19 0.04 0.65	0.03 0.01 0.08	0.02 0.00 0.08	1.33 0.00 4.00	1.42 0.00 5.00
Multiphasic	1.76 0.27 4.16	1.24 0.78 1.55	0.34 0.11 0.97	0.23 0.13 0.34	0.03 0.00 0.15	0.01 0.00 0.02	0.68 0.00 2.00	0.71 0.00 1.00
Double potentials	0.73 0.22 1.58	1.87 1.87 1.87	0.14 0.03 0.04	0.02 0.02 0.02	0.02 0.00 4.00	0.02 0.02 0.02	2.00 1.00 4.00	1.00 1.00 1.00

LSPV – Posterior

Monophasic	0.14 0.06 0.26	0.14 0.05 0.35	0.04 0.03 0.07	0.04 0.02 0.05	0.03 0.01 0.07	0.03 0.01 0.05	4.67 2.00 15.00	4.41 2.00 8.00
Biphasic	1.08 0.14 4.30	0.48 0.17 1.72	0.19 0.04 0.93	0.07 0.03 0.25	0.04 0.01 0.13	0.02 0.00 0.08	2.40 0.00 5.00	2.81 1.00 5.00
Triphasic	1.33 0.21 3.20	0.65 0.22 1.78	0.22 0.04 0.63	0.09 0.04 0.18	0.02 0.00 0.06	0.02 0.00 0.04	1.30 0.00 3.00	1.83 1.00 3.00
Multiphasic	1.18 0.30 3.80	1.06 0.52 1.85	0.20 0.04 0.52	0.16 0.06 0.28	0.02 0.00 0.06	0.01 0.00 0.03	1.36 0.00 5.00	1.50 1.00 3.00
Double potentials	1.29 0.21 3.40	0.15 0.15 0.15	0.21 0.08 0.60	0.04 0.04 0.04	0.02 0.01 0.03	0.01 0.01 0.01	1.11 1.00 2.00	4.00 4.00 4.00

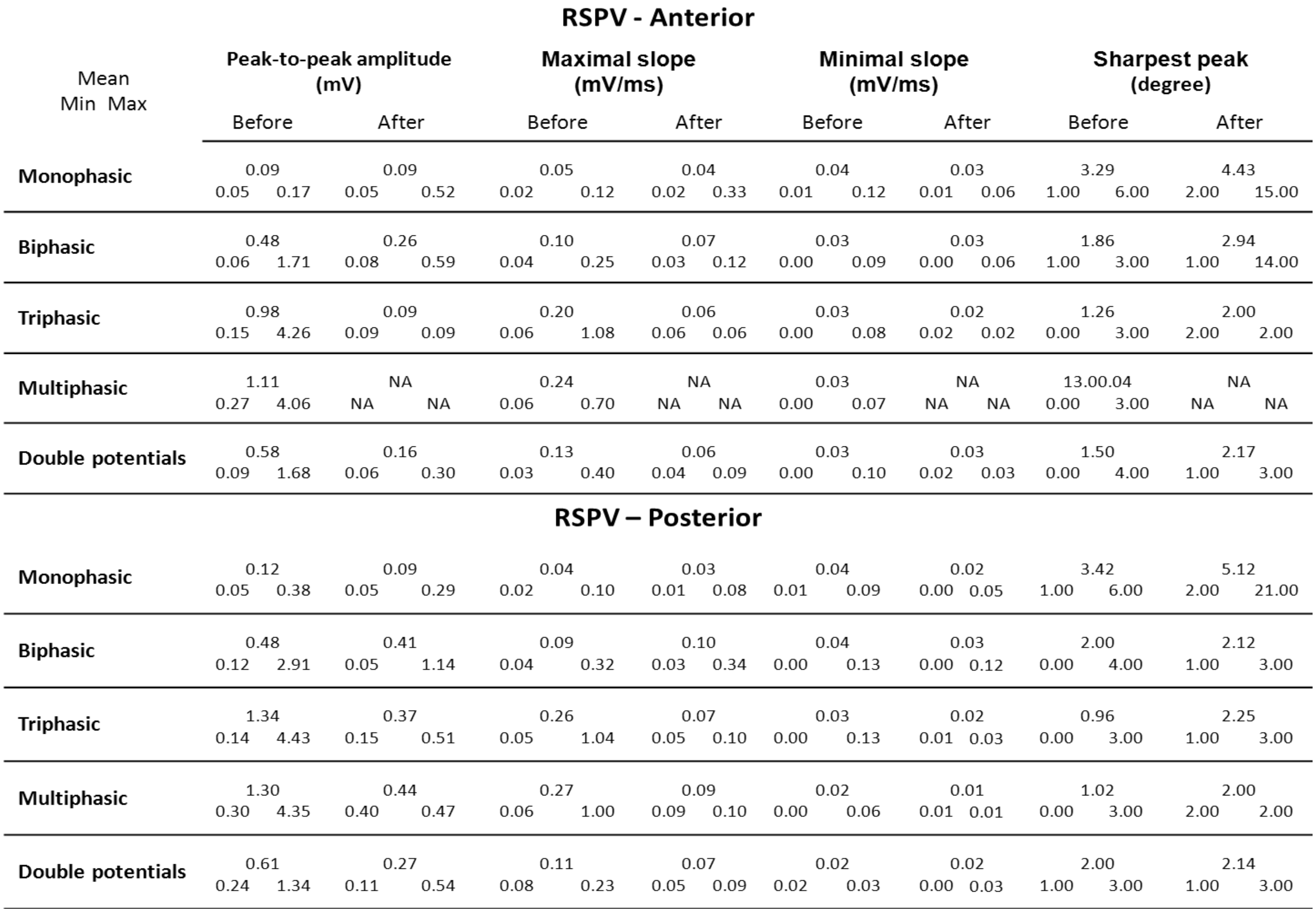

RSPV - Anterior

Mean Min Max	Peak-to-peak amplitude (mV)		Maximal slope (mV/ms)		Minimal slope (mV/ms)		Sharpest peak (degree)	
	Before	After	Before	After	Before	After	Before	After
Monophasic	0.09 0.05 0.17	0.09 0.05 0.52	0.05 0.02 0.12	0.04 0.02 0.33	0.04 0.01 0.12	0.03 0.01 0.06	3.29 1.00 6.00	4.43 2.00 15.00
Biphasic	0.48 0.06 1.71	0.26 0.08 0.59	0.10 0.04 0.25	0.07 0.03 0.12	0.03 0.00 0.09	0.03 0.00 0.06	1.86 1.00 3.00	2.94 1.00 14.00
Triphasic	0.98 0.15 4.26	0.09 0.09 0.09	0.20 0.06 1.08	0.06 0.06 0.06	0.03 0.00 0.08	0.02 0.02 0.02	1.26 0.00 3.00	2.00 2.00 2.00
Multiphasic	1.11 0.27 4.06	NA NA NA	0.24 0.06 0.70	NA NA NA	0.03 0.00 0.07	NA NA NA	13.00.04 0.00 3.00	NA NA NA
Double potentials	0.58 0.09 1.68	0.16 0.06 0.30	0.13 0.03 0.40	0.06 0.04 0.09	0.03 0.00 0.10	0.03 0.02 0.03	1.50 0.00 4.00	2.17 1.00 3.00

RSPV – Posterior

Mean Min Max	Peak-to-peak amplitude (mV)		Maximal slope (mV/ms)		Minimal slope (mV/ms)		Sharpest peak (degree)	
	Before	After	Before	After	Before	After	Before	After
Monophasic	0.12 0.05 0.38	0.09 0.05 0.29	0.04 0.02 0.10	0.03 0.01 0.08	0.04 0.01 0.09	0.02 0.00 0.05	3.42 1.00 6.00	5.12 2.00 21.00
Biphasic	0.48 0.12 2.91	0.41 0.05 1.14	0.09 0.04 0.32	0.10 0.03 0.34	0.04 0.00 0.13	0.03 0.00 0.12	2.00 0.00 4.00	2.12 1.00 3.00
Triphasic	1.34 0.14 4.43	0.37 0.15 0.51	0.26 0.05 1.04	0.07 0.05 0.10	0.03 0.00 0.13	0.02 0.01 0.03	0.96 0.00 3.00	2.25 1.00 3.00
Multiphasic	1.30 0.30 4.35	0.44 0.40 0.47	0.27 0.06 1.00	0.09 0.09 0.10	0.02 0.00 0.06	0.01 0.01 0.01	1.02 0.00 3.00	2.00 2.00 2.00
Double potentials	0.61 0.24 1.34	0.27 0.11 0.54	0.11 0.08 0.23	0.07 0.05 0.09	0.02 0.02 0.03	0.02 0.00 0.03	2.00 1.00 3.00	2.14 1.00 3.00

LIPV - Anterior

Mean Min Max	Peak-to-peak amplitude (mV)				Maximal slope (mV/ms)				Minimal slope (mV/ms)				Sharpest peak (degree)			
	Before		After		Before		After		Before		After		Before		After	
Monophasic	0.15		0.11		0.04		0.04		0.03		0.03		4.17		3.82	
	0.05	0.33	0.06	0.22	0.02	0.07	0.02	0.07	0.01	0.06	0.02	0.05	2.00	6.00	2.00	6.00
Biphasic	0.36		0.38		0.07		0.07		0.07		0.03		2.33		2.50	
	0.06	1.04	0.05	0.78	0.03	0.15	0.05	0.16	0.02	0.06	0.00	0.05	1.00	4.00	1.00	4.00
Triphasic	1.19		0.34		0.20		0.06		0.03		0.02		1.50		2.25	
	0.23	3.43	0.16	0.57	0.06	0.54	0.05	0.10	0.01	0.06	0.02	0.03	0.00	3.00	1.00	3.00
Multiphasic	1.16		1.77		0.20		0.37		0.01		0.02		1.50		0.50	
	0.22	2.60	1.61	1.93	0.06	0.59	0.28	0.46	0.00	0.04	0.01	0.03	0.00	3.00	0.00	1.00
Double potentials	0.47		0.19		0.12		0.04		0.04		0.02		1.67		3.50	
	0.18	0.69	0.16	0.21	0.08	0.22	0.03	0.06	0.03	0.06	0.02	0.02	1.00	2.00	3.00	4.00

LIPV – Posterior

Monophasic	0.09		0.14		0.04		0.04		0.03		0.02		3.60		4.88	
	0.05	0.14	0.05	0.46	0.03	0.05	0.02	0.12	0.02	0.03	0.01	0.05	3.00	4.00	2.00	8.00
Biphasic	0.45		0.41		0.08		0.08		0.03		0.02		2.40		3.13	
	0.12	0.73	0.06	1.72	0.04	0.18	0.02	0.29	0.01	0.09	0.00	0.03	1.00	5.00	0.00	15.00
Triphasic	1.23		0.39		0.22		0.09		0.03		0.03		1.78		1.00	
	0.18	3.26	0.35	0.43	0.06	0.59	0.09	0.10	0.01	0.05	0.03	0.03	0.00	4.00	1.00	1.00
Multiphasic	2.13		NA		0.35		NA		0.03		NA		0.75		NA	
	0.32	4.25	NA	NA	0.10	1.01	NA	NA	0.01	0.09	NA	NA	0.00	1.00	NA	NA
Double potentials	0.76		NA		0.14		NA		0.02		NA		2.33		NA	
	0.16	2.32	NA	NA	0.02	0.26	NA	NA	0.00	0.03	NA	NA	1.00	8.00	NA	NA

RIPV - Anterior

Mean Min Max	Peak-to-peak amplitude (mV)		Maximal slope (mV/ms)		Minimal slope (mV/ms)		Sharpest peak (degree)	
	Before	After	Before	After	Before	After	Before	After
Monophasic	0.47 0.05 1.47	0.09 0.05 0.21	0.08 0.01 0.18	0.03 0.01 0.08	0.05 0.01 0.12	0.02 0.00 0.08	3.54 1.00 10.00	6.36 2.00 22.00
Biphasic	0.35 0.18 0.96	0.19 0.08 0.30	0.07 0.02 0.13	0.05 0.03 0.09	0.03 0.01 0.06	0.02 0.00 0.04	2.70 1.00 6.00	3.24 1.00 7.00
Triphasic	1.37 0.13 4.40	0.54 0.23 0.76	0.24 0.04 0.88	0.09 0.05 0.14	0.03 0.00 0.09	0.03 0.02 0.04	1.19 0.00 4.00	2.00 1.00 3.00
Multiphasic	1.37 0.26 3.96	0.54 0.54 0.54	0.26 0.05 0.61	0.09 0.09 0.09	0.02 0.00 0.05	0.02 0.02 0.02	0.91 0.00 3.00	2.00 2.00 2.00
Double potentials	0.81 0.14 2.00	0.11 0.10 0.12	0.17 0.05 0.46	0.05 0.03 0.08	0.03 0.01 0.04	0.02 0.02 0.03	1.89 1.00 3.00	2.67 1.00 4.00

RIPV – Posterior

Monophasic	0.11 0.05 0.19	0.10 0.05 0.38	0.04 0.02 0.06	0.04 0.01 0.08	0.03 0.02 0.05	0.02 0.01 0.05	3.56 2.00 6.00	4.79 2.00 9.00
Biphasic	0.59 0.09 2.06	0.34 0.08 1.00	0.11 0.03 0.32	0.08 0.03 0.18	0.03 0.01 0.06	0.03 0.01 0.05	2.21 1.00 6.00	2.19 1.00 4.00
Triphasic	1.16 0.22 3.68	0.80 0.15 2.11	0.20 0.05 0.62	0.15 0.05 0.41	0.03 0.01 0.09	0.02 0.00 0.08	1.30 0.00 3.00	1.70 0.00 3.00
Multiphasic	1.61 0.34 4.12	0.76 0.36 1.21	0.27 0.08 0.63	0.14 0.05 0.20	0.03 0.00 0.06	0.01 0.00 0.02	0.94 0.00 3.00	1.25 1.00 2.00
Double potentials	0.90 0.08 3.00	0.43 0.19 0.68	0.15 0.05 0.41	0.05 0.04 0.06	0.03 0.01 0.06	0.02 0.02 0.02	1.38 0.00 3.00	2.50 2.00 3.00

Likelihood of presence of PV potentials in a PV recording based upon typology (overall likelihood – step 1)

Two representative PV recordings with their overall likelihood (OL) calculation are given in figure 6. In the top panel, a recording from the RSPV before isolation is shown. Automated typology indicates triphasic potentials in EGMs 1-2 and 9-10, multiphasic potentials in EGMs 2-3, 3-4, 4-5, and 5-6, biphasic potentials in EGMs 6-7 and 8-9, and double potentials in EGM 8-9. Next to the type of potentials we indicated the reported prevalence (library, Fig. 4 panel d) of that specific type for that given PV and hemisphere before and after isolation. As such, the OL that the recording contains PVP is calculated to be +75%. In the lower panel, a recording from the LIPV after PVI is shown. Now the automated typology and calculation of prevalence generates an OL of -35%.

In figure 7, we plotted for each LSPV, RSPV, LIPV, and RIPV (panels 1.a, 2.a, 3.a, and 4.a) the OL values before and after PVI. The mean OL was higher before PVI than after PVI (LSPV: 23±19% vs. -13±12%, RSPV: 24±36% vs. -41±16%, LIPV: 29±38% vs. -25±11%, and RIPV: 33±29% vs. -41±26%, p<0.0001 for all). Despite the significant difference, there was considerable overlap of OL value before and after PVI in 60 out of 160 PVs (38%, shaded areas). On the other hand, in 62% of PVs, the following OL cutoffs were specific for PV recordings before and after PVI respectively: In LSPV, OL>+12% and <-4%; in RSPV, OL>+33% and <-41%; in LIPV, OL>-2% and <-31%; in RIPV, OL>+16% and <-8%. These specific cutoffs were used in the first step of the two-step algorithm to differentiate non-isolated from isolated PVs. As such, the RSPV recording in figure 6 upper panel was correctly identified as non-isolated PV (OL=+75% >+33%) whereas the LIPV recording in the lower panel was correctly identified as an isolated PV (OL=-35% <-31%).

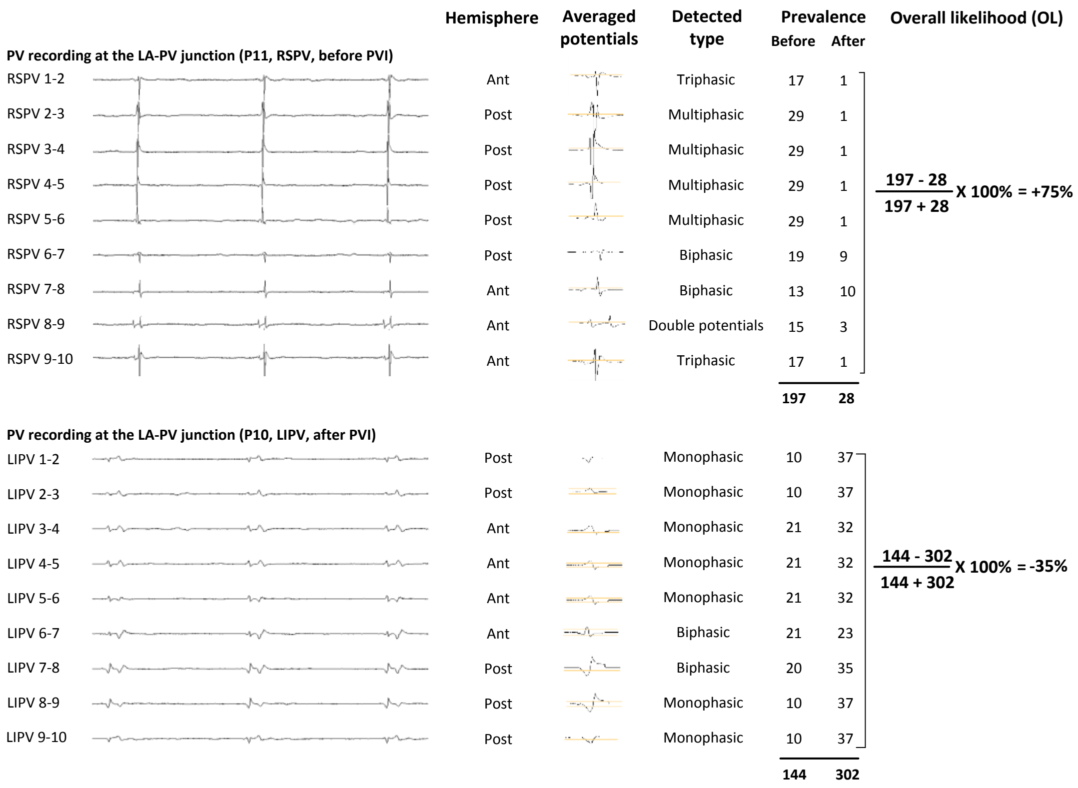

Figure 4-6: *Representative examples of the stepwise algorithm to analyze isolation of PV based upon the overall likelihood (OL) that a PV still contains PVP. Each bipole is assigned a hemisphere according to its position at the LA-PV junction, averaged into 1 single potential, and characterized by its type. The prevalence of that type - unique for each PV and hemisphere - is used to calculate the OL. See text for further explanation.*

Likelihood of presence of PV potentials in a PV recording based upon typology and parameters (modified OL - step 2)

For those PV recordings with OL values in the overlapping range (Fig. 7, shaded areas), we calculated the MOL. Representative examples of PV recordings with intermediate OL values (together with their MOL values) are given in figure 8. Although the LSPV recording in the upper panel was recorded before PVI, the OL was only -4% (non-conclusive first step). This was due to the presence of mainly triphasic potentials which occur equally or even more in isolated PVs (library, Fig. 4-panels a and b). Subsequent analysis of type-dependent parameters revealed that the

LA-PV potentials in EGM 1-2 (multiphasic with amplitude=2.7mV and max. slope=0.4mV/ms), EGM 4-5 (triphasic with max. slope=0.22mV/ms), and EGM 5-6 (triphasic with amplitude = 2.69mV, max. slope =0.63 mV/ms, and peak-angle=0.4degrees) had parameters specific for non-isolated PVs (see asterisks next to EGM). No parameters specific for isolated PVs were identified. As a result, MOL value was +100%.

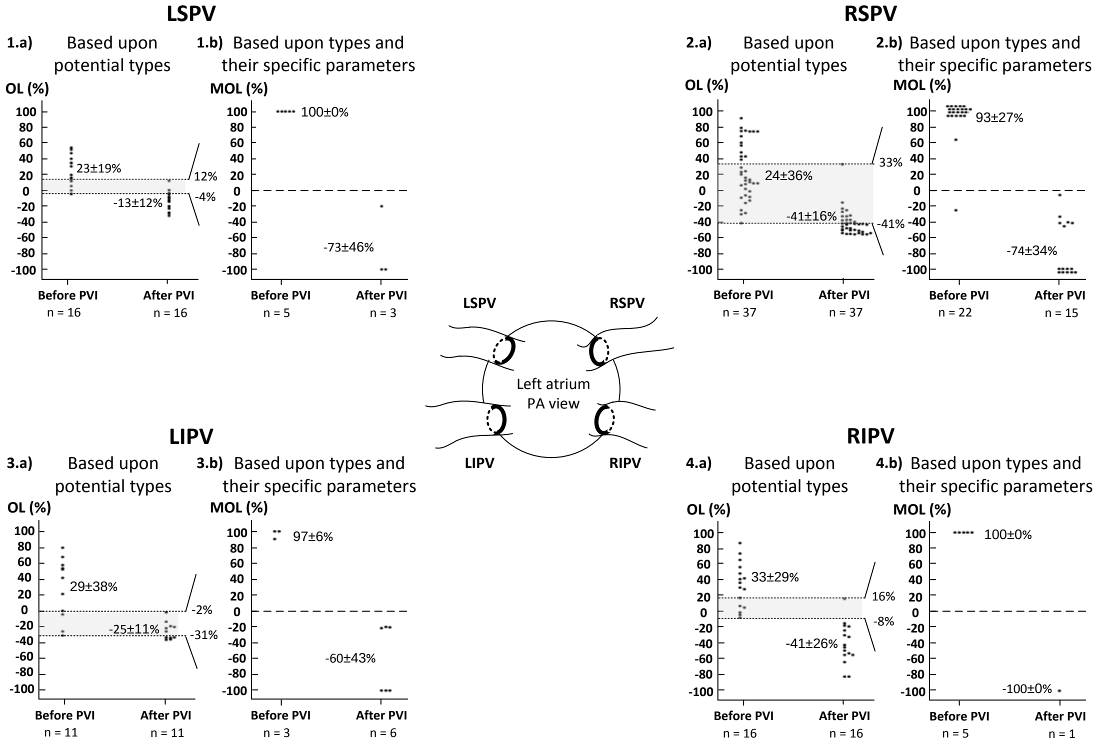

Figure 4-7: *Overall results of the stepwise approach to analyze isolation of PV based upon the overall likelihood (OL) and modified overall likelihood (MOL) that a PV contains PVP. PVs with intermediate OL (gray area in panels 1.a, 2.a, 3.a, and 4.a) proceed to the second step.*

In the lower panel, a recording from an isolated RIPV is plotted. The OL of +16% was indecisive due to the presence of mainly triphasic and multiphasic potentials.

Type-dependent analysis revealed that the LA-PV potentials in EGM 1-2 (biphasic with amplitude=0.1mV), EGM 2-3 (biphasic with amplitude=0.17mV, min. slope=0.009mV/ms, peak-angle=7degrees), and EGM 9-10 (monophasic with peak-angle = 15 degrees) had parameters specific for isolated PVs (see asterisks next to EGM). As a result MOL value was -100%.

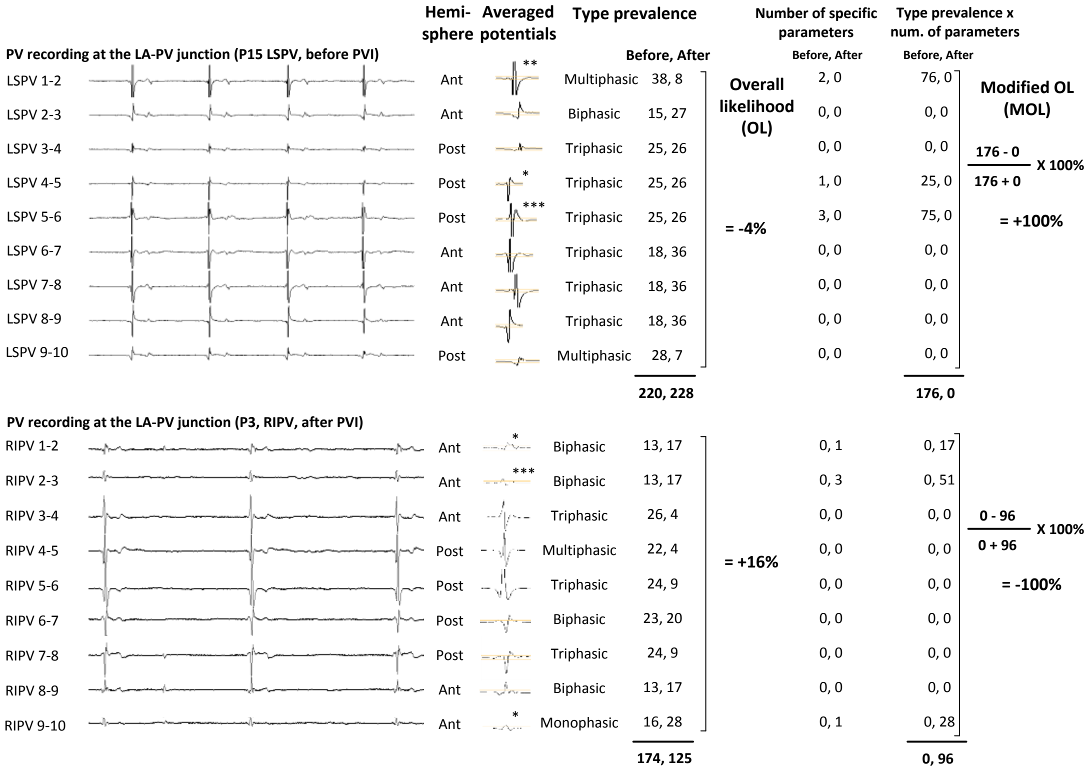

Figure 4-8: *Representative examples of the stepwise algorithm to analyze isolation of PV based upon the modified overall likelihood (OL) that a PV still contains PVP. Each bipole is assigned a hemisphere according to its position at the LA-PV junction, averaged into 1 single potential, and characterized by its type. In step 1, the prevalence of that type - unique for each PV and hemisphere - is used to calculate the overall likelihood (OL) that a PV contains PVP. PVs with intermediate OL (in this examples, -4% and +16%) proceed to step 2 where the number parameters of specific parameters for each type is used as a weighing factor for the prevalence of type.*

In figure 7 we plotted for each intermediate OL value (shaded area) the MOL (panels 1.b, 2.b, 3.b, 4.b). Overall, the modified OL ranged between -100% and +100%. The mean modified OL was higher before than after PVI (LSPV: 100±0% vs. -73±46%, RSPV: 93±27% vs. -74±34%, LIPV: 97±6% vs. -60±43%, RIPV: 100±0% vs. -100±0%, p<0.0001 for all). In contrast to OL, there was no overlap in the MOL value before and after PVI. A MOL value of 0% was used as a cutoff in the second step of the algorithm to differentiate non-isolated from isolated PVs (MOL > 0% for isolated PVs and < 0% for non-isolated PVs).

Prospective validation of the two-step algorithm

The flowchart of the two-step algorithm is given in figure 9. We evaluated prospectively (20 patients) the accuracy of the two-step algorithm in a dataset of 90 PV recordings (unpaired analysis of 43 before and 47 after PVI). The algorithm accurately identified PVs as non-isolated (still containing PVP) with 100% sensitivity and 87% specificity (accuracy = 93%, precision= 88%). The algorithm showed 100% sensitivity and 91% specificity in LSPV recordings, 100% sensitivity and 86% specificity in LIPV recordings, 100% sensitivity and 89% specificity in RSPV recordings, and 100% sensitivity and 82% specificity in RIPV recordings.

The algorithm differentiated 65 out of 90 PVs in the first step (overall=72%, LSPV=77%, RSPV=64%, LIPV=64%, and RIPV=89%), of which, all were correctly classified except for 1 LIPV. In the second step (n=25, 28%), 20 PVs were correctly classified, whereas 5 PVs were misclassified (as containing PVP although proven isolated in LSPV= 1, RSPV= 2, and RIPV= 2). These misclassified PVs were not characterized by any type-dependent specific parameters (i.e. MOL value was equal to OL value).

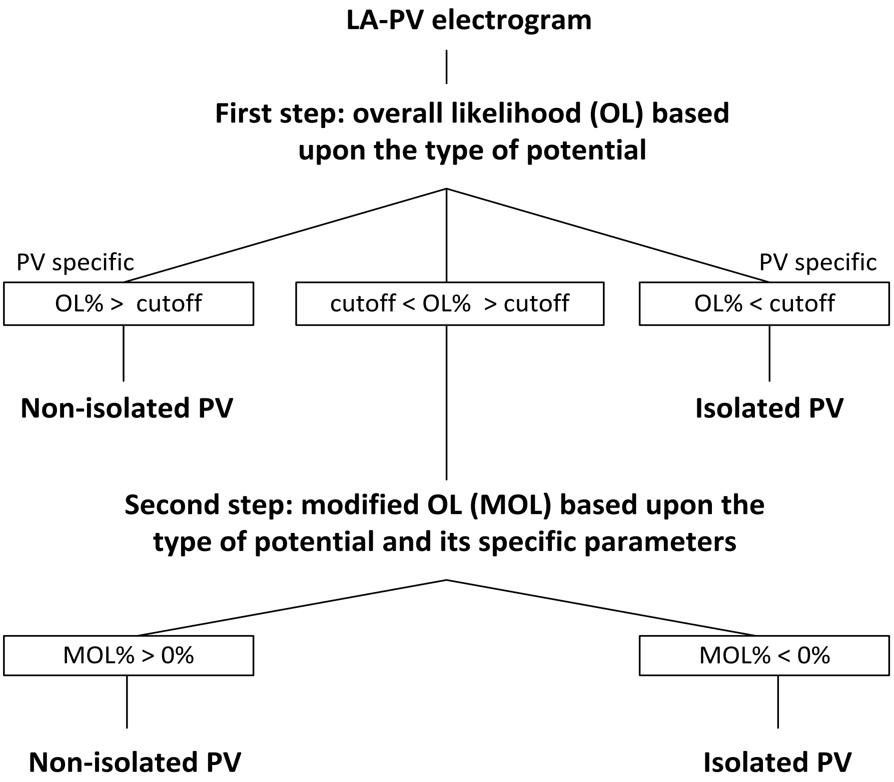

Prospective validation

	LSPV (n=22)	LIPV (n=14)	RSPV (n=36)	RIPV (n=18)	Overall (n=90)
Sensitivity	100 %	100 %	100 %	100 %	100 %
Specificity	91 %	86 %	89 %	82 %	87 %
Accuracy	95 %	93 %	94 %	89 %	93 %
Precision (PPV)	92 %	88 %	90 %	78 %	88 %

Figure 4-9: *Flowchart of the two-step algorithm to identify isolation based upon the overall likelihood (OL) and modified OL that the PV contains PVP. Lower panel: table of sensitivity, specificity, accuracy, and precision (positive predictive value) for the two-step algorithm in the prospective dataset (20 patients, 90 PVs).*

4.4 Discussion

Main findings

We algorithmically characterized 1440 left atrial – pulmonary vein bipolar electrograms, recorded by a circular mapping catheter during sinus rhythm before and after PVI (library of vein-specific types and parameters). Based upon this library we introduced an automated and robust algorithm to automatically differentiate between non-isolated and isolated PVs (93% accuracy).

Prior description of electrograms recorded at the LA-PV junction

Limited quantitative data is available about the characteristics of EGM recorded at the LA-PV junction before and after PVI. While PVs are the sources of pulmonary vein potentials (PVP), anatomical structures adjacent to the PVs are the sources of far-field potentials (FFP). Shah et al studied the characteristics of PVP and FFP before PVI in the left PVs (35 LSPV and 20 LIPV).[5] During sinus rhythm, PVP and FFP overlapped in a single potential in 63% of the LSPV and 70% of the LIPV. Upon CS pacing, the single potential splited into a double potential (100% in LSPV and 80 % in LIPV). The first potential (identified as FFP) was characterized by low amplitude (LSPV: 0.4±0.3, LIPV: 0.15±0.13 mV) and low slope (LSPV:0.039±0.03, LIPV:0.015±0.014 mV/ms), whereas the second potential (identified as PVP) was characterized by high amplitude (LSPV: 0.9±0.6, LIPV: 0.8±0.5mV), and steeper slope (LSPV:0.17±0.08, LIPV:0.16±0.09 mV/ms). The amplitude and slope however, showed considerable overlap between PVP and FFP, indicating that they are not reliable parameters to differentiate between PVP and FFP.[5] Even though the measurement method was not reported and no results were given for the septal veins, these findings are in line with our algorithmic results showing overlap in amplitude and slope when not compared per type of EGM.

In a different study, Shah et al. evaluated the characteristics of FFP in the RSPV (114 patients) after PVI.[6] FFP (all originating from the superior vena cava) were identified in 23% of the RSPV and were characterized by low amplitude (0.29±0.17mV) and short timing to the onset of P-wave (17±12ms). The authors concluded that timing to the onset of the P-wave (< 30ms) can identify FFP after PVI during sinus rhythm with high sensitivity and specificity (92% and 100%).[6]

Tada et al.[7] characterized PVP and atrial potentials (i.e. FFP) before PVI in LSPV, LIPV, and RSPV (n=20 all) by analyzing several parameters (using digital calipers) of the unipolar and bipolar EGM. After splitting PVP from FFP (by pacing), they observed that in bipolar EGMs, PVP amplitude was higher and the width was shorter than in FFP for all veins. The morphology of the unipolar was always biphasic for FFP and PVP, and the unipolar slope was greater in PVP than in FFP.[7]

None of the above studies consistently reported the detailed morphology of the B-EGMs for all veins and none characterized the B-EGM recorded during sinus rhythm before PVI (i.e. superimposed PVP + FFP).

Detailed morphology and characteristics of bipolar electrograms recorded at the LA-PV junction before and after PVI (library)

We constructed a library of EGMs before (PVP+FFP) and after PVI (FFP) and determined algorithmically per vein and hemisphere the morphology type and its distribution. This library of EGMs per PV and hemisphere (Fig. 4) can be used as a template in the EP lab to guide visual interpretation of PVI. We observed that before PVI, due to aliasing of PVP and FFP, the EGM complex contained greater number of peaks (triphasic, multiphasic, and double potentials), whereas EGM recorded after unambiguous PVI (FFP only) were characterized by low voltage, monophasic, and biphasic potentials. Additionally, we determined for each vein, hemisphere, and type of EGM, the amplitude, maximal slope, minimal slope, and peak-angle. Differences in LA-PV EGM amplitude and slopes before and after PVI were in line with prior reports (roughly before PVI >1mV and >0.15mV/ms whereas after PVI <0.5mV and <0.1mV/ms). A sharper peak in the LA-PV EGM before PVI (1.82±0.26 vs. 3.45±0.85 degrees) can be explained by the local activation of the PV sleeve under the electrodes. Overall, there was significant overlap in amplitude, maximal slope, minimal slope, and peak-angle values when comparing recordings before and after PVI. This overlap was significantly reduced (and in some completely avoided) by analyzing all parameters per type of EGM (Fig. 5).

The automated two-step algorithm for verification of PV isolation

Conventionally, PV isolation is verified by visual interpretation of (changes in) EGMs recorded by a circular multi-electrode catheter positioned at the LA-PV junction. Assessment of PVI (absence of PVP) however, remains challenging as FFP are recorded at the LA-PV junction before and after PVI.[3] To improve accuracy in differentiating PVP from FFP, pacing maneuvers can be used.[5,6,7,8] Alternatively, unipolar EGMs can been used to differentiate PVP from FFP. Tada et al. showed that in the presence of PVP (i.e. before PVI), the unipolar EGM recorded on the ablation catheter has the same morphology as the adjacent EGM recorded on the CMC.[9] Nevertheless, assessment of PVI remains ambiguous. As such, an objective and accurate method for identification of PVP and FFP could be advantageous.

To the best of our knowledge, algorithmic verification of PV isolation has not been reported yet. We introduced an automated and robust two-step algorithm based upon: 1) the vein-dependent prevalence of a given type before and after PVI (first step) and, 2) vein-and type-dependent cutoff values in parameters specific for recordings before and after PVI (second step). Basically we determined for a given PV recording the overall likelihood that it (still) contains PVP (step 1). The more the overall likelihood is closer to its limits (-100% or +100%), the more it is assertive that the PV is isolated (-100%) or not isolated (+100%). For those PVs with overall likelihood closer to 0% (i.e. within the cutoffs), we calculated the modified overall likelihood by using the unique parameters of each typology as a weighing factor (step 2). As such, the modified overall likelihood was increased or decreased towards the limits (-100% or +100%) to give an assertive indication of isolation.

The two-step algorithm showed 100% sensitivity and 87% specificity to detect presence of PVP (accuracy 93%). As such, all non-isolated PVs were classified correctly (no false negative) whereas minority of the isolated PVs were classified as non-isolated (false positive).

Clinical implications of algorithmic verification of PV isolation

Once available online, the automated two-step algorithm could facilitate clinical AF ablation procedures as it is fast, reliable, independent on operator experience, and not requiring pacing maneuvers. Given a 100% sensitivity of the algorithm, the operator is not expected to end an ablation without complete isolation of all PVs. Given a high specificity of 87%, there is a low chance that the operator will continue ablation even though the PV is isolated (13%). As such, on top of facilitation, this algorithm may improve safety and efficacy of AF ablation (by preventing unnecessary ablation in case of isolation and prevent incomplete isolation).

The library of types and parameters can be expanded or re-constructed to be specific for diverse catheters and systems. As such, the automated two-step algorithm can be implemented in various commercially available EAM and recording systems to guide point-by-point manual ablation. Moreover, because the algorithm does not require paired analysis and fixed position of the catheter, it could also be used in PVI guided by single shot devices (Cryoballoon, PVAC, etc.).

Limitations

All electrograms were recorded with a single type of circular mapping catheter. As such, the influence of catheter type, electrode size and spacing was not evaluated. If needed however, this limitation can be overcome by constructing a new catheter-specific library.

The algorithm requires the operator to specify the PV and the hemisphere for each CMC bipole. For fully automated assessment of PVI, bipole position has to be automatically detected by the navigation system.

The library of characteristics and cutoffs were constructed from a dataset of patients without structural heart disease and from one center. Including more data to expand the library can be easily performed and the consequent cutoffs can be adjusted accordingly.

4.5 References

1. Natale A, Raviele A, Arentz T, Calkins H, Chen SA, Haïssaguerre M, Hindricks G, Ho Y, Kuck KH, Marchlinski F, Napolitano C, Packer D, Pappone C, Prystowsky EN, Schilling R, Shah D, Themistoclakis S, Verma A. Venice Chart international consensus document on atrial fibrillation ablation. J Cardiovasc Electrophysiol. 2007;18:560-80.

2. Calkins H, Kuck KH, Cappato R, Brugada J, Camm AJ, Chen SA, et al. 2012 HRS/EHRA/ECAS Expert Consensus Statement on Catheter and Surgical Ablation of

Atrial Fibrillation: recommendations for patient selection, procedural techniques, patient management and follow-up, definitions, endpoints, and research trial design. Europace. 2012;14:528–606.

3. Shah D. Electrophysiological evaluation of pulmonary vein isolation. Europace. 2009;11:1423-33.

4. Duytschaever M, De Meyer G, Acena M, El-Haddad M, De Greef Y, Van Heuverswyn F, Vandekerckhove Y, Tavernier R, Lee G, Kistler P. Lessons from dissociated pulmonary vein potentials: entry block implies exit block. Europace. 2013;15:805-12.

5. Shah D, Haissaguerre M, Jais P, Hocini M, Yamane T, Macle L et al. Left atrial appendage activity masquerading as pulmonary vein potentials. Circulation 2002; 105:2821–5.

6. Shah D, Burri H, Sunthorn H, Gentil-Baron P. Identifying far-field superior vena cava potentials within the right superior pulmonary vein. Heart Rhythm 2006; 3:898–902.

7. Tada H, Oral H, Greenstein R, Pelosi F Jr, Knight BP, Strickberger SA, Morady F. Differentiation of atrial and pulmonary vein potentials recorded circumferentially within pulmonary veins. J Cardiovasc Electrophysiol 2002 ;2:118–123.

8. Hocini M, Shah DC, Jais P, Haissaguerre M, Peng JT, Yamane T, Deisenhofer I, Garrigue S, Clementy J: Concealed left pulmonary vein potentials unmasked by left atrial stimulation. PACE 2000; 23(Pt II):1832-1835.

9. Tada H, Oral H, Wasmer K, Greenstein R, Pelosi F Jr, Knight BP, Strickberger SA, Morady F. Pulmonary vein Isolation: comparison of bipolar and unipolar electrograms at successful and unsuccessful ostial ablation sites. J Cardiovasc Electrophysiol 2002;1:13–19.

CHAPTER 5

Histogram Analysis: A novel method to detect and differentiate fractionated electrograms during atrial fibrillation

Milad El Haddad, MS; Richard Houben, PhD; Tom Claessens, PhD; Rene Tavernier, MD, PhD; Roland Stroobandt, MD, PhD; Mattias Duytschaever, MD, PhD

This original research article was published in the Journal of Cardiovascular Electrophysiology, volume 22, issue 7, pages 781-790 in July 2011

Abstract

Introduction: Complex fractionated atrial electrograms (CFAE) might identify the critical substrate maintaining AF. We developed a method based upon histogram analysis of inter-peak intervals (IPI) to automatically quantify fractionation and differentiate between subtypes of CFAEs.

Methods: Two experts classified 1681 fibrillatory electrograms recorded in 13 patients with persistent AF into three categories (gold standard): normal electrograms; discontinuous CFAEs or continuous CFAEs. Histogram analysis of IPI was performed to calculate the P5, P50, P95 and the mean of IPIs, in addition to the total number of IPI (N_{Total}), and the number of IPI within pre-determined ranges: 10-60ms (N_{Short}), 60-120ms ($N_{Intermediate}$), and >120ms (N_{Long}).

Results: P50 and N_{Long} were higher in the normal electrograms compared to the other two categories ($p<0.001$). $N_{Intermediate}$ was higher in the discontinuous CFAE category compared to the other two categories. P95, mean IPI, N_{Total}, and N_{Short} were all significantly different among the three categories ($p<0.001$) and correlated with the degree of fractionation (r= -0.52, -0.55, 0.68, and 0.67 respectively). ROC curves showed good diagnostic accuracy (area under curve, AUC >0.8) of P50 and N_{Long} to detect normal electrograms. An algorithm using $N_{Intermediate}$ showed good diagnostic accuracy (AUC >0.7) to detect discontinuous CFAEs, whereas P95, mean, N_{Total}, and N_{Short} all revealed high diagnostic accuracy (AUC >0.85) to detect continuous CFAEs. This was confirmed in a prospective data set.

Conclusions: Histogram analysis of inter-peak intervals (IPI) can differentiate between normal electrograms, discontinuous and continuous fractionated electrograms. This method might be used to standardize and optimize ablation strategies in AF.

5.1 Introduction

Pulmonary vein isolation (PVI) is associated with good clinical outcome in patients with paroxysmal atrial fibrillation (AF) and limited heart disease.[1] PVI in patients with structural heart disease and persistent AF is less successful which may be explained by the predominance of a substrate maintaining AF. This substrate is expected to show considerable inter-individual variation.[2,3,4,5,6] Patient-specific substrate ablation could be guided by activation mapping of fibrillatory waves, spectral analysis of electrograms, or identification of complex fractionated atrial electrograms (CFAE).[2,3,7,8] Although CFAEs might point to areas of impaired conduction, their specificity to identify the critical substrate of AF is expected to be limited.[9,10,11] Therefore, indiscriminate ablation of all CFAEs might compromise safety without enhancing efficacy. It has been suggested that differentiation into subtypes of CFAE can enhance the specificity of recognition of the critical substrate.[12] The aim of the present study was to differentiate between normal, discontinuous, and continuous electrograms using an automated time-domain method based upon histogram analysis of inter-peak intervals (IPI). An initial data set was used to define the optimal cutoff values for the investigated parameters based upon a comparison with a visual classification of fibrillatory electrograms performed by experts. These cutoff values were prospectively validated in another independent data set. The histogram analysis of the IPI was compared to commercially available CFAE algorithms. Finally, the spatial distribution of normal electrograms, discontinuous, and continuous CFAEs in the left atrium (LA) was studied.

5.2 Methods

Study subjects

Thirteen patients (60 ±10 years) with symptomatic AF (history of AF 7.4 ± 6.2 years; last AF episode persisting > 1 month) without structural heart disease were studied. LA diameter (PS- LAX, GE Healthcare, Buckinghamshire, UK) was 46 ± 8mm. The study was approved by the ethics committee and informed consent was obtained from all patients.

Ablation procedure

Treatment with antiarrhythmic drugs was stopped one month prior to the procedure (no patient on amiodarone). The procedure was performed under general anesthesia using propofol, cisatracurium, and remifentanil. A decapolar catheter was placed in the coronary sinus (CS). After double transseptal puncture, we introduced: (1) a 14-pole circular mapping catheter (Orbiter PV, Bard Electrophysiology, MA, USA); and (2) an irrigated-tip ablation catheter with a distal 3.5mm tip and three 1mm ring electrodes spaced by 2-5-2mm (Navistar® Thermocool, Biosense-Webster, Diamond Bar, CA, USA). Reconstruction of LA maps was performed during AF using the CARTO® XP system (Biosense-Webster, Diamond Bar, CA, USA). The ablation strategy consisted of circumferential PVI, a complete linear lesion at the mitral isthmus, and LA defractionation.

Mapping protocol

All patients were in AF throughout the procedure. Prior to any RF delivery, high-density LA mapping (120 ± 30 points) was performed. Care was taken to have 1) a stable position of the distal bipole for > 3s, and 2) a homogeneous spatial distribution.

For each acquired point, the CARTO system records its corresponding 2.5s bipolar electrogram that is band-pass filtered (30-400 Hz). After the procedure, all electrograms were extracted from CARTO® XP. Offline analysis was performed with a custom made program developed in Matlab v7.1 (The MathWorks, Inc., Natick, MA, USA).

Category of fractionation: gold standard

Two electrophysiologists - experienced in AF ablation [(MD, RT) > 800 procedures] - independently classified all electrograms according to the visual degree of fractionation: 1) normal, 2) discontinuous fractionated and, 3) continuous fractionated electrograms. Normal electrograms were recordings showing distinct, non-fractionated potentials separated by clear iso-electric windows. Continuous fractionated electrograms were recordings showing continuous perturbation of the baseline with fractionated potentials and no iso-electric windows for the majority of the time. Electrograms that did not meet either criterion were labeled as discontinuous fractionated electrograms. Tracings that could not be interpreted due to the presence of recording artifacts were labeled invalid. Electrograms that were classified differently by the two experts were regarded as mismatch. For the development and calibration of the automated algorithm, all electrograms that either showed mismatch or were classified invalid by both experts were discarded. The degree of fractionation in the matching electrograms was used as the gold standard. Electrograms that showed mismatch were analyzed as a separate group.

Histogram analysis of inter-peak intervals (IPI)

A custom made algorithm was developed to detect positive and negative peaks (i.e. +dV/dt followed by -dV/dt and vice versa) in the electrograms (Figure 1). Noise threshold was set at 0.05mV. All intervals between consecutive peaks (i.e. inter-peak intervals, IPI) were determined automatically (middle tracing). To avoid double counting, all IPI <10ms were discarded. Histogram analysis of the remaining IPI was performed to calculate the 5th percentile (P5), median (P50), 95th percentile (P95), the mean, and the total number (NTotal) of IPIs (lower panel). In addition, the absolute frequency of IPI for different interval ranges was calculated. The optimal limits of these ranges were determined by subtraction of histograms (not shown). The obtained ranges were 10-60ms (short intervals, N_{Short}), 60-120ms (intermediate intervals, $N_{Intermediate}$), and > 120ms (long intervals, N_{Long}).

To determine the optimal cutoff of each parameter, receiver operating characteristic (ROC) curves were constructed by a custom made program (developed in Matlab V7.1) using 2x2 tables of several cutoff values. The point on the ROC curve closest to the upper left corner of the ROC was selected as the optimal cutoff. To prospectively validate the histogram analysis with the cutoff values, the experts classified a new set of electrograms - recorded from another five patients with persistent AF - separately. A binary classification test for each expert classification was used to determine the positive predictive value (PPV), negative predictive value (NPV), sensitivity, specificity, and accuracy of each parameter (with the corresponding cutoff).

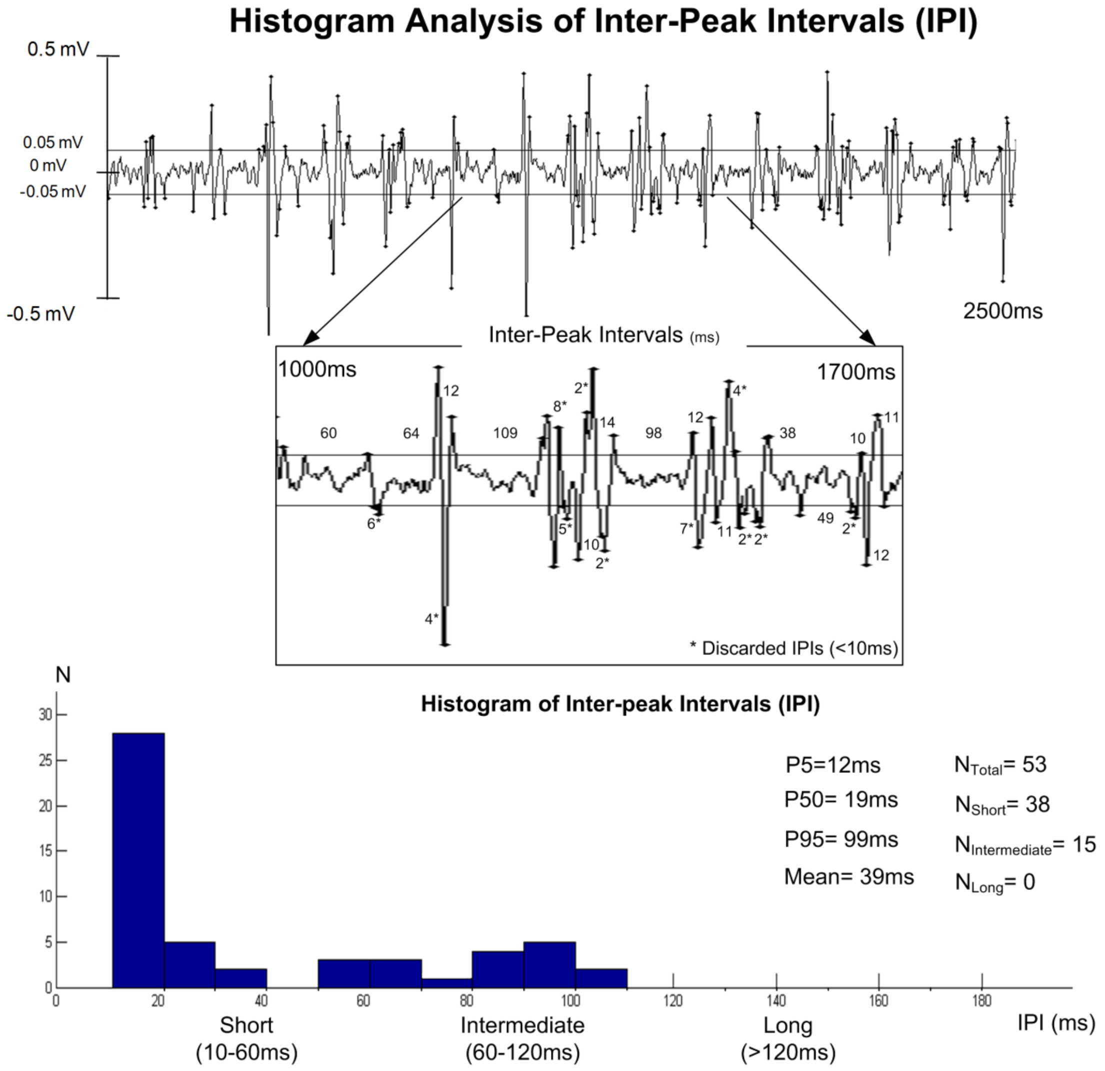

Figure 5-1: *A bipolar fibrillatory electrogram (2.5s) with its corresponding histogram and histogram parameters of inter-peak intervals (IPIs). Middle panel shows a magnified segment (1000ms -1700ms) of the electrogram with all IPI values. Intervals below 10ms are discarded from the analysis. P5 = 5th percentile; P50 = 50th percentile; P95 = 95th percentile;* N_{Short} *= number of IPI between 10ms and 60ms;* $N_{Intermediate}$ *= number of IPI between 60ms and 120ms,* N_{Long} *= number of IPI >120ms.*

To study the temporal stability of the CFAE parameters, a new set of 83 electrograms was used from two patients with persistent AF. At the same catheter position, fibrillatory electrograms were recorded during 2.5 and 10s respectively.

Statistical analysis

For each category, box plots were created for the IPI parameters (P5, P50, P95, mean, N_{Total}, N_{Short}, $N_{Intermediate}$, and N_{Long}) using statistical software SPSS 15.0 (SPSS, Chicago, IL, USA). Student's t-test (for Gaussian distributions) and Wald-Wolfowitz runs test were used to measure the statistical differences between groups. Pearson correlation was used to evaluate the correlation between the degree of fractionation and each IPI parameter. A p value less than 0.05 was considered statistically significant.

Spatial distribution and custom-made 3D mapping software

A 3D mapping software package was developed allowing visualization of each IPI parameter in a color-coded image. The software uses the x-y-z coordinates of the nodes exported from the CARTO. According to the numerical value of an operator-selected IPI parameter, each node is assigned a relative color. Finally, a color-coded 3D map is generated by interpolating the colors of all nodes over the whole surface area. A color bar can be used to manually adjust the displayed colors and threshold according to preset cutoffs. Spatial distribution of the subtypes of fractionation was studied in the first 13 patients.

Direct interval analysis

Because histogram analysis of IPI is an interval based method, direct interval analysis was performed as well. All peaks above 0.05 mV were detected and all inter peak intervals were directly counted without the refractory period of 10ms. Then, for each possible interval range (i.e. 0-10ms, 0-20ms, etc.) the absolute number of intervals was calculated and the diagnostic accuracy was compared to the gold standard.

Histogram analysis versus commercially available software

A commercially available software (NavX EnSite system, St Jude Medical, St Paul, MN, USA) which calculates the mean interval of complex fractionated electrograms (CFE) has been recently validated for the ablation of AF (STAR AF).[13] Electrograms having CFE-mean <120 ms are identified as CFAE positive. The CFAE software in the Carto system (Biosense-Webster, Diamond Bar, CA, USA) uses an algorithm to count the number of intervals (interval confidence level, ICL) within an operator-specified time window. Most studies use the default time window of 70-120ms with an ICL cutoff ≥ 5 to identify CFAEs.[23,27] We developed an offline algorithm (in Matlab) that performs an identical calculation of the CFE-mean and the ICL 70-120 and compared the results with the histogram analysis of IPI.

5.3 Results

Classification by experts – gold standard

Out of 1681 fibrillatory electrograms, 333 (20%) electrograms showed mismatch whereas 77 (5%) were classified invalid by both experts. The remaining 1271 were classified identically by both experts: 1) normal electrograms (207), 2) discontinuous fractionated electrograms (586), and 3) continuous fractionated electrograms (478). To minimize variability, only those 1271 electrograms and their classification were used as gold standard.

Percentiles and mean of inter-peak intervals (IPI)

Electrograms (normal, discontinuous, and continuous CFAE) with their corresponding IPI histogram are shown in Figure 2. P5 was comparable among the three electrograms (12ms, 12ms, and 11ms). P50 (68ms) was higher for normal electrograms compared to the two fractionated electrograms (19ms, and 17ms). With increasing degree of fractionation, P95 and mean IPI decreased (156ms, 99ms, 43ms and 80ms, 39ms, 20ms). Box plots are given in Figure 3 (upper panels). The P5 IPI was comparable between the categories (p= 0.991) and did not correlate with the degree of fractionation (r=-0.13, p<0.001). The P50 IPI was significantly higher for normal electrograms (p<0.001), but not different between the discontinuous CFAEs and continuous CFAEs. The P95 and mean IPI showed a significant linear correlation with the degree of fractionation (r = -0.52 and -0.55 respectively, p<0.001), with a significant difference in between the categories (p<0.001).

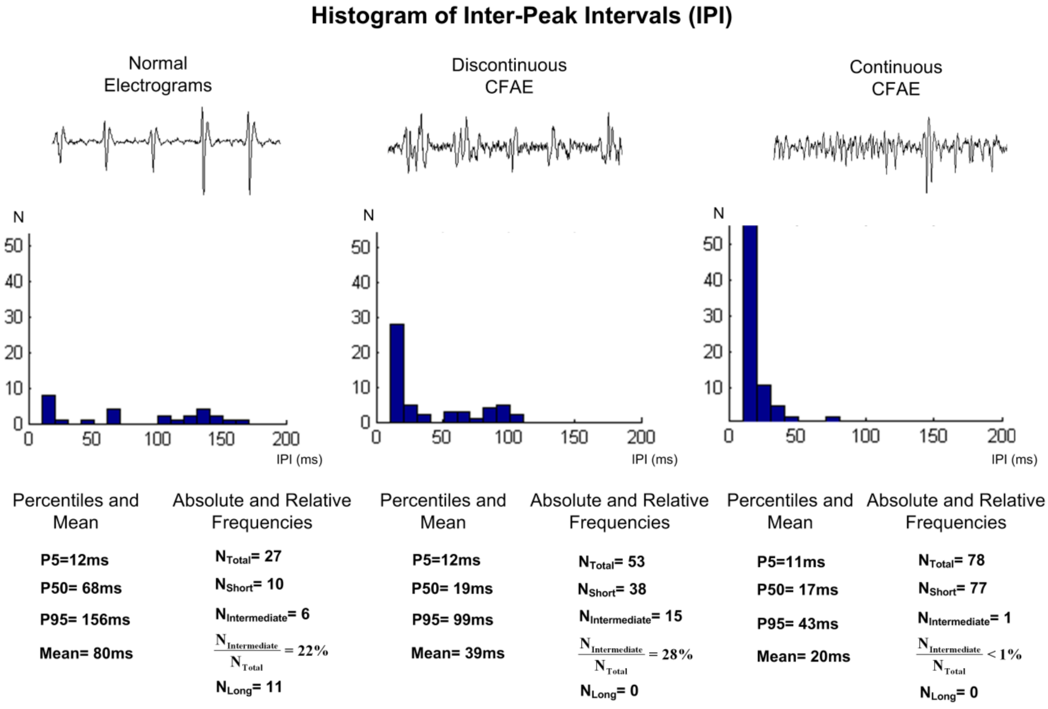

Figure 5-2: *Three representative electrograms (top) from the different degrees of fractionation (normal electrogram, discontinuous CFAE, and continuous CFAE) and their corresponding histograms of inter-peak intervals (IPI). Below each histogram the corresponding values of percentiles and mean, in addition to the values of the absolute and relative frequencies. P5 = 5th percentile; P50 = 50th percentile; P95 = 95th percentile; N_{Total} = total number of IPI, N_{Short} = number of IPI between 10 and 60ms; $N_{Intermediate}$ = number of IPI between 60 and 120ms, N_{Long} = number of IPI >120ms.*

Absolute and relative frequencies of inter-peak intervals (IPI)

With increasing degree of fractionation (Figure 2), there was an increasing value of the total number of IPI (N_{Total}= 27, 53, and 78). In addition, the histograms became skewed to the left with the normal electrogram being characterized by more long intervals, the discontinuous CFAE by more intermediate intervals, and the continuous CFAE by more short intervals. With increasing degree of fractionation (Figure 2), the number of short IPI increased (N_{Short}= 10, 38, and 77). The number of intermediate IPI was higher for the discontinuous fractionated electrogram compared to the other two electrograms ($N_{Intermediate}$=6, 15, and 1). To correct for the difference in the total number of IPI, the relative frequency $N_{Intermediate}/N_{Total}$ was calculated. This resulted in a distinct differentiation between the discontinuous and continuous CFAEs (28% and <1% respectively). The number of long IPI was higher for the normal electrogram compared to the two other fractionated electrograms (N_{Long}=11, 0, and 0). Box plots are given in Figure 3 (lower panels). N_{Total} and N_{Short} showed significant difference among all categories ($p<0.001$), with a significant linear correlation with respect to the degree of fractionation ($r=0.68$ and 0.67 respectively, $p<0.001$). $N_{Intermediate}$ was higher at the discontinuous CFAEs category with a significant difference from the two other categories ($p<0.001$), but not significantly different between the normal electrograms and the continuous CFAEs categories ($p=0.85$). The absolute difference between the discontinuous and continuous CFAEs was enhanced by using the relative frequency $N_{Intermediate}/N_{Total}$ ($p<0.001$, not shown). N_{Long} showed a significant difference among all categories (Student’s t-test $p<0.001$) with a significant linear correlation with respect to the degree of fractionation ($r=-0.60$, $p<0.001$).

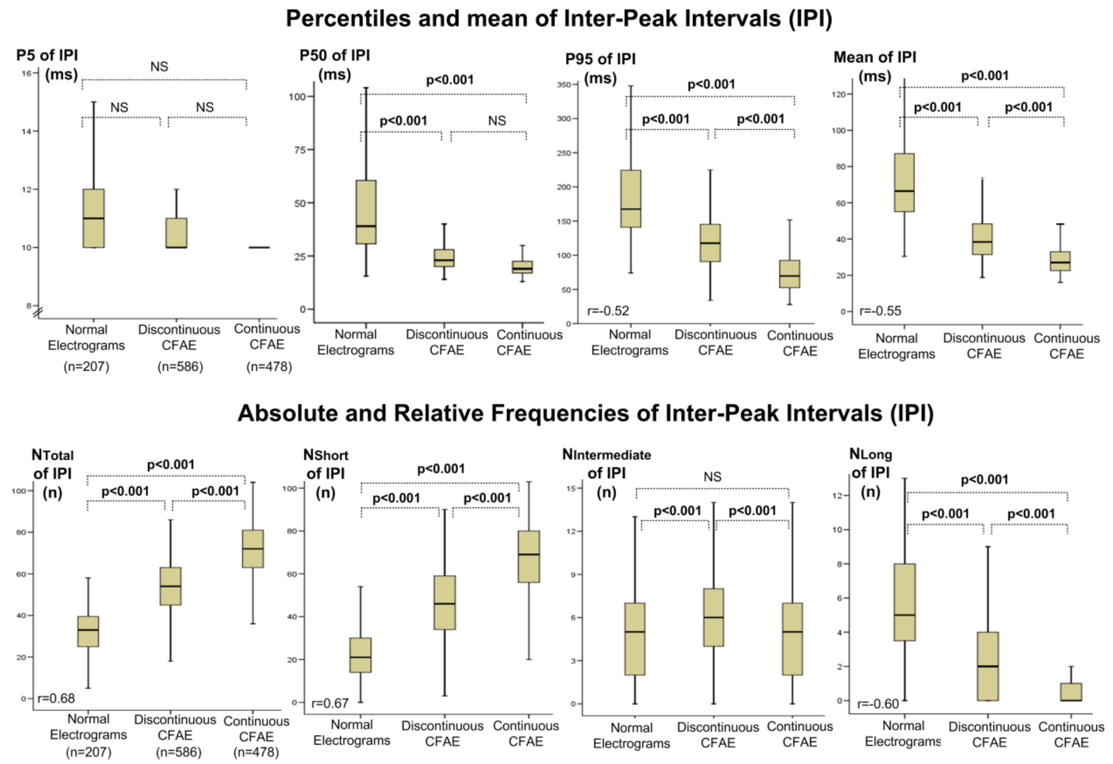

Figure 5-3: *Box plots displaying minimum, first quartile, median, third quartile, and maximum of the parameters of the inter-peak intervals (IPI) histogram with respect to the fractionation categories. See text for explanation. P5 is the 5th percentile; P50 is the 50th percentile; P95 is the 95th percentile; NS is non-significant;* N_{Total} *= total number of IPI,* N_{Short} *= number of IPI between 10 and 60ms;* $N_{Intermediate}$ *= number of IPI between 60 and 120ms,* N_{Long} *= number of IPI >120ms. NS = non-significant.*

Classification of electrograms showing visual mismatch

Mismatch in visual classification was seen in 333 electrograms. Expert one classified 65 electrograms as normal while expert two classified them as discontinuous (n=50) or invalid (n=15). Out of 176 discontinuous CFAEs (expert one), expert two classified 40 as discontinuous and 116 as continuous CFAEs (20 invalid). Out of 75 normal electrograms, expert 2 classified 74 as discontinuous CFAEs (1 invalid). Finally, expert one classified 17 electrograms as invalid. In conclusion, mismatch between experts never exceeded more than one class. Histogram analysis of mismatching electrograms revealed nominal values at the transition between two neighboring classes.

Diagnostic accuracy of IPI parameters to identify normal, discontinuous, and continuous fractionated electrograms

ROC curves of P50 and NLong revealed good diagnostic accuracy (AUC=0.88 and 0.86) to detect normal electrograms at cutoffs of >30ms and >3 respectively. At these cutoffs the sensitivity was 80% and 75% with corresponding specificity of 79% and 82% (figure 4, left panel). To detect discontinuous CFAEs we employed a two-step algorithm. This algorithm used first P50 (>30ms) to filter out normal electrograms, then NIntermediate/NTotal (>10%) was used as a second step to distinguish discontinuous CFAEs from the remaining electrograms.

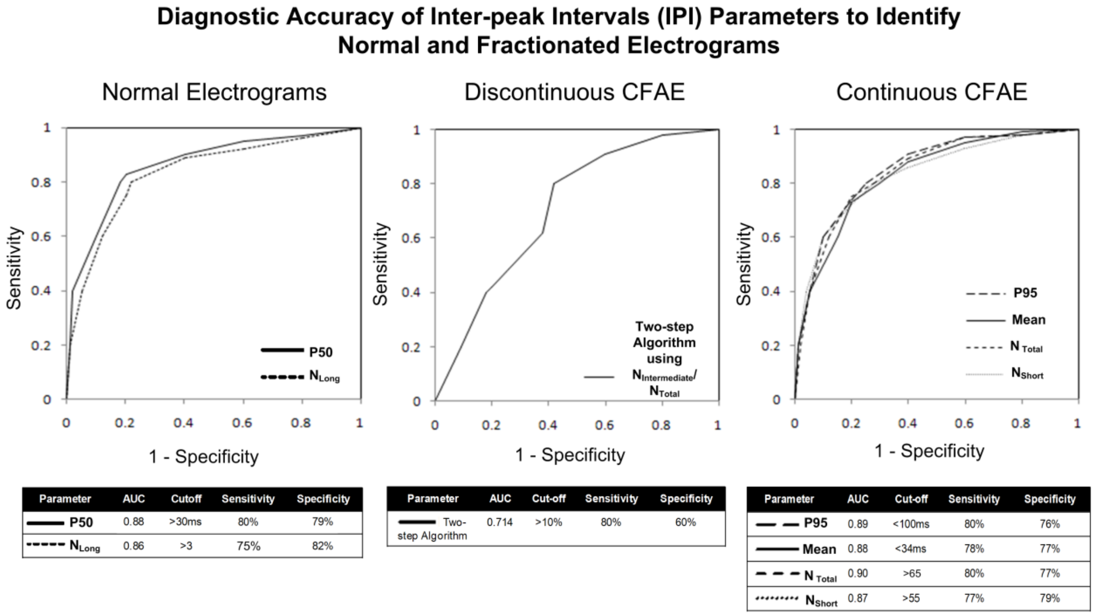

Parameter	AUC	Cutoff	Sensitivity	Specificity
P50	0.88	>30ms	80%	79%
N_{Long}	0.86	>3	75%	82%

Parameter	AUC	Cut-off	Sensitivity	Specificity
Two-step Algorithm	0.714	>10%	80%	60%

Parameter	AUC	Cut-off	Sensitivity	Specificity
P95	0.89	<100ms	80%	76%
Mean	0.88	<34ms	78%	77%
N_{Total}	0.90	>65	80%	77%
N_{Short}	0.87	>55	77%	79%

Figure 5-4: *Receiver operating characteristic (ROC) curves of inter-peak intervals (IPI) histogram parameters to identify normal electrograms, discontinuous, and continuous CFAEs. Left panel, ROC curves of* N_{Long} *and P50 to identify normal electrograms. Middle panel, ROC curve of the two-step algorithm of P50 and* $N_{Intermediate}/N_{Total}$ *to identify discontinuous CFAEs. Right panel, ROC curves of P95, mean IPI,* N_{Total}*, and* N_{Short} *to identify continuous CFAEs. Below each ROC curve a table showing the corresponding area under curve (AUC), optimal cutoff (defined as the closest point on the curve to the upper left corner), sensitivity, and specificity. P50 = 50*th *percentile; P95 = 95*th *percentile;* N_{Total} *= total number of IPI,* N_{Short} *= number of IPI between 10 and 60ms;* $N_{Intermediate}$ *= number of IPI between 60 and 120ms,* N_{Long} *= number of IPI >120ms.*

The AUC of this two-step algorithm was 0.71 with a sensitivity of 80% and a specificity of 60% (middle panel). ROC curves of P95, mean, N_{Total}, and N_{Short} revealed good accuracy (AUC>0.85) to detect continuous CFAEs at cutoffs of <100ms, <34ms, >65, and >55 respectively (figure 4, right panel). At these cutoffs, sensitivity was 80%, 78%, 80%, and 77% with corresponding specificity of 76%, 77%, 77%, and 79% respectively.

Prospective validation of histogram analysis of IPI

Data are given in Table 1. A binary classification test revealed good PPV, NPV, sensitivity, specificity, and accuracy of each parameter to detect normal (P50 and NLong), discontinuous (two-step algorithm using $N_{Intermediate}/N_{Total}$), and continuous (P95, mean, N_{Total}, and N_{Short}) CFAEs for each expert.

Table 5.1: *Prospective validation of histogram analysis of IPI*

E1 | E2	**Histogram Analysis of IPI ***						
	P50	**N_{Long}**	**Two-step algorithm**	**P95**	**Mean**	**N_{Total}**	**N_{Short}**
PPV (%)	25 | 28	16 | 21	67 | 59	73 | 72	74 | 72	74 | 73	74 | 73
NPV (%)	98 | 97	96 | 96	62 |70	82 | 76	81 | 76	78 | 74	79 | 74
Sensitivity (%)	87 | 77	67 | 71	83 | 85	64 | 62	62 | 58	50 | 49	52 | 51
Specificity (%)	76 | 78	68 | 70	41 | 38	77 | 78	86 | 81	86 | 88	85 | 86
Accuracy	77 | 78	68 | 70	66 | 62	73 | 72	74 | 72	74 | 73	74 | 73

** Cutoffs of IPI parameters used were determined by ROC curves (described in text).*

CFAE is complex fractionated atrial electrograms, E1 = expert 1, E2= expert 2, IPI is inter-peak intervals, P50 = 50th percentile, P95 = 95th percentile, N_{Total} = total number of IPI, N_{Short} = number of IPI between 10 and 60ms, N_{Long} = number of IPI >120ms, PPV= positive predictive value, NPV= negative predictive value.

Spatial distribution of normal, discontinuous, and continuous CFAEs

Representative color-coded maps of IPI parameters to detect the three categories of fractionation are given in Figure 5 (left panel). In this patient, NLong displayed normal electrograms in the anterior and lateral wall, LA appendage (LAA), part of the posterior wall and PV ostia (red zones). Discontinuous CFAEs (detected by $N_{Intermediate}/N_{Total}$) were found at the posterior wall of the LA and the LAA, whereas N_{Total} displayed continuous CFAEs at the septum (red zone). To calculate the spatial distribution of the subtypes of electrograms for all patients, the LA was divided into six zones: 1) roof, 2) septum, 3) anterior and lateral wall, LAA, 4) posterior wall, 5) inferior wall and 6) PV ostia (Figure 5, top). For each zone the percentage of normal electrograms, discontinuous CFAEs, and continuous CFAEs was determined using the experts' diagnosis and the corresponding IPI parameter(s) (Figure 5, table). For normal electrograms, P50 and NLong showed consistent results compared to the experts' classification. In all patients, the anterior and lateral wall, LAA (zone 3), the posterior wall (zone 4) in addition to the PV ostia (zone 6), revealed the highest prevalence of normal electrograms irrespective of the parameter. The two-step algorithm as well, showed consistent results with the experts' classification to detect discontinuous CFAEs. The highest prevalence of discontinuous CFAEs was observed in both the posterior wall (ranging from 54±5% to 58±7%; $p<0.001$) and inferior wall (ranging from 47±4 to 55±4%; $p<0.001$). All automated IPI parameters to detect continuous CFAEs showed consistent results compared to the experts' classification. The septum revealed the highest prevalence of continuous CFAEs, irrespective of the parameter (ranging from 58±6% to 70±5%; $p<0.01$).

Temporal stability of IPI parameters

Histogram analysis performed on 10s recordings revealed IPI values comparable to values extracted from 2.5s electrograms (R ranging from 0.54 to 0.88, $p<0.05$).

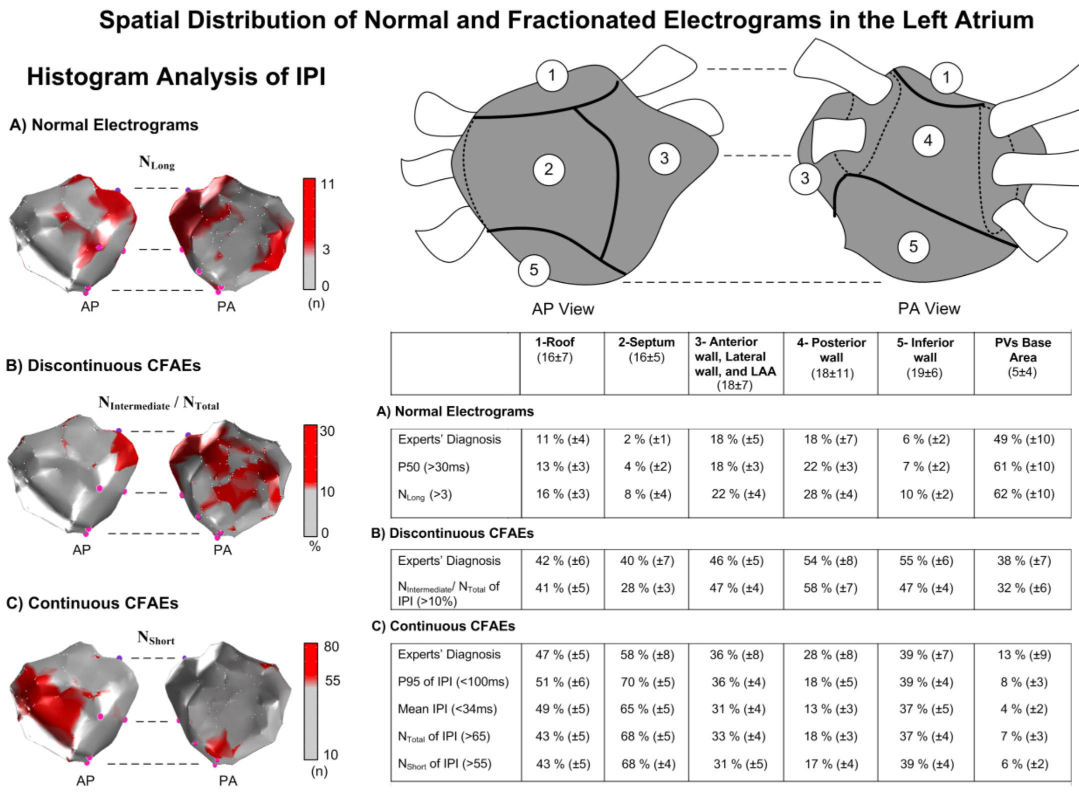

	1-Roof (16±7)	**2-Septum** (16±5)	**3- Anterior wall, Lateral wall, and LAA** (18±7)	**4- Posterior wall** (18±11)	**5- Inferior wall** (19±6)	**PVs Base Area** (5±4)
A) Normal Electrograms						
Experts' Diagnosis	11 % (±4)	2 % (±1)	18 % (±5)	18 % (±7)	6 % (±2)	49 % (±10)
P50 (>30ms)	13 % (±3)	4 % (±2)	18 % (±3)	22 % (±3)	7 % (±2)	61 % (±10)
N_{Long} (>3)	16 % (±3)	8 % (±4)	22 % (±4)	28 % (±4)	10 % (±2)	62 % (±10)
B) Discontinuous CFAEs						
Experts' Diagnosis	42 % (±6)	40 % (±7)	46 % (±5)	54 % (±8)	55 % (±6)	38 % (±7)
$N_{Intermediate}$/ N_{Total} of IPI (>10%)	41 % (±5)	28 % (±3)	47 % (±4)	58 % (±7)	47 % (±4)	32 % (±6)
C) Continuous CFAEs						
Experts' Diagnosis	47 % (±5)	58 % (±8)	36 % (±8)	28 % (±8)	39 % (±7)	13 % (±9)
P95 of IPI (<100ms)	51 % (±6)	70 % (±5)	36 % (±4)	18 % (±5)	39 % (±4)	8 % (±3)
Mean IPI (<34ms)	49 % (±5)	65 % (±5)	31 % (±4)	13 % (±3)	37 % (±5)	4 % (±2)
N_{Total} of IPI (>65)	43 % (±5)	68 % (±5)	33 % (±4)	18 % (±3)	37 % (±4)	7 % (±3)
N_{Short} of IPI (>55)	43 % (±5)	68 % (±4)	31 % (±5)	17 % (±4)	39 % (±4)	6 % (±2)

Figure 5-5: *Left panel, representative custom-made color-coded maps of the left atrium which display the distribution of normal electrograms, discontinuous, and continuous CFAEs using* N_{Long}, $N_{Intermediate}/N_{Total}$, *and* N_{Short} *respectively (red zones). The color bar was manually adjusted for each parameter according to the corresponding cutoff (>3, >10%, and >55 respectively). Right upper panel, schematic drawing of the LA (left: AP view, right: PA view) with the 6 zones of interest: 1) roof, 2) septum, 3) left atrial appendage, anterior and lateral wall, 4) posterior wall, 5) inferior wall, 6) PV ostia. Distribution of CFAEs detected by each parameter with its specific cutoff is given in the table. (see text for explanation).*

Direct interval analysis

Direct interval counting showed that the number of intervals within 10-60ms, 10-70ms, up to 10-150ms were the best ranges to detect continuous CFAEs (AUC from

0.850 to 0.855). Intervals within the ranges of 70-120ms up to 70-150ms and 80-120ms up to 80-150ms were the best to detect discontinuous CFAEs with AUC ranging from 0.641 to 0.646.

Table 5.2: *Histogram analysis of IPI versus EnSite "CFE-Mean" and CARTO XP "CFAE-ICL"*

Gold Standard	**Histogram Analysis of IPI***	**EnSite NavX (CFAE positive if CFE-mean < 120ms)$^{+}$**	**CARTO XP (CFAE positive if ICL 70-120 ≥ 5)^**
Matching classification (n)	**Correctly classified n (%)**	**Correctly classified n (%)**	**Correctly classified n (%)**
Normal (207)	165, 155 (80, 75%)	90 (44%)	90 (44%)
Discontinuous CFAEs (586)	468 (80%)	1010 (95%)	516 (49%)
Continuous CFAEs (478)	381, 373, 383, 369 (80, 78, 80, 77%)		

** Parameters of histogram analysis of IPI used in this table are P50, two-step algorithm using $N_{Intermediate}$, and N_{Total} to classify normal, discontinuous, and continuous CFAEs respectively;*

$^{+}$ *Electrograms having CFE-Mean < 120ms were considered CFE positive by EnSite.*

^ Electrograms having ICL score ≥ 5 were considered CFE positive by CARTO.

CFE = complex fractionated electrograms, ICL= interval confidence level, IPI = inter-peak intervals.

Histogram analysis versus standard use of commercially available CFE software

Results are given in table 2. Histogram analysis of IPI can discriminate up to 80% of normal electrograms, discontinuous and continuous CFAEs. CFE-mean (Ensite NavX) was able to detect only 44% of normal electrograms and 95% of CFAEs but without differentiation. Using the ICL 70-120 criterion (Carto XP), of all normal electrograms 44% were classified correctly (cutoff<5), whereas of all CFAEs, 49% were classified correctly without differentiation (cutoff ≥5).

5.4 Discussion

Main findings

We developed an automated method based on histogram analysis of inter-peak intervals (IPI) to differentiate between normal, discontinuous and continuous fractionated electrograms during AF. Different parameters with their corresponding cutoffs were calculated and validated in a prospective data set. Spatial distribution of subtypes of fractionated electrograms was visualized on custom-made 3D color-coded maps. Finally, we showed by comparison to commercially available algorithms (CFE-Mean, STAR AF study)[13] that histogram analysis of IPI enables detection of clinically relevant fractionated electrograms, with the advantage of differentiation into subtypes of fractionation.

Characteristics of CFAEs: active versus passive and continuous versus discontinuous

Although fractionated electrograms may point to regions critical for AF (i.e. active CFAEs),[7,9,14,15,16,17,18] CFAEs might also be present in regions of structural and anatomical heterogeneity not fundamental for AF (i.e. passive CFAEs). Because both active and passive CFAEs can co-exist within the atria, it seems essential to develop methods enabling more accurate discrimination. Activation mapping of fibrillatory waves might indicate the critical regions maintaining AF.[19] It is unknown whether electrogram morphology might enable differentiation between active and passive CFAEs. Both Lin et al.[20] (in a canine model of AF) and Takahashi et al.[12] (in patients with AF), showed that ablation-induced modification of AF preferentially occurred at sites exhibiting electrograms with continuous rather than discontinuous activity.

These studies suggest that differentiation of discontinuous and continuous CFAE are needed to improve clinical outcome and safety of CFAE ablation.[12,20,21,22]

Visual detection and differentiation of fractionated electrograms

Prior ablation studies on clinical outcome after either stand-alone defractionation or defractionation following PVI show divergent results.[2,21,22,23,24] Discrepancy in results might be due to different visual interpretation of CFAEs. Despite the widespread use of Nademanee et al.[2] criteria of CFAEs, their definition does not allow differentiation between the subtypes of CFAEs.

Visual classification of fibrillatory electrograms in prior studies showed moderate consistency among the experts (60-65%).[25,26] In the present study, agreement in classification between the two experts was only for 75% of the fibrillatory electrograms. The above observations emphasize that visual assessment of the degree of fractionation in electrograms is a subjective method and that standardized methods to quantify and differentiate fibrillatory electrograms are needed.

CFAE differentiation and the gold standard in AF ablation

The optimal gold standard in AF ablation is a criterion that identifies an ablation target that results in a more effective AF ablation (i.e. ablation induced termination of AF or a better clinical outcome). However, AF termination occurs rarely and a cumulative effect of prior ablations can never be excluded. Long-term clinical outcome can only be assessed by future randomized trials comparing different ablation sequences and targets. In view of these limitations and the availability of data supporting the role of CFAE in the maintenance of AF, visual classification of CFAE is at this moment in time a valid intermediate step towards the development of an optimal gold standard. To minimize the variability in the gold standard, we used only those electrograms with matching classification. The validity of this chosen gold standard was supported by the positive prospective validation of the histogram method which was done for each expert separately.

Automated histogram analysis for the detection and differentiation of CFAE

Histogram analysis of IPI was introduced as a novel method to detect and differentiate fractionated atrial electrograms. The temporal stability of the measurements indicates that stable 2.5s recordings are enough to insure consistent results with this method. Different histogram parameters (50th percentile, N_{Long}, $N_{Intermediate}/N_{Total}$, 95th percentile, mean IPI, N_{Total}, and N_{Short}) can be used independently to quantify automatically the degree of complexity (normal, discontinuous, and continuous CFAEs) in bipolar electrograms with high sensitivity and specificity.

Histogram analysis is strictly based upon analysis of intervals. As such, our findings imply that direct interval counters can differentiate between continuous and discontinuous electrograms as well (see below, commercially available systems). If continuous CFAEs are the most useful targets for CFAE ablation, then interval counting alone should be sufficient. However, three arguments underscore the value of using the intermediate step of histogram analysis of all intervals: (1) whereas normal and continuous CFAEs can be detected by direct interval counters (N_{Short}, N_{Long}, N_{Total}), our data suggest that for discontinuous CFAEs detection, histogram analysis is superior since the 50th percentile is needed in the two-step algorithm; (2) histogram parameters (percentiles and mean parameters) have the advantage of being not affected by the duration of the bipolar recording compared to the direct interval counters in which the nominal value is dependent on the recording time; and (3) the conclusion that direct interval counters could be sufficient is a direct implication of the present study and not vice versa.

Indirect and direct validity of the automated histogram analysis

Even though histogram analysis of IPI increases the accuracy and reproducibility to detect discontinuous and continuous CFAEs, this study did not investigate the direct validity of this method to identify the critical substrate maintaining AF. The ultimate goal of research on CFAE is to identify those electrograms worthwhile to be ablated. This could be reflected in a prolongation of AF cycle length, AF termination or an improved clinical outcome during ablation. This requires as a first step an objective and algorithmic description of fibrillatory electrograms. In contrast to prior studies on CFAE research, this step was performed and described in the present manuscript. Indirect clinical validity of our approach is already reflected in the results of the STAR AF trial. In this study, PVI in combination with CFAE ablation was superior to PVI alone in patients with long standing persistent AF. CFAEs were identified objectively using commercially available software. Our histogram based analysis not only detects these electrograms but has the advantage of differentiating these electrograms into subtypes of fractionation.

In our opinion, histogram analysis of IPI can be used as a research tool to compare different ablation strategies, to further decipher fractionated electrograms, link them to the underlying substrate, and to study the effects of anti-arrhythmic drugs on subtypes of fractionation. Moreover, we showed that histogram analysis of IPI with color-coded mapping could be easily implemented in commercial systems and used as online CFAE software during ablation procedures.

How to interpret and optimize currently available CFAEs software?

The EnSite NavX system uses the “CFE-mean” extension to detect fractionation. Electrograms with a CFE mean <120ms are considered CFAE positive.[13,25,28] Based upon our findings, this setting detects some normal electrograms and the majority of fractionated electrograms without discrimination between discontinuous and continuous CFAEs (Table2) . A cutoff of <70ms would make the method more sensitive for the detection of continuous fractionation. Discarding the refractory window (i.e. refractory setting set to 10ms) would make it sensitive to detect only continuous CFAEs (CFE mean < 35ms).

The CARTO system uses the ICL score to detect fractionation. Most studies use the default time window of 70-120ms with ICL cutoff ≥5.[23,27] Based upon our findings, this setting detects only a minority of the CFAEs of whom the majority are discontinuous. The combination of a time window 60-120ms with ICL ≥ 4 makes the algorithm more sensitive to detect discontinuous CFAEs, whereas adjusting the time window to 10-60ms with an ICL>55 allows detection of continuous CFAEs.

Study limitations

Visual assessment of fibrillatory electrograms was used as a gold standard. Histogram analysis of fibrillatory electrograms assumes temporal stability of the substrate over relatively long periods of time. Bipolar electrograms may be greatly influenced by electrode size, inter-electrode spacing, and catheter orientation. Since the proposed method was investigated with a single type of catheter, the universality of the method in the clinical arena was not tested. Using a fixed low-voltage threshold to detect peaks, potentials reflecting true local activation may be missed. An adjustable noise threshold or measures to improve the signal to noise ratio could further improve accurate detection of peaks. Finally, the effect of ablation of the different subtypes of fractionated electrograms has not been evaluated yet.

5.5 References

1. European Heart Rhythm Association (EHRA), European Cardiac Arrhythmia Scoiety (ECAS), American College of Cardiology (ACC), American Heart Association (AHA), Society of Thoracic Surgeons (STS); Calkins H, Brugada J, Packer DL, Cappato R, Chen SA, Crijns HJ, Damiano RJ Jr, Davies DW, Haines DE, Haissaguerre M, Iesaka Y, Jackman W, Jais P, Kottkamp H, Kuck KH, Lindsay BD, Marchlinski FE, McCarthy PM, Mont JL, Morady F, Nademanee K, Natale A, Pappone C, Prystowsky E, Raviele A, Ruskin JN, Shemin RJ : HRS/EHRA/ECAS expert Consensus Statement on catheter and surgical ablation of atrial fibrillation: Recommendations for personnel, policy, procedures and follow-up. A report of the Heart Rhythm Society (HRS) Task Force on catheter and surgical ablation of atrial fibrillation. Heart Rhythm 2009; 6:1-148.

2. Nademanee K, McKenzie J, Kosar E, Schwab M, Sunsaneewitayakul B, Vasavakul T, Khunnawat C, Ngarmukos T: A new approach for catheter ablation of atrial fibrillation: Mapping of the electrophysiologic substrate. J Am Coll Cardiol 2004; 43:2044-2053.

3. Konings KT, Smeets JL, Penn OC, Wellens HJ, Allessie MA: Configuration of unipolar atrial electrograms during electrical induced atrial fibrillation in humans. Circulation 1997; 95:1231-1241.

4. Rostock T, Rotter M, Sanders P, Takahashi Y, Jaïs P, Hocini M, Hsu LF, Sacher F, Clémenty J, Haïssaguerre M: High density activation mapping of fractionated electrograms in the atria of patients with paroxysmal atrial fibrillation. Heart Rhythm 2006; 3:27-34.

5. Papageorgiou P, Monahan K, Boyle NG, Seifert MJ, Beswick P, Zebede J, Epstein LM, Josephson ME: Site-dependent intra-atrial conduction delay: Relationship to initiation of atrial fibrillation. Circulation 1996; 94:384-389.

6. Gaita F, Calò L, Riccardi R, Garberoglio L, Scaglione M, Licciardello G, Coda L, Di Donna P, Bocchiardo M, Caponi D, Antolini R, Orzan F, Trevi GP: Different patterns of atrial activation in idiopathic atrial fibrillation: Simultaneous multisite atrial mapping in patients with paroxysmal and chronic atrial fibrillation. J Am Coll Cardiol 2001; 37:534-541.

7. Konings K, Kirchhof C, Smeets J, Wellens H, Penn O, Allessie M: High-density mapping of electrically induced atrial fibrillation in humans. Circulation 1994; 89:1665-1680.

8. Gojraty S, Lavi N, Valles E, Kim SJ, Michele J, Gerstenfeld EP: Dominant frequency mapping of atrial fibrillation: comparison of contact and noncontact approaches. J Cardiovasc Electrophysiol 2009; 20:997-1004.

9. Haïssaguerre M, Sanders P, Hocini M, Takahashi Y, Rotter M, Sacher F, Rostock T, Hsu LF, Bordachar P, Reuter S, Roudaut R, Clémenty J, Jaïs P: Catheter ablation of long-lasting persistent atrial fibrillation: Critical structures for termination. J Cardiovasc Electrophysiol 2005; 16:1125-1137.

10. Calò L, Lamberti F, Loricchio ML, De Ruvo E, Colivicchi F, Bianconi L, Pandozi C, Santini M: Left atrial ablation versus biatrial ablation for persistent and permanent atrial fibrillation: A prospective and randomized study. J Am Coll Cardiol 2006; 47:2504-2512.

11. de Bakker JM, Wittkampf FH: The pathophysiologic basis of fractionated and complex electrograms and the impact of recording techniques on their detection and interpretation. Circ Arrhythm Electrophysiol 2010; 3:204-213.

12. Takahashi Y, O'Neill MD, Hocini M, Dubois R, Matsuo S, Knecht S, Mahapatra S, Lim KT, Jaïs P, Jonsson A, Sacher F, Sanders P, Rostock T, Bordachar P, Clémenty J, Klein GJ, Haïssaguerre M: Characterization of electrograms associated with termination of chronic atrial fibrillation by catheter ablation. J Am Coll Cardiol 2008; 51:1003-1010.

13. Verma A, Mantovan R, Macle L, De Martino G, Chen J, Morillo CA, Novak P, Calzolari V, Guerra PG, Nair G, Torrecilla EG, Khaykin Y.: Substrate and Trigger Ablation for Reduction of Atrial Fibrillation (STAR AF): a randomized, multicentre, international trial. Eur Heart J 2010; 31:1344-1356.

14. Spach MS, Dolber PC: Relating extracellular potentials and their derivatives to anisotropic propagation at microscopic level in human cardiac muscle: evidence for electrical uncoupling of side-to-side fiber connections with increasing age. Circulation Research 1986; 58:356–371.

15. Jacquemet V, Henriquez CS: Genesis of complex fractionated atrial electrograms in zones of slow conduction: a computer model of microfibrosis. Heart Rhythm 2009; 6:803-810.

16. Kalifa J, Tanaka K, Zaitsev A, Warren M, Vaidyanathan R, Auerbach D, Pandit S, Vikstrom KL, Ploutz-Snyder R, Talkachou A, Atienza F, Guiraudon G, Jalife J, Berenfeld O: Mechanisms of wave fractionation at boundaries of high-frequency excitation in the posterior left atrium of the isolated sheep heart during atrial fibrillation. Circulation 2006; 113:626–633.

17. Lin J, Scherlag BJ, Zhou J, Lu Z, Patterson E, Jackman WM, Lazzara R, Po SS: Autonomic mechanism to explain complex fractionated atrial electrograms (CFAE). J Cardiovasc Electrophysiol 2007; 18:1197-1205.

18. Yamabe H, Morihisa K, Tanaka Y, Uemura T, Enomoto K, Kawano H, Ogawa H: Mechanisms of the maintenance of atrial fibrillation: role of the complex fractionated atrial electrogram assessed by noncontact mapping. Heart Rhythm 2009; 6:1120-1128.

19. Houben RP, de Groot NM, Lindemans FW, Allessie MA: Automatic mapping of human atrial fibrillation by template matching. Heart Rhythm 2006; 3:1221-1229.

20. Lin J, Scherlag BJ, Zhou J, Lu Z, Patterson E, Jackman WM, Lazzara R, Po SS: Autonomic mechanism to explain complex fractionated atrial electrograms (CFAE). J Cardiovasc Electrophysiol 2007; 18:1197-1205

21. Elayi CS, Verma A, Di Biase L, Ching CK, Patel D, Barrett C, Martin D, Rong B, Fahmy TS, Khaykin Y, Hongo R, Hao S, Pelargonio G, Dello Russo A, Casella M, Santarelli P, Potenza D, Fanelli R, Massaro R, Arruda M, Schweikert RA, Natale A: Ablation for longstanding permanent atrial fibrillation: results from a randomized study comparing three different strategies. Heart Rhythm 2008; 5:1665-1666.

22. Tada H, Yoshida K, Chugh A, Boonyapisit W, Crawford T, Sarrazin JF, Kuhne M, Chalfoun N, Wells D, Dey S, Veerareddy S, Billakanty S, Wong WS, Kalra D, Kfahagi A, Good E, Jongnarangsin K, Pelosi F Jr, Bogun F, Morady F, Oral H: Prevalence and characteristics of continuous electrical activity in patients with paroxysmal and persistent atrial fibrillation. J Cardiovasc Electrophysiol 2008; 19:606-612.

23. Scherr D, Dalal D, Cheema A, Cheng A, Henrikson CA, Spragg D, Marine JE, Berger RD, Calkins H, Dong J: Automated detection and characterization of complex fractionated atrial electrograms in human left atrium during atrial fibrillation. Heart Rhythm 2007; 4:1013-1020.

24. Wu J, Estner H, Luik A, Ucer E, Reents T, Pflaumer A, Zrenner B, Hessling G, Deisenhofer I: Automatic 3D mapping of complex fractionated atrial electrograms (CFAE) in patients with paroxysmal and persistent atrial fibrillation. J Cardiovasc Electrophysiol 2008; 19:897-903.

25. Ng J, Borodyanskiy AI, Chang ET, Villuendas R, Dibs S, Kadish AH, Goldberger JJ: Measuring the complexity of atrial fibrillation electrograms. J Cardiovasc Electrophysiol 2010; 21:649-655.

26. Kremen V, Lhotská L, Macas M, Cihák R, Vancura V, Kautzner J, Wichterle D: A new approach to automated assessment of fractionation of endocardial electrograms during atrial fibrillation: Physiol Meas 2008; 29:1371-1381.

27. Hunter RJ, Diab I, Thomas G, Duncan E, Abrams D, Dhinoja M, Sporton S, Earley MJ, Schilling RJ: Validation of a classification system to grade fractionation in atrial fibrillation and correlation with automated detection systems. Europace 2009; 11:1587-1596.

CHAPTER 6

A meta-analysis on adjunctive complex fractionated atrial electrogram ablation: comparing the incomparable?

Mattias Duytschaever, MD, PhD; Milad El Haddad, MS; Rene Tavernier, MD, PhD

This editorial was published in Europace, volume 13, issue 7, pages 909-910 in July 2011. It refers to 'Efficacy of adjunctive ablation of complex fractionated atrial electrograms and pulmonary vein isolation for the treatment of atrial fibrillation: a meta-analysis of randomized controlled trials' by M.H. Kong et al., Europace: 13(2):193–204

Pulmonary vein (PV) isolation is a generally accepted endpoint in catheter ablation of patients with paroxysmal atrial fibrillation (AF). In long-standing persistent AF or in the presence of advanced structural heart disease, atrial substrate modification on top of PV isolation may be required.[1] This may consist of deployment of additional linear lesions, adjunctive ablation of areas exhibiting complex fractionated atrial electrograms (CFAEs), or even a stepwise ablation strategy until conversion.[2] In recent years, several randomized controlled, single- and multicenter trials have been performed comparing a strategy of PV ablation only vs. PV ablation followed by additional defractionation. These studies revealed divergent results even between very experienced centers. Kong et al.[3] performed a meta-analysis of six prospective randomized studies evaluating the additional value of defractionation beyond PV ablation including both patients with paroxysmal AF and long-standing persistent AF.[4,5,6,7,8,9] This meta-analysis reveals a distinct benefit of additional defractionation on top of PV ablation with a significant overall increase in freedom of AF from 48 to 66% and a twice as high likelihood of being in sinus rhythm (odds ratio 1.98; confidence interval: 1.04–3.74). The randomized controlled trials (PubMed, clinicaltrials.gov), the primary outcome parameter (freedom of AF or atrial tachycardia with or without antiarrhythmic drug therapy after a single procedure), and the random-effect model were appropriately chosen, and analysis for sensitivity and heterogeneity was performed.

In spite of this, the conclusion and potential implications of this meta-analysis should be interpreted with vigilance. Analysis for publication bias and grading of the quality of the randomized clinical trials was not reported. Furthermore, there is a moderate heterogeneity in the primary outcome parameter, which itself is related to diversity in patient selection, PV ablation strategy, and defractionation approach between the incorporated studies. First, there are obvious differences in patient characteristics: three studies included patients with paroxysmal AF,[4,7,8] while three other studies included patients with high AF burden or longstanding persistent AF.[5,6,9] This is reflected in the marked variation in success rates especially in the ‘PV ablation’ arm with freedom of AF ranging from as low as 38 up to as high as 89%. Secondly, the chosen PV ablation strategy varied from circumferential PV ablation without a circular mapping catheter[4,5] to proven electrical PV isolation.[6,7,8,9] Furthermore, follow-up duration was highly variable, ranging from 3 to 16 months.[5,7] Finally, the defractionation approach was very different between the six studies at different echelons. Identification of CFAEs was performed using diverse methods varying from visual assessment[4,5,6,7,8] to commercially available but not validated algorithms.[9] Our group has recently reported that visual classification is highly subjective and that different commercial algorithms and cut-off values may point to different types of fractionation.[10] Also the ablation strategy of CFAEs varied from left atrial[4,6] to extensive bi-atrial defractionation[5,7,8,9] with a marked difference in the pre-specified endpoint (non-inducibility of AF,[4,7] AF conversion,[4,6,7,9] time limit,[4,6] or elimination of CFAEs[5,8,9]) resulting in a net increase in radiofrequency energy delivery times ranging from 14 to 33 min. On top of the observed heterogeneity—which to some extent could be considered inherent to any meta-analysis— other limitations are present. A negative publication bias cannot be excluded (especially in outcome studies), all studies were small size (maximum 50 patients in the defractionation arm), and no single study was performed with blinded analysis and/or central adjudication of endpoints. Data extraction from the cited studies can also be criticized. Elayi et al.[5] compared three different ablation strategies: PV ablation, PV isolation, and PV isolation with CFAE ablation. In the meta-analysis, patients with PV ablation and PV isolation were included in the control arm whereas PV isolation was the only PV strategy in the defractionation arm. It is likely that part of the beneficial effect of additional defractionation generated in the meta-analysis was to some extent due to the superior effect of PV isolation (freedom of AF 40%) over PV ablation (freedom of AF 11%). In the study by Deisenhofer et al.,[7] CFAE ablation was only performed in patients with inducible AF after PV isolation; yet patients with non-inducible AF from this study were also included in the defractionation arm of the meta-analysis.

Based on these elements, we believe that it is too early to recommend defractionation beyond PV isolation as a standard ablation strategy in patients with long-standing persistent AF or advanced structural heart disease. On the other hand, the present meta-analysis does support further research on CAFE ablation and substrate modification in general. Theoretically, ablation guided by activation mapping of fibrillatory waves with identification of the critical regions maintaining AF should be the ideal approach.[11] However, this method is unlikely to be implemented in clinical practice because it is time consuming and requires simultaneous wave mapping and offline analysis. As an alternative, we suggest performing better AF characterization at baseline using (i) substrate imaging of the atria[12] and (ii) an algorithmic objective description of fibrillatory electrograms.[10] Furthermore, ablation of objectively characterized fractionated electrograms should be guided by pre-specified objective endpoints. Only then the additional benefit of defractionation on top of PV isolation can be elucidated.

References

1. Calkins H, Brugada J, Packer DL, Cappato R, Chen SA, Crijns HJ et al. HRS/EHRA/ECAS Expert Consensus Statement on catheter and surgical ablation of atrial fibrillation: recommendations for personnel, policy, procedures and follow-up.

A report of the Heart Rhythm Society (HRS) Task Force on catheter and surgical ablation of atrial fibrillation. Heart Rhythm 2007;4:816–61.

2. O’Neill MD, Jaı¨s P, Hocini M, Sacher F, Klein GJ, Cle´menty J et al. Catheter ablation for atrial fibrillation. Circulation 2007;116:1515–23.

3. Kong MH, Piccini JP, Bahnson TD. Efficacy of adjunctive ablation of complex fractionated atrial electrograms and pulmonary vein isolation for the treatment of atrial fibrillation: a meta-analysis of randomized controlled trials: Europace 2011; 13:193–204.

4. Oral H, Chugh A, Lemola K, Cheung P, Hall B, Good E et al. Noninducibility of atrial fibrillation as an end point of left atrial circumferential ablation for paroxysmal atrial fibrillation: a randomized study. Circulation 2004;110:2797–801.

5. Elayi CS, Verma A, Di Biase L, Ching CK, Patel D, Barrett C et al. Ablation for longstanding permanent atrial fibrillation: results from a randomized study comparing three different strategies. Heart Rhythm 2008;5:1658–64.

6. Oral H, Chugh A, Yoshida K, Sarrazin JF, Kuhne M, Crawford T et al. A randomized assessment of the incremental role of ablation of complex fractionated atrial electrograms after antral pulmonary vein isolation for long-lasting persistent atrial fibrillation. J Am Coll Cardiol 2009;53:782–9.

7. Deisenhofer I, Estner H, Reents T, Fichtner S, Bauer A, Wu J et al. Does electrogram guided substrate ablation add to the success of pulmonary vein isolation in patients with paroxysmal atrial fibrillation? A prospective, randomized study. J Cardiovasc Electrophysiol 2009;20:514–21.

8. Di Biase L, Elayi CS, Fahmy TS, Martin DO, Ching CK, Barrett C et al. Atrial fibrillation ablation strategies for paroxysmal patients: randomized comparison between different techniques. Circ Arrhythm Electrophysiol 2009;2:113–9.

9. Verma A, Mantovan R, Macle L, De Martino G, Chen J, Morillo CA et al. Substrate and trigger ablation for reduction of atrial fibrillation (STAR AF): a randomized, multicentre, international trial. Eur Heart J 2010;31:1344–56.

10. El Haddad M, Houben R, Claessens T, Tavernier R, Stroobandt R, Duytschaever M. Histogram analysis: a novel method to detect and differentiate fractionated electrograms during atrial fibrillation. J Cardiovasc Electrophysiol 2011:22: 781-90.

11. Houben RP, de Groot NM, Allessie MA. Analysis of fractionated atrial fibrillation electrograms by wavelet decomposition. IEEE Trans Biomed Eng 2010;57: 1388–98.

12. Oakes RS, Badger TJ, Kholmovski EG, Akoum N, Burgon NS, Fish EN et al. Detection and quantification of left atrial structural remodeling with delayed-enhancement magnetic resonance imaging in patients with atrial fibrillation. Circulation 2009;119:1758–67.

PART III

General discussion

In this general discussion chapter, a brief introduction about technology and the development of electrophysiology is given. The chapter continues by a description of the current management of atrial fibrillation and how to improve its management using the conventional and the novel methods introduced in this thesis.

Technology and electrophysiology

Electrophysiology has evolved dramatically with advances in technology (Figure 1), especially during the last 2 decades with the fast development in the field of computing. The electrocardiogram shifted from an analog tracing of the pulse printed on a piece of paper to a digital signal acquired with high sampling rate and displayed on touch screens. The large recorded information and better computational power enabled the transition of the daily clinical strategies used by electrophysiologists into reliable and robust automated systems. These automated systems not only improved daily clinical work but also opened the door to better understanding of current arrhythmias and the discovery of new arrhythmias. A continued joined venture between electrophysiologists and engineers will further lead to better management and treatment of arrhythmias.

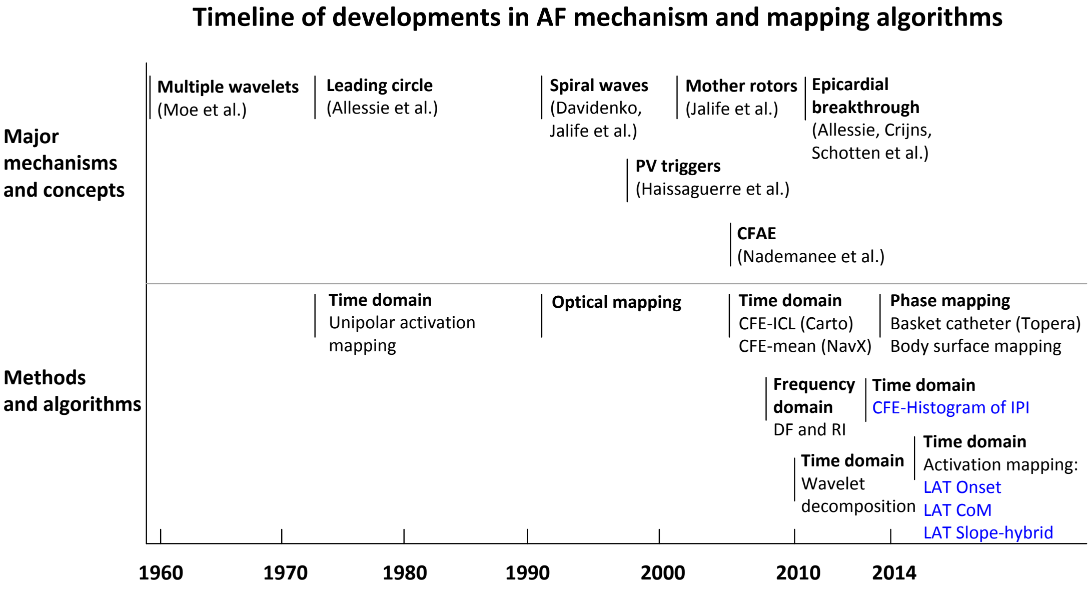

Figure III-1: *Timeline of development in atrial fibrillation (AF) for major mechanisms in and some of the methods and algorithms (including the methods in this work). In recent years, there has been great development of novel methods and algorithms to map AF and guide ablation. PV: pulmonary veins, CFAE: complex fractioned atrial electrograms, ICL: interval confidence level, DF: dominant frequency, RI: regularity index, IPI: inter-peak intervals, LAT: local activation time, CoM: center of mass.*

Current management of atrial fibrillation

According to the guidelines, atrial fibrillation (AF) can be classified into five types (first diagnosed, paroxysmal, persistent, long-standing persistent, and permanent).[1] In the elderly paucisymptomatic AF patient, AF management by either rate control or rhythm control has no difference in all-cause mortality or stroke rate.[2] However, in some AF patients, maintaining sinus rhythm improves quality of life and survival.[1] Rhythm control can be managed by antiarrhythmic drugs therapy (ADT) and/or catheter ablation (CA). In a systematic literature review comparing the efficacy of ADT (patients n=3180) and CA (n=2800), ADT showed a lower success rate at 52% (all drugs) compared to CA (57% success after single procedure without ADT).[3] Although the possibility that new generation ADT can offer better treatment for AF still holds, CA seems to be a more effective treatment platform.

The complexity of the ablation strategy is related to the type and complexity of AF. Although the exact mechanism of AF is still unclear, it is widely accepted that AF requires a trigger to initiate it and a substrate to maintain it. Especially in paroxysmal AF, episodes of AF can be triggered by single ectopic beats,[4,5] mainly originating from the pulmonary veins (PV).[6,7] As such, ablating these triggers seemed successful to maintain patients in sinus rhythm.[8] A more successful approach for trigger ablation is performing complete circumferential ablation of all PVs in order to electrically isolate the triggers (or potential triggers) from the left atrium.[9] At 1 year follow-up and taking into account multiple procedures, the success rate of CA based upon PV isolation was 74.9% in paroxysmal AF (without ADT, 1.4 procedures).[10] In other studies, long-term follow-up after 5 years showed a success rate of 80% in paroxysmal AF (of which 82% without ADT, 1.54 procedures).[11]

While isolating the AF triggers originating from the PVs is considered as the corner stone of AF ablation procedures, the ablation of the substrate remains controversial. In paroxysmal AF, PVI is sufficient to isolate the triggers in the PVs, whereas in persistent or long-standing persistent AF, ablation techniques (such as lesion lines, defractionation, debulking of the LA posterior wall, targeting dominant frequency and rotors) beyond PVI are needed for better outcome.[12-22] Regardless the ablation strategy, at 1 year follow-up and taking into account multiple procedures, the success rate of CA in persistent AF was 64.8% and 63.1% in long-standing persistent AF (without ADT, 1.4 procedures).[10] In other studies, long-term follow-up after 5 years showed a success rate in persistent AF of 60% (of which 89% without ADT, 1.5 procedures).[23]

Despite the sobering results in long-term freedom of AF (80% with 50% repeat in paroxysmal AF and 60% with 50% redo in persistent AF), CA procedure has been widely accepted as a standard treatment for patients with recurrent, symptomatic, and drug resistant AF.[24]

Towards better management of paroxysmal atrial fibrillation

In the majority of repeat ablations in paroxysmal AF, reconnection of the pulmonary veins is observed. As such, it can be predicted that more durable PV isolation will decrease the reported 50% repeat ablation rate. Improving PV isolation might be achieved by better monitoring of the contact force of the ablation catheter (lesion index), evaluating lesion formation by imaging (MRI and echo), using different energy sources or devices (surgical, single-shot RF catheters, cryoballoon, laser,…). It can be hypothesized that incomplete isolation at the time of the first ablation also contributes to the repeat procedure rate. As such, better identification of isolation via analysis of LA-PV electrograms might reduce the 50% repeat ablation as well. We introduced a novel tool (Chapter 4) for automated analysis of isolation in PVs based upon the likelihood that the PV still contains PV potentials. It remains to be proven whether this automated tool can facilitate PV isolation and improve AF ablation outcome (reduce repeat ablations).

Durable PV isolation on the other hand is not expected to increase the cumulative 80% success as the majority of the 20% recurrent AF are most likely non-PV triggered. We hypothesize that improvement of the success rate of paroxysmal AF above 80% might be achieved by:

1) keeping patients after the ablation procedure on ADT,

2) performing mapping and ablation of the patient-specific triggers beyond PVI. A recent study showed that ablation of non-PV triggers - originating from the LA appendage in 62.5% of the patients, CS in 53.1%, inter-atrial septum in 32.8%, SVC or crista terminalis in 19.8%, mitral valve annulus in 18.7%, and LA roof/free wall in 14.1% and present in 95% of the patients - beyond PVI can increase the success rate at 3 years follow-up to 88% after 2 procedures,[25]

3) **better selection of patients** (e.g. avoid ablation in paroxysmal AF patients with a CHADS2 score of more than 3 as it has been shown that these patients have 90% AF recurrence after 5 years follow-up).[26]

Towards better management of persistent atrial fibrillation

So far the success rate of ablation in persistent AF toped at 60% with 50% repeat ablation. Similar measures to the management of paroxysmal AF can be taken to reduce the 50% repeat procedures. Increasing the 60% success rate however, will be challenging with the current ablation strategies. We hypothesize that improvement of the success rate of persistent AF above 60% might be achieved by:

1) keeping patients after the ablation procedure on ADT. A recent study showed that using ADT after ablation was beneficial for maintain long-term freedom from AF,[27]

2) performing mapping and ablation of the patient–specific substrate. Ideally, ablation of the patient-specific substrate is based upon mapping of the patient-specific propagation of the fibrillatory waves. Allessie et al succeeded to perform high-density mapping of fibrillatory waves using the local activation time of the unipolar electrograms.[28] Jalife et al used high-resolution optical mapping to map AF in experimental models (spiral wave reentry and rotors).[29] These experimental mapping methods were not implemented in clinical practice due to the complexity of the technology. However, several indirect tools have been developed as surrogates for activation mapping of AF in clinical practice. These methods are based upon time-domain analysis (amplitude and interval, e.g. complex fractionated atrial electrograms), spectral analysis (Fourier transformation, e.g. dominant frequency, organization index, and rotors), and phase analysis (Hilbert transformation, e.g. rotors).

Substrate-guided ablation by *time-domain analysis* of complex fractionated atrial electrograms (CFAE) revealed unsatisfactory long-term efficacy.[30-32] We introduced a novel tool (Chapter 5) for better identification and differentiation of CFAE and its subtypes based upon the inter-peak intervals of electrograms. Prospective evaluation of this tool in guiding patient-specific substrate ablation to prove its value in improving the success rate of persistent AF ablation has yet to be performed.

Substrate-guided ablation by *spectral analysis* of dominant frequency, organization index, and rotors revealed also unsatisfactory long-term efficacy. However, the concept of finding the sources of fast firing represented by high frequency is a promising technique. The efficacy of substrate ablation guided by frequency analysis was recently evaluated in a multicenter clinical trial (RADAR-AF).[33] In 117 patients with persistent AF, ablation of the high frequency sources on top of PVI resulted in 61% freedom of AF after 1 year follow-up (single procedure, with or without antiarrhythmic drugs).[33]

Substrate-guided ablation by *phase analysis* of fibrillatory waves has been recently implemented in clinical practice to target rotors and focal sources maintaining AF (Topera RhythmView^{TM}).[31] After multi-procedures and 3 years follow-up, freedom from AF was observed in 70% of the patients.[34] Recently, Haissaguerre et al introduced and validated a system of body surface mapping (252-electrode-vest) for activation mapping in regular atrial tachycardia.[35] Although phase analysis has several limitations (requiring simultaneous multielectrode mapping, interpolation of electrograms to compensate low number of electrodes, electrograms morphology must be monophasic, detection of spiral waves around a core only - i.e. rotors)[36], it seems promising for detecting rotors in AF when combined with body surface mapping. Further clinical AF ablation studies and long-term follow-up in persistent AF are needed.

We believe that the limitations of the indirect tools can be overcome by true activation mapping of the fibrillatory waves. This will require high-density mapping devices (simultaneous recordings with multiple electrodes, very small electrode size and inter-space distance, large contact area) and robust algorithms to detect accurately the local activation time of the bipolar and/or unipolar electrograms in both normal and diseased atria. In this thesis we introduced and validated three novel methods to accurately assess the local activation time in bipolar and unipolar electrograms (Chapters 1 and 2).[37,38] We presume that these methods (especially U-LAT$_{\text{Slope-hybrid}}$) can be used to accurately annotate the local activation time of fibrillatory waves in AF. A representative case of accurate and direct activation mapping of a spiral wave reentry in an area of low voltage dense scar was demonstrated in Chapter 3.

It remains to be seen whether the above tools to identify the patient-specific substrate can tilt up the 60% efficacy rate in persistent AF. It can be postulated that in some patients, AF is not *maintained* by an active substrate, but rather *perpetuated* by multiple wavelets within the diseased atrial tissue.[39] Allessie et al observed in long-standing persistent AF patients with structural heart disease (64±9 years and dilated atrium) longitudinal dissociation of fibrillation waves together with epicardial breakthrough and transmural conduction during atrial fibrillation rather than the existence of rotors and focal sources.[40] Simultaneous endo-epicardial high density activation mapping during AF has shown electric dissociation between the endocardial and the epicardial layer.[41] It is unlikely that ablation can effectively eliminate the dissociation between the layers.

3) better selection of patients. To increase the success rate of ablation in persistent AF patients, it is important to know ‘whom not to ablate’ and avoid unnecessary ablation procedures. This can be achieved by a defining an exclusion strategy based upon pre-procedural assessment of the cardiac tissue properties by imaging- or electrical-based methods. Delayed-enhancement magnetic resonance imaging was used to stage the progress of AF by quantifying the degree of fibrosis in the left atrium.[42] The multicenter DECAAF study showed that AF ablation outcome can be predicted by staging of the left atrial fibrosis (Utah classification 1 to 4).[43] For the occurrence of disturbances in the conduction however, the overall quantity of fibrosis might be less important than the spatial distribution of fibrosis and the continuity of the thin epicardial layer.[44]

It can be hypothesized that electrical-based methods such as a pre-procedural electrophysiology study might be an effective strategy to (de)select patients. In this setting, the time-domain analysis of the inter-peak intervals (Chapter 5) might have the potential to identify efficiently patients with fibrosis or loss of epicardial continuity.[45] Other electrical-based methods could be based upon the analysis of fibrillatory electrograms by non-invasive methods such as the analysis of the AF cycle length on the surface ECG or wave mapping via body surface mapping.

References

1. Aliot EM, Stevenson WG, Almendral-Garrote JM, Bogun F, Calkins CH, Delacretaz E, Della Bella P, Hindricks G, Jaïs P, Josephson ME, Kautzner J, Kay GN, Kuck KH, Lerman BB, Marchlinski F, Reddy V, Schalij MJ, Schilling R, Soejima K, Wilber D; European Heart Rhythm Association (EHRA); Registered Branch of the European Society of Cardiology (ESC); Heart Rhythm Society (HRS); American College of Cardiology (ACC); American Heart Association (AHA). EHRA/HRS Expert Consensus on Catheter Ablation of Ventricular Arrhythmias: developed in a partnership with the European Heart Rhythm Association (EHRA), a Registered Branch of the European Society of Cardiology (ESC), and the Heart Rhythm Society (HRS); in collaboration with the American College of Cardiology (ACC) and the American Heart Association (AHA). Europace. 2009;11:771-817.

2. AFFIRM Investigators. A comparison of rate control and rhythm control in patients with atrial fibrillation. N Engl J Med 2002;347:1825–1833.

3. Calkins H, Reynolds MR, Spector P, Sondhi M, Xu Y, Martin A, Williams CJ, Sledge I. Treatment of atrial fibrillation with antiarrhythmic drugs or radiofre quency ablation: two systematic literature reviews and meta-analyses. Circ Arrhythm Electrophysiol 2009;2:349–361.

4. Jaïs P, Haïssaguerre M, Shah DC, Chouairi S, Gencel L, Hocini M, Clémenty J. A focal source of atrial fibrillation treated by discrete radiofrequency ablation. Circulation. 1997;95:572-6.

5. Waktare JE, Hnatkova K, Sopher SM, Murgatroyd FD, Guo X, Camm AJ, Malik M. The role of atrial ectopics in initiating paroxysmal atrial fibrillation. Eur Heart J. 2001;22:333-9.

6. Haïssaguerre M, Jaïs P, Shah DC, Takahashi A, Hocini M, Quiniou G, Garrigue S, Le Mouroux A, Le Métayer P, Clémenty J. Spontaneous initiation of atrial fibrillation by ectopic beats originating in the pulmonary veins. N Engl J Med. 1998 ;339:659-66.

7. Chen SA, Hsieh MH, Tai CT, Tsai CF, Prakash VS, Yu WC, Hsu TL, Ding YA, Chang MS. Initiation of atrial fibrillation by ectopic beats originating from the pulmonary veins: electrophysiological characteristics, pharmacological responses, and effects of radiofrequency ablation. Circulation. 1999;100:1879-86.

8. Haïssaguerre M, Jaïs P, Shah DC, Arentz T, Kalusche D, Takahashi A, Garrigue S, Hocini M, Peng JT, Clémenty J. Catheter ablation of chronic atrial fibrillation targeting the reinitiating triggers. J Cardiovasc Electrophysiol. 2000;11:2-10.

9. Pappone C, Oreto G, Rosanio S, Vicedomini G, Tocchi M, Gugliotta F, Salvati A, Dicandia C, Calabrò MP, Mazzone P, Ficarra E, Di Gioia C, Gulletta S, Nardi S, Santinelli V, Benussi S, Alfieri O. Atrial electroanatomic remodeling after circumferential radiofrequency pulmonary vein ablation: efficacy of an anatomic approach in a large cohort of patients with atrial fibrillation. Circulation. 2001;104:2539-44.

10. Cappato R, Calkins H, Chen SA, Davies W, Iesaka Y, Kalman J, Kim YH, Klein G, Natale A, Packer D, Skanes A, Ambrogi F, Biganzoli E. Updated worldwide survey on the methods, efficacy, and safety of catheter ablation for human atrial fibrillation. Circ Arrhythm Electrophysiol. 2010;3:32-8.

11. Ouyang F, Tilz R, Chun J, Schmidt B, Wissner E, Zerm T, Neven K, Köktürk B, Konstantinidou M, Metzner A, Fuernkranz A, Kuck KH. Long-term results of catheter ablation in paroxysmal atrial fibrillation: lessons from a 5-year follow-up. Circulation. 2010;122:2368-77.

12. Willems S, Klemm H, Rostock T, Brandstrup B, Ventura R, Steven D, Risius T, Lutomsky B, Meinertz T. Substrate modification combined with pulmonary vein isolation improves outcome of catheter ablation in patients with persistent atrial fibrillation: a prospective randomized comparison. Eur Heart J. 2006;27:2871-2878

13. Estner HL, Hessling G, Biegler R, Schreieck J, Fichtner S, Wu J, Jilek C, Zrenner B, Ndrepepa G, Schmitt C, Deisenhofer I. Complex fractionated atrial electrogram or

linear ablation in patients with persistent atrial fibrillation--a prospective randomized study. Pacing Clin Electrophysiol. 2011;34:939-948.

14. Pappone C, Manguso F, Vicedomini G, Gugliotta F, Santinelli O, Ferro A, Gulletta S, Sala S, Sora N, Paglino G, Augello G, Agricola E, Zangrillo A, Alfieri O, Santinelli V. Prevention of iatrogenic atrial tachycardia after ablation of atrial fibrillation: a prospective randomized study comparing circumferential pulmonary vein ablation with a modified approach. Circulation. 2004;110:3036-3042.

15. Knecht S, Hocini M, Wright M, Lellouche N, O'Neill MD, Matsuo S, Nault I, Chauhan VS, Makati KJ, Bevilacqua M, Lim KT, Sacher F, Deplagne A, Derval N, Bordachar P, Jaïs P, Clémenty J, Haïssaguerre M. Left atrial linear lesions are required for successful treatment of persistent atrial fibrillation. Eur Heart J. 2008;29:2359-2366.

16. Verma A, Mantovan R, Macle L, De Martino G, Chen J, Morillo CA, Novak P, Calzolari V, Guerra PG, Nair G, Torrecilla EG, Khaykin Y. Substrate and Trigger Ablation for Reduction of Atrial Fibrillation (STAR AF): a randomized, multicentre, international trial. Eur Heart J. 2010;31:1344-1356.

17. Nademanee K, McKenzie J, Kosar E, Schwab M, Sunsaneewitayakul B, Vasavakul T, Khunnawat C, Ngarmukos T: A new approach for catheter ablation of atrial fibrillation: Mapping of the Electrophysiologic substrate. J Am Coll Cardiol 2004;43:2044-2053.

18. Atienza F, Almendral J, Jalife J, Zlochiver S, Ploutz-Snyder R, Torrecilla EG, Arenal A, Kalifa J, Fernandez-Aviles F, Berenfeld O: Real-time dominant frequency mapping and ablation of dominant frequency sites in atrial fibrillation with left-to-right frequency gradients predicts long-term maintenance of sinus rhythm. Heart Rhythm 2009;6:33-40.

19. Sanders P, Berenfeld O, Hocini M, Jais P, Vaidyanathan R, Hsu LF, Garrigue S, Takahashi Y, Rotter M, Sacher F, Scavee C, Ploutz-Snyder R, Jalife J, Haissaguerre M: Spectral analysis identifies sites of high frequency activity maintaining atrial fibrillation in humans. Circulation 2005;112:789-797.

20. Mansour M: Highest dominant frequencies in atrial fibrillation: A new target for ablation? J Am Coll Cardiol 2006;47:1408-1409.

21. Jalife J. Rotors and spiral waves in atrial fibrillation. J Cardiovasc Electrophysiol 2003;14:776-80.

22. Narayan SM, Krummen DE, Rappel WJ: Clinical mapping approach to diagnose electrical rotors and focal impulse sources for human atrial fibrillation. J Cardiovasc Electrophysiol 2012;23:447-454.

23. O'Neill MD, Wright M, Knecht S, Jaïs P, Hocini M, Takahashi Y, Jönsson A, Sacher F, Matsuo S, Lim KT, Arantes L, Derval N, Lellouche N, Nault I, Bordachar P, Clémenty J, Haïssaguerre M. Long-term follow-up of persistent atrial fibrillation ablation using termination as a procedural endpoint. Eur Heart J. 2009;30:1105-12.

24. Camm AJ, Kirchhof P, Lip GY, Schotten U, Savelieva I, Ernst S, Van Gelder IC, Al-Attar N, Hindricks G, Prendergast B, Heidbuchel H, Alfieri O, Angelini A, Atar D,

Colonna P, De Caterina R, De Sutter J, Goette A, Gorenek B, Heldal M, Hohloser SH, Kolh P, Le Heuzey JY, Ponikowski P, Rutten FH. Guidelines for the management of atrial fibrillation: the task force for the management of atrial fibrillation of the European society of cardiology (ESC). Eur Heart J 2010;31:2369-2429.

25. Bai R, DI Biase L, Mohanty P, Santangeli P, Mohanty S, Pump A, Elayi CS, Reddy YM, Forleo GB, Hongo R, Beheiry S, Russo AD, Casella M, Pelargonio G, Santarelli P, Horton R, Sanchez J, Gallinghouse J, Burkhardt JD, Ma C, Lakkireddy D, Tondo C, Natale A. Catheter Ablation of Atrial Fibrillation in Patients with Mechanical Mitral Valve: Long-term Outcome of Single Procedure of Pulmonary Vein Antrum Isolation with or without Non- Pulmonary Vein Trigger Ablation. J Cardiovasc Electrophysiol. 2014 Apr. doi: 10.1111/jce.12433. [Epub ahead of print]

26. Chao TF, Ambrose K, Tsao HM, Lin YJ, Chang SL, Lo LW, Hu YF, Tuan TC, Suenari K, Li CH, Hartono B, Chang HY, Wu TJ, Chen SA. Relationship between the CHADS(2) score and risk of very late recurrences after catheter ablation of paroxysmal atrial fibrillation. Heart Rhythm. 2012;9:1185-91.

27. Gaztañaga L, Frankel DS, Kohari M, Kondapalli L, Zado ES, Marchlinski FE. Time to recurrence of atrial fibrillation influences outcome following catheter ablation. Heart Rhythm. 2013;10:2-9.

28. Konings KT, Kirchhof CJ, Smeets JR, Wellens HJ, Penn OC, Allessie MA. High-density mapping of electrically induced atrial fibrillation in humans. Circulation. 1994;89:1665-80.

29. Pertsov AM, Davidenko JM, Salomonsz R, Baxter WT, Jalife J. Spiral waves of excitation underlie reentrant activity in isolated cardiac muscle. Circ Res. 1993;72:631-50.

30. Rostock T, Salukhe TV, Steven D, Drewitz I, Hoffmann BA, Bock K, Servatius H, Müllerleile K, Sultan A, Gosau N, Meinertz T, Wegscheider K, Willems S. Long-term single- and multiple-procedure outcome and predictors of success after catheter ablation for persistent atrial fibrillation. Heart Rhythm. 2011;8:1391-1397.

31. Tilz RR, Chun KR, Schmidt B, Fuernkranz A, Wissner E, Koester I, Baensch D, Boczor S, Koektuerk B, Metzner A, Zerm T, Ernst S, Antz M, Kuck KH, Ouyang F. Catheter ablation of long-standing persistent atrial fibrillation: a lesson from circumferential pulmonary vein isolation. J Cardiovasc Electrophysiol. 2010;21:1085-93.

32. Lin YJ, Tsao HM, Chang SL, Lo LW, Hu YF, Chang CJ, Tsai WC, Suenari K, Huang SY, Chang HY, Wu TJ, Chen SA. Role of high dominant frequency sites in nonparoxysmal atrial fibrillation patients: insights from high-density frequency and fractionation mapping. Heart Rhythm. 2010;7:1255-62.

33. Atienza F, Ormaetxe J, Moya A, Martínez-Alday J, Hernandez-Madrid A, Castellanos E, Arribas F, Arias M, Tercedor L, Peinado R, Arenal A, Fdez-Avilés F, Almendral J, Jalife J. RADAR-AF Trial. Randomized multicenter comparison of radiofrequency catheter ablation of drivers versus circumferential pulmonary vein isolation in patients with atrial fibrillation. American Heart Association Late-Breaking Clinical Trial Report LBCT 05/Abstract. 2013

34. Narayan SM, Baykaner T, Clopton P, Schricker A, Lalani G, Krummen DE, Shivkumar K, Miller JM. Ablation of Rotor and Focal Sources Reduces Late Recurrence of Atrial Fibrillation Compared to Trigger Ablation Alone. J Am Coll Cardiol. 2014. pii: S0735-1097(14)01305-9.

35. Shah AJ, Hocini M, Xhaet O, Pascale P, Roten L, Wilton SB, Linton N, Scherr D, Miyazaki S, Jadidi AS, Liu X, Forclaz A, Nault I, Rivard L, Pedersen ME, Derval N, Sacher F, Knecht S, Jais P, Dubois R, Eliautou S, Bokan R, Strom M, Ramanathan C, Cakulev I, Sahadevan J, Lindsay B, Waldo AL, Haissaguerre M. Validation of novel 3-dimensional electrocardiographic mapping of atrial tachycardias by invasive mapping and ablation: a multicenter study. J Am Coll Cardiol. 2013;62:889-897.

36. Umapathy K, Nair K, Masse S, Krishnan S, Rogers J, Nash MP, Nanthakumar K. Phase mapping of cardiac fibrillation. Circ Arrhythm Electrophysiol. 2010;3:105-14.

37. El Haddad M, Houben M, Stroobandt R, Van Heuverswyn F, Tavernier R, Duytschaever M. Algorithmic detection of the beginning and end of bipolar electrograms: Implications for novel methods to assess local activation time during atrial tachycardia. Biomed Signal Process Control. 2013;8:981-991.

38. El Haddad M, Houben M, Stroobandt R, Van Heuverswyn F, Tavernier R, Duytschaever M. Novel algorithmic methods in mapping of atrial and ventricular tachycardia. Circ Arrhythm Electrophysiol 2014 – In press.

39. Allessie MA, Konings K, Kirchhof CJ, Wijffels M. Electrophysiologic mechanisms of perpetuation of atrial fibrillation. Am J Cardiol. 1996;77:10A-23A.

40. de Groot NM, Houben RP, Smeets JL, Boersma E, Schotten U, Schalij MJ, Crijns H, Allessie MA. Electropathological substrate of longstanding persistent atrial fibrillation in patients with structural heart disease: epicardial breakthrough. Circulation. 2010;122:1674-82.

44. Eckstein J, Zeemering S, Linz D, Maesen B, Verheule S, van Hunnik A, Crijns H, Allessie MA, Schotten U. Transmural conduction is the predominant mechanism of breakthrough during atrial fibrillation: evidence from simultaneous endo-epicardial high-density activation mapping. Circ Arrhythm Electrophysiol. 2013;6:334-41.

45. Oakes RS, Badger TJ, Kholmovski EG, Akoum N, Burgon NS, Fish EN, Blauer JJ, Rao SN, DiBella EV, Segerson NM, Daccarett M, Windfelder J, McGann CJ, Parker D, MacLeod RS, Marrouche NF. Detection and quantification of left atrial structural remodeling with delayed-enhancement magnetic resonance imaging in patients with atrial fibrillation. Circulation. 2009;119:1758-1767.

43. Marrouche NF, Wilber D, Hindricks G, Jais P, Akoum N, Marchlinski F, Kholmovski E, Burgon N, Hu N, Mont L, Deneke T, Duytschaever M, Neumann T9, Mansour M, Mahnkopf C, Herweg B, Daoud E, Wissner E, Bansmann P15, Brachmann J. Association of atrial tissue fibrosis identified by delayed enhancement MRI and atrial fibrillation catheter ablation: the DECAAF study. JAMA. 2014;311:498-506.

44. Verheule S, Tuyls E, Gharaviri A, Hulsmans S, van Hunnik A, Kuiper M, Serroyen J, Zeemering S, Kuijpers NH, Schotten U. Loss of continuity in the thin

epicardial layer because of endomysial fibrosis increases the complexity of atrial fibrillatory conduction. Circ Arrhythm Electrophysiol. 2013 Feb;6:202-11.

45. El Haddad M, Houben R, Claessens T, Tavernier R, Stroobandt R, Duytschaever M. Histogram analysis: a novel method to detect and differentiate fractionated electrograms during atrial fibrillation. J Cardiovasc Electrophysiol 2011:22: 781-90.

SUMMARY

In **Part I** of this dissertation, a brief description of the heart and history of arrhythmias is given. Even though the first arrhythmias were discovered 2000 years ago, we are still aiming to understand their mechanisms in order to optimize their treatments. Catheter ablation has emerged recently as an effective non-pharmaceutical treatment for regular atrial tachycardia (AT), regular ventricular tachycardia (VT), and atrial fibrillation (AF). Ablation procedures are guided by electroanatomical mapping based upon the analysis of intracardiac electrograms. Due to several limitations however, current ablation strategies are not yet completely effective. As such, accurate algorithmic methods to analyze electrograms are essential to facilitate the ablation procedure and improve its safety and efficacy.

Novel algorithmic methods introduced and developed to optimize the ablation procedure are described in **Part II.** In **chapters 1 to 3**, we describe the optimization of mapping and ablation in regular atrial and ventricular tachycardias. Mapping of arrhythmias requires accurate detection of the local activation time in unipolar or bipolar electrograms. Conventional assessment of the local activation time in unipolar and bipolar electrograms however, is not accurate due to far-field potentials in unipolar electrograms and wavefront direction, bipole orientation, electrode size, and inter-electrode spacing in bipolar electrograms. We introduced and validated three novel methods to assess local activation time in unipolar and bipolar electrograms in both atrial and ventricular tachycardia. We showed that the novel methods have incremental benefit over conventional methods especially when used in mapping of complex activation patterns and in the presence of low quality and low voltage electrograms. Implementation of the developed methods in existing or new electroanatomical mapping systems may facilitate comprehensive mapping and enable automated activation mapping of tachycardias (multi-electrode mapping).

In **chapters 4 to 6**, we describe the optimization of mapping and ablation in atrial fibrillation (AF). As pulmonary vein isolation (PVI) is essential for successful atrial fibrillation procedure, we first developed a novel step-wise algorithm for automated identification of isolated veins during sinus rhythm. The step-wise approach algorithm based upon the likelihood that a pulmonary vein recording still contains pulmonary vein potentials revealed high sensitivity and accuracy to identify isolated veins. In AF patients requiring further substrate ablation, we introduced and developed a time-domain algorithm based upon histogram analysis of inter-peak intervals to quantify fractionation in electrograms. The algorithm accurately differentiated between continuous fractionated electrograms, discontinuous fractionated electrograms, and normal electrograms. These methods can be implemented in existing or new electroanatomical mapping systems to facilitate and guide ablations in AF patients.

Finally in **Part III**, I discuss the effect of technology on electrophysiology and better management of atrial fibrillation. At 5-years follow-up, catheter ablation of paroxysmal AF achieves 80% freedom of AF (taking into account 50% repeat ablations). In persistent AF these figures are 60% and 50% respectively. Improvements in PV isolation might reduce the repeat ablations. The following strategies might increase the cumulative success rate in both paroxysmal and persistent AF: 1) continued antiarrhythmic drugs therapy after ablation, 2) mapping of the patient-specific AF triggers and substrate, and 3) better patient selection.

SAMENVATTING

Deze thesis beschrijft de ontwikkeling en validatie van nieuwe algoritmes voor het optimaliseren van ablatieprocedures van regelmatige en onregelmatige tachycardieën. In **Deel I**, wordt de anatomie het hart en de geschiedenis van een ritmestoornissen in het kort beschreven. Niettegenstaande ritmestoornissen voor het eerst 2000 jaar geleden werden vastgesteld, proberen we nog steeds het mechanisme te achterhalen om aldus tot een betere behandeling te komen. Catheterablatie is een recente techniek voor de niet-farmacologische behandeling van een regelmatige atriale tachycardie, een regelmatige ventrikeltachycardie en voorkamerfibrillatie. Tijdens ablatieprocedures wordt gebruik gemaakt van elektro-anatomische mapping die gebaseerd is op analyse van intracardiale elektrogrammen. Door een aantal beperkingen zijn ablatieprocedures helaas niet altijd compleet succesvol. Nauwkeurige algoritimische methodes zijn daarom noodzakelijk om de ablatieprocedure te vergemakkelijken en hun efficaciteit en veiligheid te verhogen.

Nieuwe algoritmes om ablatieprocedures te optimaliseren werden ontwikkeld en beschreven in **Deel II**. In **hoofdstuk 1 tot 3** rapporteren we de optimalisatie van de mapping en ablatie van regelmatige atriale en ventriculaire tachycardieën. Mapping van ritmestoornissen vergt een accurate detectie van de locale activatietijd in unipolaire en bipolaire elektrogrammen. Conventionele analyse van de locale activatietijd in unipolaire en bipolaire electrogrammen is echter onnauwkeurig. Dit kan te wijten zijn aan verre-veld potentialen in unipolaire electrogrammen en de richting van het golffront, de orientatie van de bipool, de grootte van de elektrode en de inter-elektrode afstand in bipolaire electrogrammen.

Wij ontwikkelden en valideerden drie nieuwe methodes om de locale activatietijd in unipolaire en bipolaire elctrogrammen te bepalen zowel tijdens atriale tachycardie als tijdens ventrikeltachycardie. We toonden aan dat de nieuwe methodes een supplementair voordeel bieden ten opzichte van de conventionele methodes tijdens de mapping van complexe activatiepatronen en in de aanwezigheid van laag- en hoogkwaliteit electrogrammen. Implementatie van de nieuw ontwikkelde methodes in bestaande elektro-anatomische mapping systemen kan extensieve mapping vergemakkelijken en laat toe een automatische mapping (multi-elektrode mapping) van ritmestoornissen uit te voeren.

In **hoofdstuk 4 tot 6**, beschrijven we de optimalisatie en ablatie van voorkamerfibrillatie (VKF). Daar isolatie van de pulmonale venen essentieel is voor een succesvolle ablatie van VKF hebben we eerst een nieuw stapsgewijs algoritme ontwikkeld dat toelaat na te gaan of de pulmonale venen geïsoleerd zijn tijdens sinusritme. Het stapsgewijs algoritme gebaseerd op de waarschijnlijkheid dat een pulmonaal-vene recording nog pulmonaal-vene potentialen bevat, vertoonde een hoge sensitiviteit en nauwkeurigheid om geïsoleerde venen te identificeren. Bij patiënten met VKF die een verdere ablatie van het substraat nodig hadden, introduceerden we een tijdsdomein algoritme gebaseerd op histogram analyse van de interpiek intervallen om de fragmentatie in de electrogrammen te kwantificeren. Het algoritme kon duidelijk het onderscheid maken tussen continu-gefragmenteerde, discontinu-gefragmenteerde en normale electrogrammen. Deze methodes kunnen geïmplementeerd worden in bestaande en nieuwe elektro-anatomische mapping systemen als welgekomen hulp bij ablatie van VKF.

Tenslotte behandelen we in Deel III hoe de technologie een bijdrage kan leveren aan de elektrofysiologie en de behandeling van voorkamerfibrillatie kan verbeteren. Na 5 jaar follow-up is 80% van de patiënten met paroxismale voorkamerfibrillatie vrij van recidief (evenwel dient rekening gehouden te worden dat 50% een “redo” ablatie diende te ondergaan). Bij patiënten met persisterende voorkamerfibrillatie bedragen deze cijfers respectievelijk 60% en 50%. Een verbeterde isolatie van de pulmonale venen kan zeker leiden tot een daling van het aantal “redo” procedures. Volgende strategieën kunnen mogelijks het cumulatief succes zowel bij paroxismale en persisterende voorkamerfibrillatie doen toenemen:1) verdere onderhoudsbehandeling met antaritmica na ablatie, 2) mapping van patiënt-specifieke triggers van voorkamerfibrillatie en substraat, en 3) betere patiëntenselectie.

ACKNOWLEDGEMENTS

This dissertation is the result of the work I did from March 2009 until March 2014 at the department of cardiology and electrophysiology at Ghent University Hospital (UZ Gent) in Belgium. I accomplished this work with the contribution and support of many people whom I am greatly thankful for:

“ First, I want to thank my promoter Professor **Mattias Duytschaever**. Professor Duytschaever was more than a promoter to me; he was an ideal whom I was always impressed by his intellects, leadership, and brilliant ideas that made me achieve this work with confidence. Dear Mattias, I can never express how much I am grateful for having you as my promoter. I want to thank you for the informal, trustful, and friendly atmosphere you kept between us. I will never forget the vast time you sacrificed from your family in order for us to meet. **Isabelle**, **Charles**, and **Emilia,** thank you for being friendly and making me feel welcomed at your home. I will miss the countless meetings I had with Mattias in Drongen.

It goes without saying how much I am thankful for Professor **Roland Stroobandt**, the "Pope" of the electrophysiology family at UZ. Prof. Stroobandt was my first contact at UZ from 2007 and took care of me since then. Dear Prof. Stroobandt, I want to thank you for your valuable scientific input which was extremely important and essential to accomplish this work. You were the figure of a father who trusted me, believed in my potential, and made sure I could stay in Ghent to pursue my doctorate. I will always be grateful for everything you have done for me.

Special thanks to Professor **Rene Tavernier** and **Richard Houben** who immeasurably contributed to my research. Rene and Richard always supported and gave their time and important input to every study in this dissertation.

I want to thank Professor **Yves Taeymans** on the top of the cardiology department for taking me in and arranging the financial supports that were necessary for my stay and to accomplish this work. I want to thank Dr. **Frederic Van Heuverswyn** and Dr. **Liesbeth Timmers** who always supported me without any hesitation. It was always wonderful and pleasant to be with you on conferences from the sunny Mediterranean of Nice at Cardiostim to the edge of the snowy Rocky Mountains of Colorado at Heart Rhythm, and on other events in the historical Ghent and Bruges.

I want to further convey my acknowledgments to everyone at the department of cardiology at UZ Gent (my family away from my family), starting from the head of the department Dr. **Michel De Pauw,** and doctors **Frank Timmermans**, **Els Vandecasteele**, **Hans De Wilde**, **Benny Drieghe** and Professor **Peter Gheeraert.** Thank you all for the interesting scientific and non-scientific discussions and chats that made me feel one of you. I am in great debt to the support team at the EP lab especially **Rudy, Guy, Isabel**, and **Marnicks** who provided me with everything I needed to export my data for analysis. I also want to thank **Marc De Buyzere** for his feedback on the complex statistics problems I faced. I can never thank enough **Karlien**, the dynamo of administration who managed my contracts, permits, and paperwork with efficacy and expertise and always with a smile. A special thanks to my neighbors on the 10th floor, **Dries**, **Krista**, **Valery**, **Sofie**, **Michelle, Thea, Filiep** and **Veerle** who made the work environment feels like a second home.

I don't want to forget the cardiology department at AZ-Sint Jan Bruges where I collected great amount of my data as well. I am thankful for everyone who helped me there, especially Dr. **Yves Vandekerckhove**, Dr. **Benjamine Berte**, Dr. **Marta Acena**, and **Hannelore**.

In the end, I want to express my endless gratitude to my parents **Abbas** and **Siham** and my sisters **Abir** and **Rana**, who were more than 3000 Km away but in reality were always with me. You have been continuously generous to me in your care, trust, and all the support I needed to follow my goals and dreams. I also want to thank my girlfriend **Linda**, who encouraged me to start this doctorate and accompanied me from the beginning to the end. Finally, I want to thank everyone who was part of my life during this journey in this wonderful country. ❞

Milad El Haddad

Ghent, March

2014

LIST OF TABLES

LIST OF FIGURES